Study on pulse shapes of germanium detectors with a point like contact geometry for the GERDA and MAJORANA experiments

Dissertation

der Mathematisch-Naturwissenschaftlichen Fakultät
der Eberhard Karls Universität Tübingen
zur Erlangung des Grades eines
Doktors der Naturwissenschaften
(Dr. rer. nat.)

vorgelegt von
Alexander Hegai
geboren in Alma-Ata/Kasachstan

Tübingen
2018

Gedruckt mit Genehmigung der Mathematisch-Naturwissenschaftlichen Fakultät
der Eberhard Karls Universität Tübingen.

Tag der mündlichen Qualifikation:	15. 06. 2018
Dekan:	Prof. Dr. Wolfgang Rosenstiel
1. Berichterstatter:	Prof. Dr. Josef Jochum
2. Berichterstatter:	Prof. Dr. Peter Grabmayr

for my girls

Abstract

Point-like contact germanium detectors are one of the leading technologies in the neutrinoless double beta decay ($0\nu\beta\beta$) search and are used in the GERDA and MAJORANA experiments. These kinds of detectors provide a superb energy resolution as a result of their low capacitance. This low capacitance and the strong inhomogeneous electric field are due to the point-like geometry of the contact. The electric field is particularly strong close to the point contact and leads to distinctive pulse shape topologies for different event classes. $0\nu\beta\beta$ experiments take advantage of this feature by rejecting specific event types to maximize the signal to background ratio.

The first part of this work describes the characterization procedure and corresponding results for the second batch of such point-like contact detectors used in the GERDA experiment. These detectors were manufactured from enriched ^{76}Ge by Canberra Semiconductors N.V.. The focus of this study is to probe the homogeneity of the pulse shape behavior along the surface and bulk of the detectors. The results show that most of the detectors have small deviations from a homogeneous spatial distribution for the pulse shape parameters. Through simulations, which were also conducted in this work, it is shown that this behavior originates in the collection of free charges on the passivation layer close to the point contact. This effect can be neutralized by removing the passivation layer which is not needed if the detectors are operated in a noble liquid gas.

The second part of this work reports the study of ultra pure and large prototype point contact detectors. These detectors were developed by ORTEC and are used in the MAJORANA experiment. Surface scans of these detectors with a collimated ^{241}Am source and coincident measurements with a β^+ source show that the low electric fields caused by the extremely high purity can lead to a degraded pulse shape performance. This effect was also investigated and reproduced in simulations by modeling the size of the charge cloud evolution during its drift. The resulting simulations enable the correct selection of the ingot impurity profiles for the manufacturing of large point-like contact detectors for the next generation of $0\nu\beta\beta$ experiments.

Zusammenfassung

Germanium Detektoren mit einem punktförmigen Kontakt sind eine der führenden Technologien bei der Suche nach dem neutrinolosen Doppel-Betazerfall und werden in dem GERDA- sowie MAJORANA-Experiment eingesetzt. Aufgrund ihrer geringen Kapazität, besitzen diese Detektoren eine hervorragende Energieauflösung. Ihren Ursprung haben die niedrigere Kapazität sowie das stark inhomogene Feld in dem punktförmigen Design des Kontaktes. In dessen unmittelbarer Nähe ist das elektrische Feld besonders stark und führt so zu charakteristischen Pulsformen der Signale für unterschiedlich Ereignisklassen. Diese Eigenschaft wird in den $0\nu\beta\beta$ Experimenten genutzt, um das Signal zu Untergrund Verhältnis zu maximieren indem bestimmte Ereignisklassen verworfen werden.
Der erste Teil dieser Arbeit beschreibt die Charakterisierung sowie die dazugehörigen Ergebnisse der zweiten Batch solcher Punktkontaktdetektoren des GERDA Experimentes. Diese wurden aus in ^{76}Ge angereichertem Germanium von Canberra Semiconductors N.V. hergestellt. Der Fokus dieser Studie ist die Untersuchung der Homogenität der Pulsform im Inneren sowie entlang der Oberfläche der Detektoren. Die Ergebnisse zeigen, dass die meisten Detektoren eine kleine Abweichung von der homogenen Verteilung der Pulsformparamter aufweisen. Durch Simulationen, die ebenfalls im Rahmen dieser Arbeit durchgeführt worden sind, wurde gezeigt, dass der Ursprung dieses Verhaltens in der Ansammlung freier Ladungsträger an der Passivierungsschicht um den Punktkontakt liegt. Dieser Effekt kann durch die Entfernung der Passivierungsschicht unterbunden werden. Durch den Betrieb der Detektoren in einem flüssigen Edelgas kann auf die Passivierungsschicht verzichtet werden.
Der zweite Teil der Arbeit erläutert die Ergebnisse einer Studie zu ultra-reinen und großen Punktkontaktdetektoren. Diese wurden von der Firma ORTEC entwickelt und werden in dem MAJORANA Experimenten verwendet. Oberflächenscans dieser Detektoren mit einer kollimierten ^{241}Am Quelle sowie Koinzidenzmessungen mit einem β^+ Emitter zeigen, dass die niedrigen elektrischen Felder, hervorgerufenen durch die extrem hohe Reinheit, zu einer Degradierung der Pulsformperformance führen können. Dieser Effekt wurde ebenfalls untersucht und in Simulationen durch die Modellierung der Größe der Ladungsträgerwolke während ihres Driftens reproduziert. Die resultierenden Simulationen ermöglichen die Selektion des notwendigen Unreinheitsprofils der Kristalle für die Produktion großer Punktkontaktdetektoren für die nächste Generation von $0\nu\beta\beta$ Experimenten.

Table of contents

Introduction **vii**

1 The search for the neutrinoless double beta decay **1**
1.1 Neutrinoless double beta decay 1
1.2 Experimental sensitivity 4
1.2.1 Background 6
1.3 GERDA 6
1.3.1 Experimental setup 7
1.3.2 Background reduction techniques 8

2 Germanium detectors **13**
2.1 Interaction of radiation with matter 13
2.1.1 Charged radiation 14
2.1.2 Uncharged radiation 16
2.2 Semiconductor detectors 19
2.3 Signal formation 20
2.4 High Purity Germanium detectors 22
2.4.1 BEGe (Broad Energy Germanium detectors) 23
2.4.2 p^+ Point Contact detectors from ORTEC 24
2.5 Pulse shape discrimination 24

3 Pulse shape simulation **27**
3.1 Field simulation 27
3.2 Signal generation 29
3.2.1 Charge carrier drift 29
3.2.2 Charge carrier cloud size 30

4 BEGe characterization **33**
4.1 Detector production 33

4.2 HEROICA @ HADES . . . 35
4.3 ^{241}Am scanning setup . . . 36
4.4 ^{241}Am scanning measurements . . . 37
4.5 ^{241}Am scanning results . . . 41
4.5.1 Rise and drift time . . . 41
4.5.2 A/E parameter . . . 50
4.6 Comparison with the simulations . . . 61
4.7 Thermal cycle on detector Bes . . . 66
4.8 Collimated ^{228}Th measurements on detector Bes . . . 67
4.9 Conclusion . . . 68

5 Ultra high purity germanium detectors 71
5.1 PONaMa field simulation . . . 72
5.2 ^{241}Am scanning measurements . . . 74
5.2.1 Experimental setup . . . 74
5.2.2 Results and simulations . . . 74
5.3 Coincidence measurements . . . 80
5.3.1 Experimental setup . . . 80
5.3.2 Analysis chain . . . 82
5.3.3 Results and simulations . . . 82
5.4 Reference measurement . . . 92
5.5 Conclusion . . . 92

6 Conclusion and outlook 97

List of figures 99

List of tables 103

References 105

Appendix A Appendix 111

Introduction

The search for the neutrinoless double beta decay ($0\nu\beta\beta$) is one of the main topics in the fundamental particle physics since its discovery would show a lepton number violating process. This could explain the matter and antimatter asymmetry through leptogenesis and answer the question why the universe like we know it exists. Furthermore it could show the fundamental nature of neutrinos, namely if they are Dirac or Majorana particles and what is their absolute mass scale.
In the neutrinoless double beta decay process two neutrons decay into two protons emitting two electrons without the emission of the corresponding anti-electron neutrinos. The energy is nearly completely transferred to the electrons due to their high mass difference to the nucleus. To measure the energy of these two electrons with an extremely high accuracy in a nearly background free environment, is the goal of several experiments like GERDA, MAJORANA, KamLAND-Zen, EXO-200 etc. In GERDA and MAJORANA the high accuracy and efficiency is achieved by the use of germanium detectors which can provide an energy resolution in the range of single keV for the $Q_{\beta\beta}$ value of 2.039 MeV of ^{76}Ge, a double beta decay candidate. The high efficiency is a results from the use of the ^{76}Ge isotope as detector and source at the same time. A short overview on neutrino physics and the GERDA experiment will be given in chapter 1.
Furthermore the use of a new generation of germanium detectors in GERDA offers a simple and effective background suppression possibility through the separation of event classes via pulse shape analysis. This enables a quasi background free experiment with a background index of $0.7^{+1.1}_{-0.5} \cdot 10^{-3}$ cts/(keV·kg·yr) and a sensitivity of $4.0 \cdot 10^{25}$ yr at 90% C.L. [1]. A quick introduction on the basics of germanium detectors can be found in chapter 2. Chapter 3 gives an introduction to the germanium detector pulse shape simulation framework `mjd_siggen`[2]. A detailed description of the characterization procedure for the Phase II detectors for the GERDA experiment is given in chapter 4. And chapter 5 summarizes the results from testing of ultra pure prototype detectors for the MAJORANA experiment. The last chapter 6 summarizes the results of this work and gives a brief outlook on further projects related to it.

Chapter 1

The search for the neutrinoless double beta decay

1.1 Neutrinoless double beta decay

The double beta decay

$$A(Z,N) \rightarrow A(Z+2,N-2) + 2e^- + 2\bar{\nu}_e \tag{1.1}$$

can occur in even-even nuclei where normal beta decay is energetically forbidden, but the simultaneous conversion of two neutrons into two protons is possible. This condition is satisfied by only a small number of isotopes and since it is a second order decay, the corresponding lifetimes are very long, on the order of 10^{18-24} yr [3]. If the neutrino is a Majorana particle, as predicted by Ettore Majorana in 1937 [4] then a neutrinoless double beta decay ($0\nu\beta\beta$) mode is also possible, where the two anti-neutrinos are not emitted.

$$A(Z,N) \rightarrow A(Z+2,N-2) + 2e^- \tag{1.2}$$

This process violates the electronic lepton number L_e by two units and is therefore forbidden in the Standard Model (SM) of particle physics. It also requires an extension of the SM to include neutrino mass, which has been shown to be true by neutrino oscillation experiments such as SNO [5], Super-Kamiokande [6] and Double Chooz [7]. The simplest mechanism to realize the neutrinoless double beta decay is the exchange of a light Majorana neutrino (see fig. 1.2). Other exotic mechanisms like the exchange of a heavy neutrino or a Higgs triplet are possible, but not considered in this work. A good overview is given in [8] and [9].

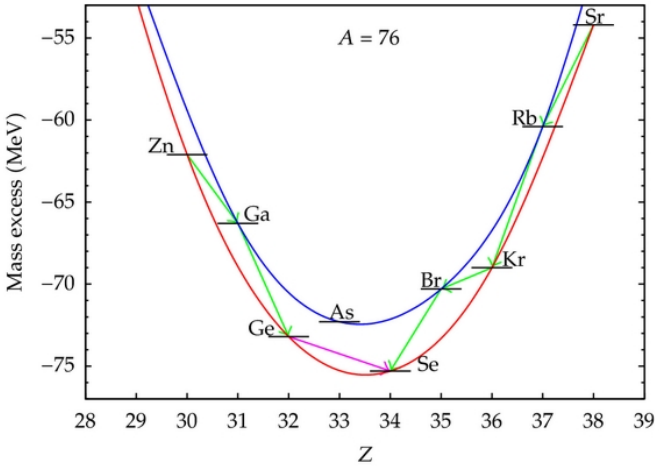

Fig. 1.1 Mass parabola and decay scheme of nuclei with A=76. Even-even nuclei are energetically more favorable than odd-odd configurations. The single beta decay from ^{76}Ge to ^{76}As is energetically forbidden and thus enables the double beta decay to ^{76}Se. Figure is taken from [10].

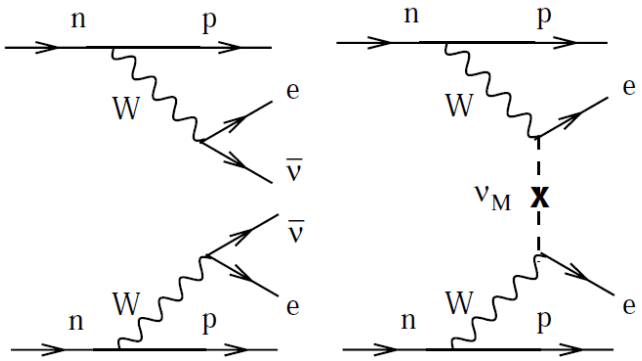

Fig. 1.2 Left: Feynman diagram for $2\nu\beta\beta$ decay. Right: Feynman diagram for $0\nu\beta\beta$ decay via exchange of a light Majorana neutrino. Figures taken from [11].

The half-life $T_{1/2}^{0\nu}$ of the $0\nu\beta\beta$ decay is much longer than the half-life of the $2\nu\beta\beta$ decay since it requires the exchange of a light Majorana neutrino. Its best limits are in the region of 10^{25} yr provided by the GERDA [1] and KamLAND-ZEN [12] experiments. This leads to very small decay rates and is therefore challenging to measure experimentally. The half-life of $0\nu\beta\beta$ is given by:

$$\left(T_{1/2}^{0\nu}\right)^{-1} = G^{0\nu}(Q_{\beta\beta}, Z) \cdot |M^{0\nu}|^2 \frac{m_{ee}^2}{m_e^2} \tag{1.3}$$

where $G^{0\nu}$ is the phase space factor which scales with the fifth power of the endpoint energy $Q_{\beta\beta}$ and the atomic number Z. High endpoint energies over 2 MeV are favorable for the experimental setup since this makes it easier to distinguish the signal from the background. $M^{0\nu}$ is the nuclear transition matrix element. There are several methods such as QRPA, IBM, EDF etc. to calculate it and the results can vary by up to a factor of 5 [13] which introduces a large uncertainty on the half-life (see fig. 1.3). m_e is the electron rest mass and m_{ee} is the effective Majorana neutrino mass and a superposition of the mass eigenstates m_i:

$$m_{ee} = \sum_{i=1}^{3} |U_{ei}^2 m_i| = |e^{i\alpha_1}|U_{e1}^2 m_1| + e^{i\alpha_2}|U_{e2}^2 m_2| + e^{-2i\delta}|U_{e3}^2 m_3||} \tag{1.4}$$

These are connected via the Pontecorvo-Maki-Nakagawa-Sakata (PMNS) matrix:

$$\begin{aligned} U = &\begin{pmatrix} 1 & 0 & 0 \\ 0 & C_{23} & S_{23} \\ 0 & -S_{23} & C_{23} \end{pmatrix} \times \begin{pmatrix} C_{13} & 0 & S_{13}e^{-i\delta} \\ 0 & 1 & 0 \\ -S_{13}e^{i\delta} & 0 & C_{13} \end{pmatrix} \times \\ &\begin{pmatrix} C_{12} & S_{12} & 0 \\ -S_{12} & C_{12} & 0 \\ 0 & 0 & 1 \end{pmatrix} \times \begin{pmatrix} e^{i\alpha_1/2} & 0 & 0 \\ 0 & e^{i\alpha_2/2} & 0 \\ 0 & 0 & 1 \end{pmatrix} \end{aligned} \tag{1.5}$$

to the flavor eigenstates $|\nu_\kappa\rangle\,(\kappa = (e, \mu, \tau))$. With $C_{ij} \equiv \cos\theta_{ij}$ and $S_{ij} \equiv \sin\theta_{ij}$. θ_{ij} represents the three mixing angles. δ is the CP-violating Dirac phase. α_1 and α_2 are only present if the neutrinos are Majorana particles and are thus called the Majorana phases.

Neutrino oscillation experiments such as Super-Kamiokande and SNO are only sensitive to the mass-squared differences Δm_{12}^2 and Δm_{23}^2. The sign of the second mass difference Δm_{23}^2, which is measured by atmospheric neutrinos, is unknown and thus allows two possible orderings for the mass eigenstates:

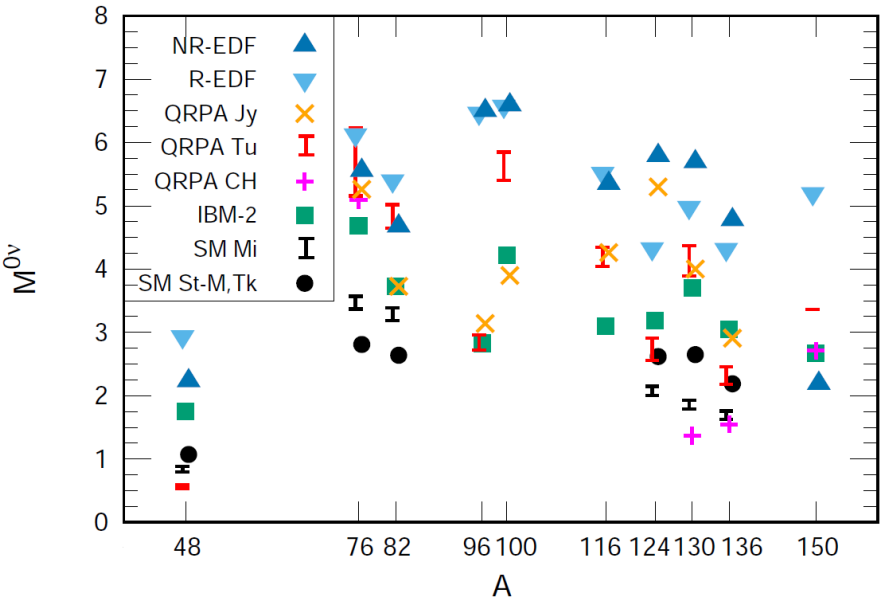

Fig. 1.3 Nuclear matrix elements for various $0\nu\beta\beta$ candidates calculated with the different approximation models. Figure is taken from [13].

- normal hierarchy (NH) with $m_1 < m_2 < m_3$
- inverted hierarchy (IH) with $m_3 < m_1 < m_2$

If NH is true, then m_1 is the lightest mass eigenstate, whilst for IH it is m_3. In both cases the solar mass difference $\Delta m^2_{\odot} \equiv \Delta m^2_{12} = m_2^2 - m_1^2$ is much smaller than the atmospheric Δm^2_{A}. In the case of NH $\Delta m^2_{\mathrm{A}} = \Delta m^2_{31} > 0$, whilst for IN $\Delta m^2_{\mathrm{A}} = \Delta m^2_{32} < 0$. The mass ordering is very important for a $(0\nu\beta\beta)$ decay search since for NH the effective Majorana mass could have very small values or vanish completely. This is not possible in the IH scenario, assuming three neutrino flavors. Here a minimum value of $|m_{ee}^{IH}| \approx 0.01 - 0.02$ eV is given for the effective Majorana neutrino mass (see fig. 1.4). Thus a discovery of the neutrinoless double beta decay could contribute to the identification of the mass ordering.

1.2 Experimental sensitivity

The search for the $0\nu\beta\beta$ decay is a very challenging task for experimental physics. The double beta decay itself is a second order process which already leads to extremely long half lives. Additionally, $0\nu\beta\beta$ decay requires the exchange of a light Majorana neutrino which extends the half lives even more. With the predicted half lives in the range of 10^{25} yr,

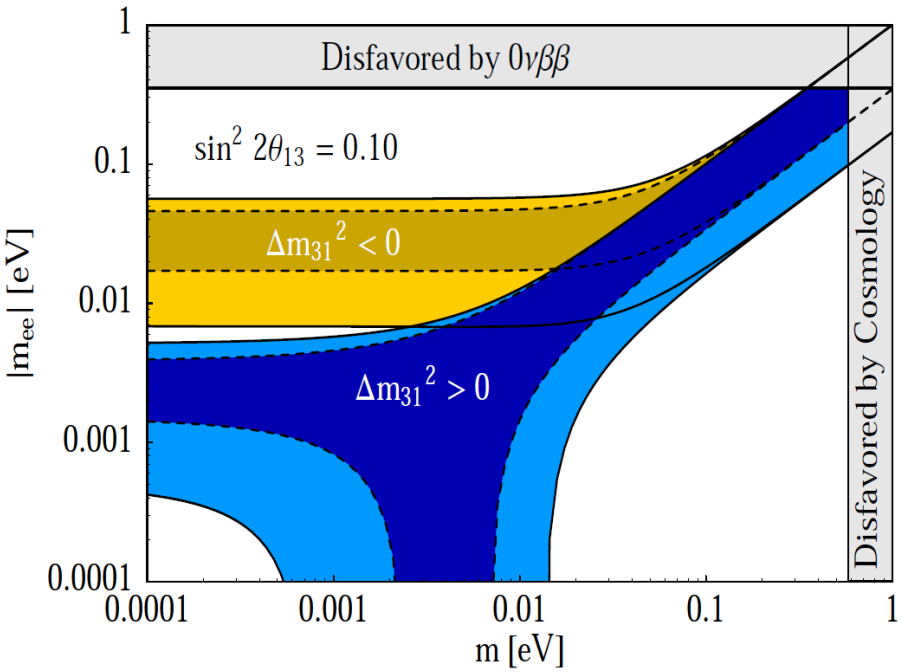

Fig. 1.4 Effective Majorana neutrino mass $\pm 1\sigma$ versus lightest neutrino mass $\pm 1\sigma$ for NH (blue) and IH (yellow). Figure is taken from [14].

experimental setups would expect only a few events per year. The number $N_{0\nu\beta\beta}$ of expected events depends on the half-life $T^{0\nu}_{1/2}$ and is given by [15]:

$$N_{0\nu\beta\beta} \cong \ln 2 \cdot \frac{N_A}{M_A} \cdot \frac{M_{tot} \cdot F_{\beta\beta} \cdot t_{life} \cdot \varepsilon_{tot}}{T^{0\nu}_{1/2}} \tag{1.6}$$

where N_A is the Avogadro constant, M_A the atomic mass of the double beta isotope, M_{tot} is the total mass of the source material, $F_{\beta\beta}$ is the fraction of the double beta decay isotope, t_{life} is the life time, ε_{tot} is the total signal detection efficiency which consists of:

$$\varepsilon_{tot} = \zeta_{av} \cdot \varepsilon_E \cdot \varepsilon_{cut} \tag{1.7}$$

The active volume fraction of the detector ζ_{av}, the energy detection efficiency in the $Q_{\beta\beta}$ energy region of interest ε_E and the overall signal acceptance efficiency after all cuts ε_{cut}. The first fraction in equation 1.6 consists of physical constants and is thus fixed for a given experimental setup. But the second one shows us directly which parameters influence the sensitivity. It is important to have a high source mass which has a large fraction of double beta decay isotopes, a long measurement time and high signal efficiency. High signal efficiency is

achieved with a big active volume fraction, an efficient energy detection in the $Q_{\beta\beta}$ ROI and a high signal acceptance. It is important that these parameters are as large as possible since the denominator (half-life) is so huge.

1.2.1 Background

Unfortunately, a background free experiment is nearly impossible to create and therefore the influence of background events has to be considered. The number N_{BG} of observed background events scales with the measurement time t_{life}, the total source mass M_{tot}, the resolution dependent energy window ΔE and the background index BI which is normally given in units of counts per keV·kg·yr.

$$N_{BG} \cong BI \cdot t_{life} \cdot M_{tot} \cdot \Delta E \tag{1.8}$$

If we assume a flat distributed background (more than 10 cts) then the number of observed events should be bigger than a $1\sigma = \sqrt{N_{BG}}$ fluctuation of the background. This leads to a sensitivity of:

$$T_{1/2}^{0\nu} = \ln 2 \cdot F_{\beta\beta} \cdot \varepsilon_{tot} \cdot \frac{N_A}{M_A} \cdot \sqrt{\frac{M_{tot} \cdot t_{life}}{BI \cdot \Delta E}} \tag{1.9}$$

This formula directly shows how important an efficient background suppression and a superior energy resolution are for the sensitivity of an experimental setup. It also shows that with background the life time sensitivity scales with the square root of the source mass and measurement time. In a background free experiment that relation would be linear.

1.3 GERDA

The GERDA (GERmanium Detector Array) experiment is based at the underground Laboratory Nazionale del Gran Sasso (LNGS) to shield the experimental setup from cosmic rays in particular from high energy muons. The experimental halls of the laboratory are covered by about 1400 m of rock and are connected by a 10 km long motorway tunnel running through the Gran Sasso ridge (see fig. 1.5). The basic idea of the experiment is to use the same material for the source and the detector to gain maximum detection efficiency. For this purpose GERDA uses germanium semiconductor detectors enriched in ^{76}Ge.

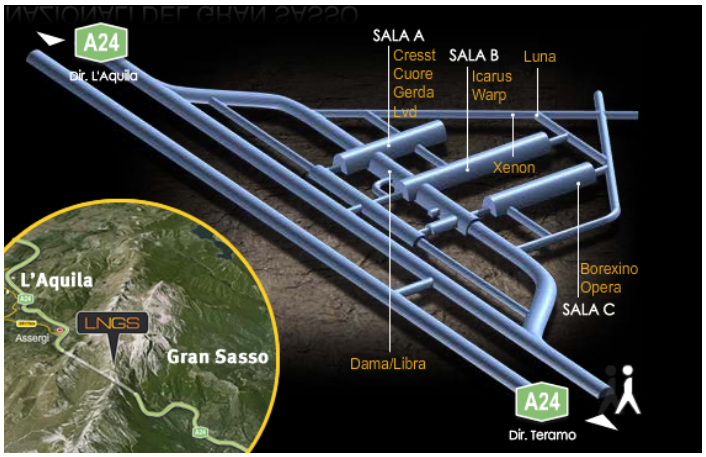

Fig. 1.5 Laboratory Nazionale del Gran Sasso (LNGS) located ca. 130km east of Rome in Abruzzo. Figure taken from [16].

1.3.1 Experimental setup

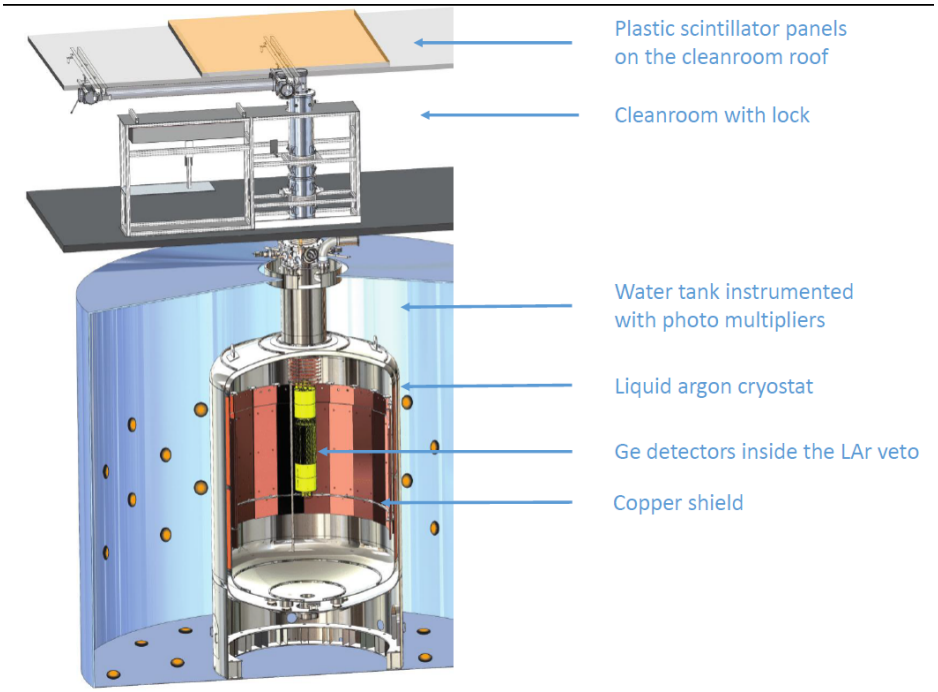

Fig. 1.6 A schematic drawing of the GERDA experiment. Figure is taken from [1].

The overall design follows the "onion shell" principle with the above mentioned germanium detectors as the core (see fig. 1.6). In Phase II GERDA uses 30 BEGe [17] and 10 semi-coaxial detectors. Only 7 of the semi-coaxial detectors are enriched in ^{76}Ge, these detectors were already used by the Heidelberg-Moscow [18] and IGEX [19] experiment. All 40 detectors

are assembled in 7 strings where each string is encapsulated inside a wavelength shifting nylon shroud (see fig. 1.7). The strings are deployed in a cryostat filled with 64 m^3 of liquid argon. The argon serves simultaneously as a cooling medium, a passive shield and an active veto. The scintillation light of the argon caused by radiation is read out by a combined system of classical photomultipliers and light fibers which are read out by SiPMs [20] (see fig. 1.8). The last shell of the apparatus is a 10 m wide and 9.4 m high cylindrical tank filled with 590 m^3 of ultra pure water and is instrumented with 66 (8 inch) photo multipliers which detect the Cherenkov light from incoming muons. Figure 1.9 shows a photograph of the water tank. The walls are covered with a wavelength shifting and reflecting foil to maximize the light detection efficiency. The last part of the structure is a class 100 clean room on top of the water tank which hosts the lock to deploy the detectors into the cryostat filled with liquid argon.

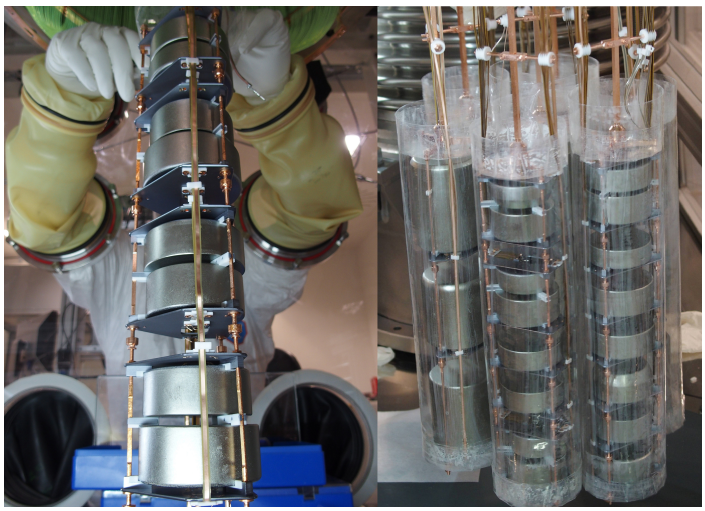

Fig. 1.7 Left: Photograph of a BEGe detector string. Right: Photograph of the seven strings inside the individual nylon shrouds. Photo taken from [16].

1.3.2 Background reduction techniques

As described before, the reduction of the background is essential to guarantee the most effective use of source material and minimize the measurement time. The overburden of 1400 m of rock above the experimental halls is equivalent to 3500 m of water and thus reduces the muon flux by a factor of $\sim 10^{-6}$ to $\sim 3.4 \cdot 10^{-4}$ (muons per m^2 and second). This produces a non tolerable amount of background in the $Q_{\beta\beta}$[1] energy region which is rejected by using the water Cherenkov veto to identify incoming muons and reject coincident

[1] $Q_{\beta\beta}$=2039 keV for ^{76}Ge

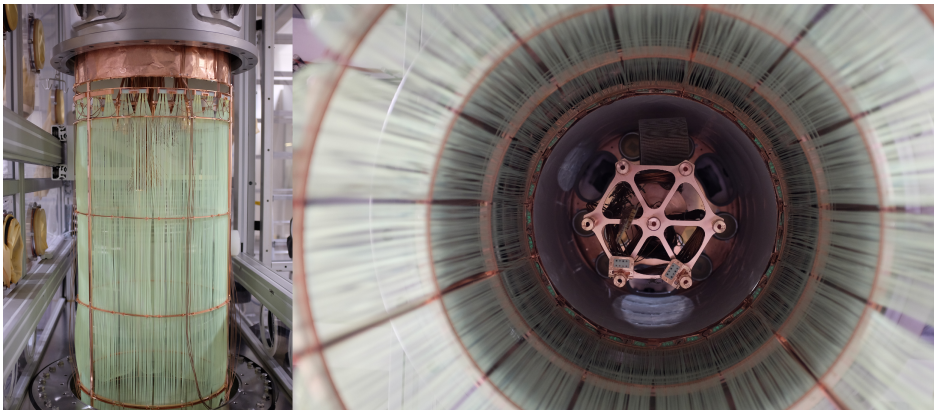

Fig. 1.8 Photograph of the liquid argon veto from deferent perspectives. Photo taken from [16].

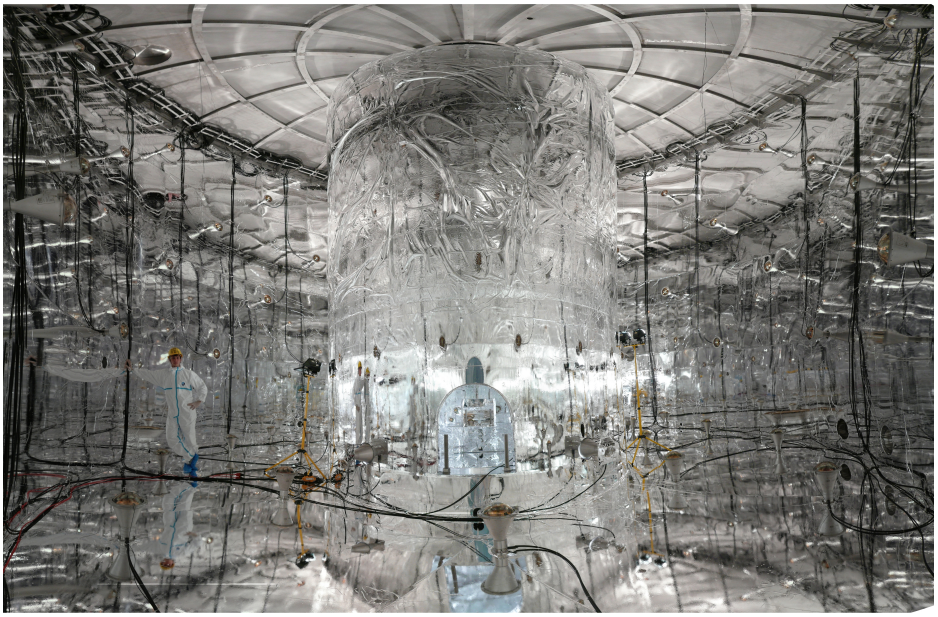

Fig. 1.9 Photograph inside the water Cherenkov veto. Photo taken from [16].

events. The detection efficiency of the muon veto is almost flawless at 99 %[21]. The next step in the active background reduction is the liquid argon veto which rejects events which do not comply with the $0\nu\beta\beta$ event topology, namely the energy deposition in one germanium detector only. Especially events with Compton scattered photons and decays where several particles deposit energy in the detectors and the argon are suppressed this way. This helps to reduce two severe sources of background in the $Q_{\beta\beta}$ region as shown in fig. 1.10. The first one is high energy photons which deposit energy in the detector in a small localized area through Compton scattering and then leave it. These photons mostly deposit energy in the liquid argon and the light produced that way is detected by the veto. The second is events like the ^{42}K β decay where the β is accompanied by a photon. If one of the particles deposits energy in one of the germanium detectors, the deposition of the other one in argon can again be tracked by the scintillation light.

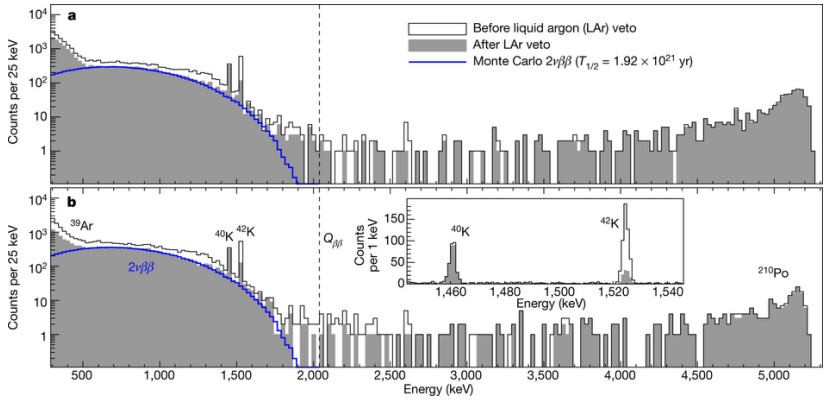

Fig. 1.10 Energy spectra of Phase II data sets before (open histogram) and after (filled histogram) the argon veto cut. Top: Enriched coaxial detectors with a total exposure of 5.0 kg·yr. Bottom: Enriched BEGe detectors with a total exposure of 5.8 kg·yr. The inset: BEGe energy spectrum for the two potassium lines, ^{40}K and ^{42}K. The ^{40}K line shows no suppression since the energy is only carried away by the photon and no energy is deposited in the argon. For the ^{42}K line the suppression is maximal (factor $\sim$5) since the photon is accompanied by a β-particle which deposits its energy in the argon. Figure is taken from [1].

The last step in the analysis is the signature of charge signal of the BEGe detectors. This simple and efficient method, described in section 2.5, allows discrimination between events with single or multiple interaction points in the detector. $0\nu\beta\beta$ events mostly deposit their energy at one site since only β-particles are involved. Background events in the $Q_{\beta\beta}$ region of $\sim$2 MeV mostly show a multisite topology. Figure 1.11 shows the discrimination efficiency of this cut.

Using all the above mentioned techniques GERDA expects an average background of less than 1 count/keV in the region of interest around $Q_{\beta\beta}$ until it reaches its designed exposure of 100 kg yr.

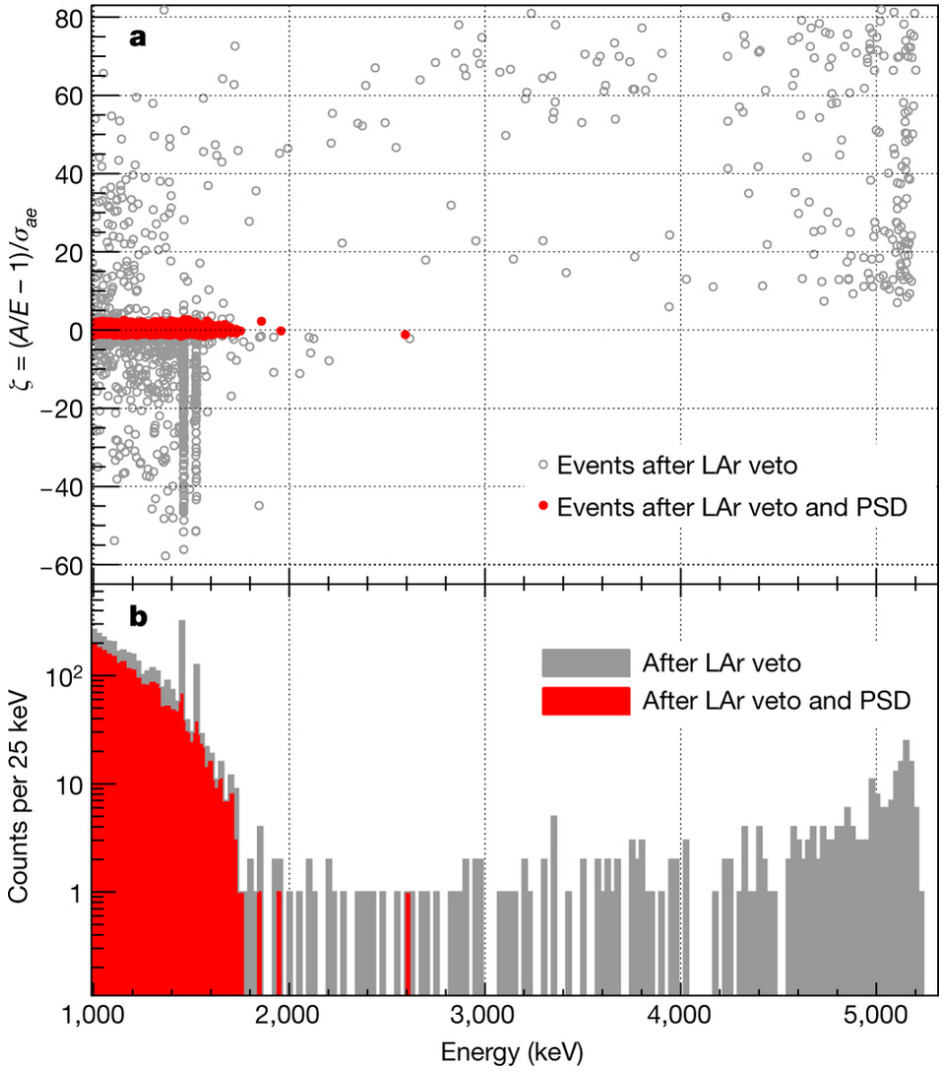

Fig. 1.11 Top: Scatter plot of the PSD parameter ζ vs energy for all BEGe events. Bottom: Energy spectrum for all BEGe events with a minimum deposition of 1000 keV in the Phase II data set. Data in red (circles and histogram) marks the events which have passed the PSD cut. The cut parameter ζ is calculated individually for each detector. Figure is taken from [1].

Chapter 2

Germanium detectors

High Purity Germanium detectors (HPGe) provide a high detection efficiency for β- and γ-radiation paired with a superb energy resolution of several ‰ over a wide energy range. Therefore they are commonly used in industrial applications as also in the field of Nuclear and Particle Physics. Especially new developed types by Canberra [22] and ORTEC [23] with a point-like contact are becoming popular in the rare event and dark matter searches since these detectors offer a low energy threshold because their small capacitance which makes them a candidate for dark matter detection [24]. The inhomogeneous electric field caused by the point-like contact also enables new pulse shape analysis methods for event classification and thus background reduction. A simple and efficient classification method will be introduced in this section along with the working principle of semiconductor detectors and the fundamental physics of radiation interaction with matter.

2.1 Interaction of radiation with matter

For a detailed understanding of the signal formation in a germanium detector, a closer look on the fundamental processes of interaction of radiation with matter and especially the characteristic interaction length is important. In this section a brief overview will be given. A detailed discussion can be found in [25] and [26]. First a distinction between on charged and uncharged radiation is useful.

2.1.1 Charged radiation

Heavy charged particles

Heavy charged particles like ions and α particles interact with matter mainly through the Coulomb force with the electrons of the absorber. The energy transferred to the electrons either excites them to a higher shell or completely remove them from the atom. These interactions transfer only a small fraction of the heavy charged particles initial kinetic energy, maximal 1/500 per nucleon, and therefore happen continuously until the particle is stopped. The specific energy loss along the track is described by the Bragg curve and is nearly linear with the distance until a certain velocity threshold is reached and the energy deposition per distance rise significantly. Since the mass of the primary particle is much larger than the electron mass, no significant deflection takes place and the particle path is close to a straight line. Due to the large number of interactions and the straight path the penetration depth for a given energy is definite and in the range of 10^{-5} m for energies in MeV scale. Since most germanium detectors possess a dead layer (DL) (see. fig. 2.6) in the order of 1 mm, heavy charged particles do not play a role in the standard spectroscopy applications. In specific layouts with high α concentrations close to the thin passivation layer (PL) and bulk contamination with thorium and uranium α particles can also contribute to measured spectra.

β particles

Fast electrons and positrons also interact through the Coulomb force with the electrons of the absorbing material but since the masses of projectile and target are now equal, a much bigger fraction of the energy can be transferred in a single interaction leading to a large deflection. The β particles can also undergo elastic scattering on the nucleus and thus change their direction completely. Therefore the mean penetration depth is generally much shorter than the path length. But as illustrated in fig. 2.1 and 2.2 it can reach up to some mm for β particles with energies in the MeV range and penetrate the DL and deposit energy in the detector.
Since the β particles decelerate during this scattering processes, they can emanate bremsstrahlung along their track. The specific radiative energy loss through bremsstrahlung is given by [25]:

$$-\left(\frac{dE}{dx}\right)_r = \frac{NEZ(Z+1)E^4}{137m_0^2c^4}\left(4ln\frac{2E}{m_0c^2}-\frac{4}{3}\right) \tag{2.1}$$

In the formula N and Z are the density and the atomic number, m_0 is the rest mass of the electron, c the speed of light and E the β particle's energy. Since the radiation energy loss

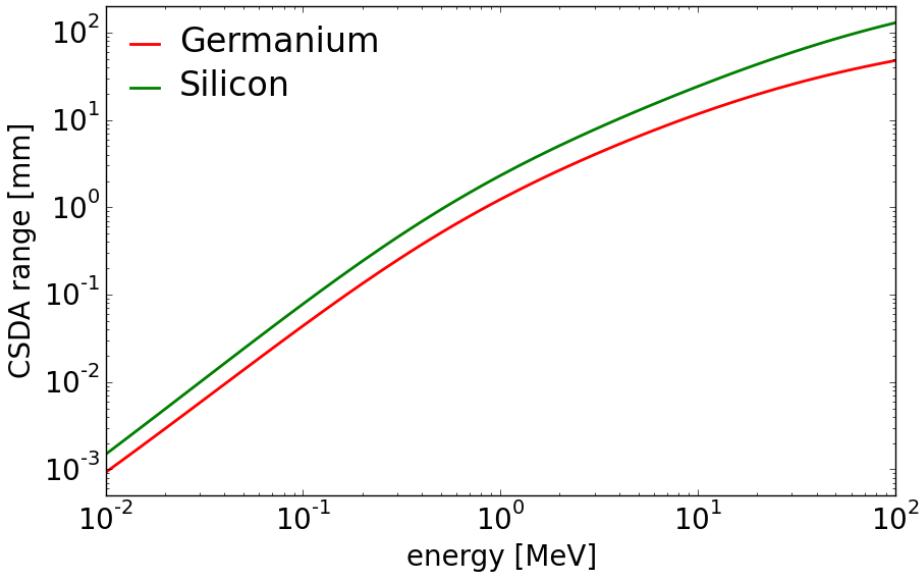

Fig. 2.1 Average path length (continuous slowing down approximation) of electrons in germanium and silicon, data taken from [27].

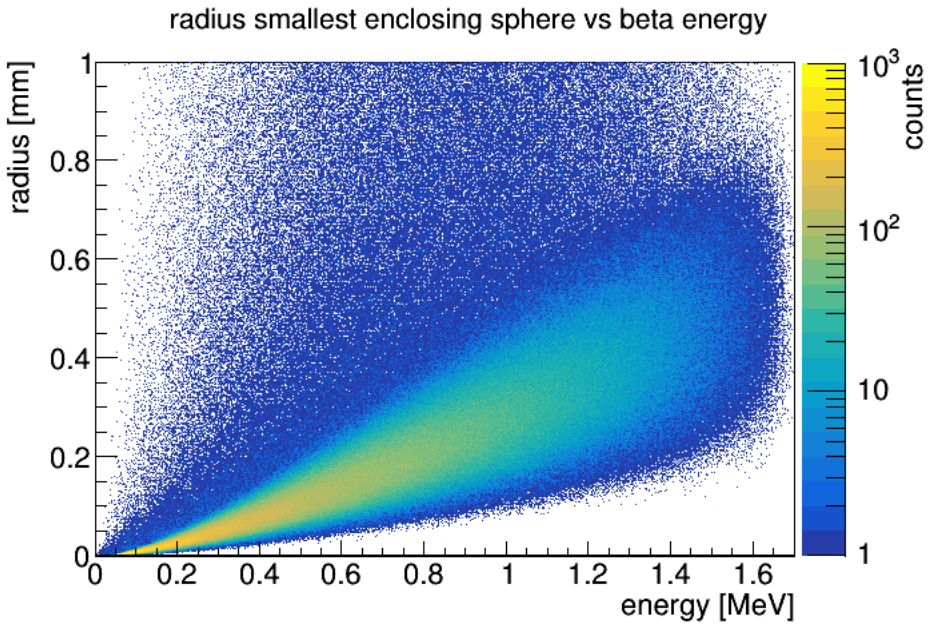

Fig. 2.2 Minimal enclosing sphere around an electron track in germanium plotted versus the initial kinetic electron energy. The interaction points were simulated with MaGe [28] and the sphere radius was calculated with the "miniball" algorithm [29].

is proportional to E^4 and Z^2 bremsstrahlung only plays a significant role for high energy β particles and absorber materials with a high Z. The emitted bremsstrahlung photon can deposit energy in a distant position to the initial interaction point of the β particle. After losing their kinetic energy positrons annihilate with an absorber electron into two 511 keV photons. Since the mean free path for photons is much larger, the energy deposition happens usually far away from the annihilation point. The photons can even leave the detector without any energy deposition.

2.1.2 Uncharged radiation

Photons

Photons interact in a discrete way with the absorber by transferring their energy to a electron, which then deposits the energy in the medium. The three main interactions for the relevant energy range of photons are:

- **Photoelectric absorption**

  During the photoelectric absorption the photon is interacting with the whole atom. The photon disappears and its energy is transferred to a bound electron mostly from the K shell. The photoelectron's energy is given by

  $$E_{e^-} = E_\gamma - E_b$$

  where E_γ is the energy of the incoming γ and E_b is the binding energy of the electron. The photoelectric absorption is dominant for energies smaller than 100-200 keV depending on the Z of the absorber material and its cross-section σ_{pa} is roughly proportional to:

  $$\sigma_{pa} \propto Z^n \cdot E_\gamma^{-3.5}$$

  The exponent n is linked to the gamma energy and varies from 4 to 5. The contribution of the photoelectric absorption to the total attenuation is shown in fig. 2.3.

- **Compton scattering**

  The incoherent scattering of photons on loosely bound outer shell electrons is the dominant interaction in the range of 0.15 MeV and 8 MeV in germanium. The differential

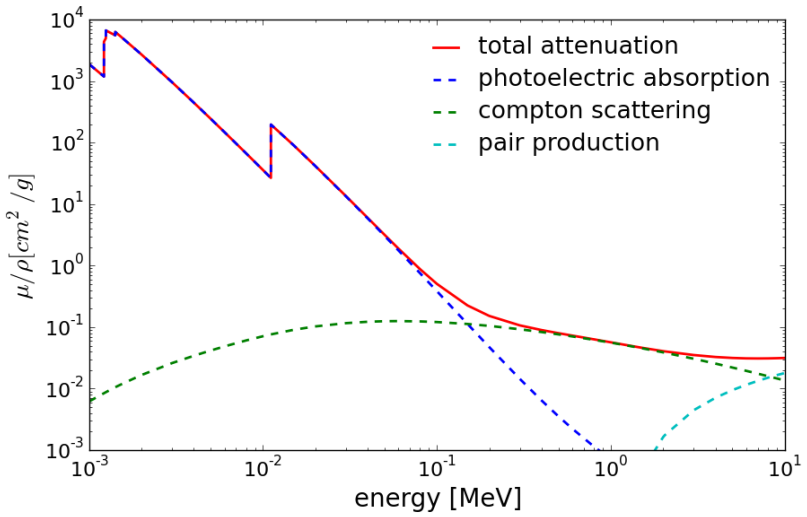

Fig. 2.3 Photon mass attenuation coefficient μ for germanium and its components. The data was taken from the NIST database [30].

cross section for Compton scattering

$$\frac{d\sigma}{d\Omega} = \frac{r_e^2}{2}\frac{1}{(1+\gamma(1-cos\theta))^2}\left(1+cos^2\theta+\frac{\gamma^2(1-cos\theta)^2}{1+\gamma(1-cos\theta)}\right), \quad \gamma = \frac{h\nu}{m_e c^2} \tag{2.2}$$

and the energy transfer to the electron

$$\frac{d\sigma}{dE_e} = \frac{\pi r_e^2}{m_e c^2 \gamma^2}\left[2+\frac{s^2}{\gamma^2(1-s)^2}+\frac{s}{1-s}\left(s-\frac{2}{\gamma}\right)\right], \quad s = \frac{E_e}{h\nu} \tag{2.3}$$

are described through the *Klein-Nishina* formula [26] with r_e as the classic electron radius, m_e the electron mass and E_e its energy. The maximum recoil energy of the electron

$$E_e^{max} = h\nu\left(\frac{2\gamma}{1+2\gamma}\right)$$

is given when the gamma is deflected by 180°. Most high energy photons undergo multiple Compton scattering until they either leave the medium or reach the energy region of photo absorption. Thus they deposit their energy in multiple locations in a detector.

- **Pair production**

  Photons excess the energy twice of the electron mass (1.022 MeV) can produce an electron-positron pair while interacting with the coulomb field of the nuclei. The probability for pair production increases with the photon energy and is the dominant effect for high energy photons above 8 MeV in germanium. All the energy is transferred to the electron-positron pair. After slowing down, the positron annihilates with a surrounding absorber electron and produces a photon pair with 0.511 MeV each. These photons then can either escape or also deposit their energy in the absorber. This effect leads to additional characteristic peaks in the measured spectrum of germanium detectors and are used in the pulse shape calibration procedure. If both photons escape, the initial photon energy minus the 1.022 MeV is deposited in the detector within a small volume and the Double Escape Peak (DEP) is visible in the spectrum. Since the energy is deposited only by β particles, the interactions are happening in one spot ($\sim$1 mm^3). These events are called Single Site Events (SSE). If only one γ escapes, the Single Escape Peak (SEP) is created. Since the mean free path for a 0.511 MeV photons is $\sim$1 cm, the energy deposition mostly happens in at least two locations. These events are called Multi Site Events (MSE). A sample spectrum is shown in fig. 2.4.

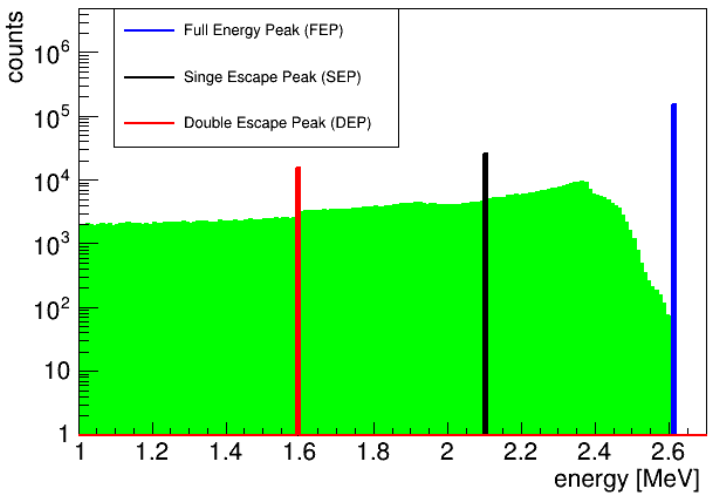

Fig. 2.4 Simulated spectrum for the 2.6 MeV line of ^{208}Tl with the Full Energy Peak in blue, the Single Escape Peak in black and the Double Escape Peak in red.

2.2 Semiconductor detectors

The semiconductor detectors' working principle is that of an ionization chamber. Incoming radiation deposits energy by creating electron-hole pairs which are then collected at the electrodes. These moving charges induce a signal on the electrodes. In this section a short summary of the basic semiconductor properties like band structure, charge carriers and p-n junction will be given. A detailed description can be found in [25], [26] and [31].

- **Band structure**

  Germanium forms a diamond cubic crystal structure in which the individual electron wave functions for the outermost shell overlap and thus form a band like structure. In a semiconductor the last occupied band in the ground state, the so called valence band, is separated only by $\sim 1\,\mathrm{eV}$ (germanium: $0.7\,\mathrm{eV}$) from the first unoccupied band, the so called conduction band. This two bands overlap in metals, whereas insulators have a bigger gap with a gradual transition to semiconductors.

- **Charge carriers**

  Through thermal excitation or incident radiation an electron can gain enough energy to overcome the band gap in a semiconductor and move from the valence into the conduction band. The excited electron leaves a vacant state in the valence band which is called "hole". This state can then easily be filled by a neighboring valence electron creating another hole. In this way the vacant state behaves like a positive charge carrier and moves through the crystal. Since germanium is an indirect semiconductor, the highest energy state in the valence band does not have the same wave vector as the minimum energy state in the conduction band, therefore an electron from the conduction band can not occupy a vacant state in the valence band by just emitting a photon. A phonon needs to be absorbed to satisfy momentum conservation. This lowers the recombination probability of holes and electrons and leads to long lifetimes ($\sim 1\,\mathrm{s}$) for charge carriers. Present impurities can shorten this lifetime significantly by acting as recombination centers through trapping the charge carriers. This can affect the detector performance.

- **Doping**

  In intrinsic semiconductors electron-hole pairs are generated by thermal excitation. The temperature dependent creation probability $p(T)$ is given by the Fermi-Dirac

distribution and is proportional to

$$p(T) \propto T^{3/2} exp\left(-\frac{E_{bg}}{2kT}\right)$$

where E_{bg} is the band gap and k the Boltzmann constant. Since the band gap of germanium with 0.7 eV is large compared to the thermal energies at room temperature (~ 0.026 eV), this results in $\sim 2.4 \cdot 10^{13}$ charge carriers per cm^3. Real semiconductor material always has a remaining concentration of impurities from the manufacturing process or is intentionally doped. The type of the dominant impurities defines if the semiconductor is n- or p- type. In n-type material the 4th group germanium atom is replaced by one from the 5th group (donor). The 5th valence electron of this substitute does not participate in the covalent lattice bonding and thus is only lightly bound to the donor atom and its energy level is slightly lower (~ 0.01 eV) than the conduction band. This electron can easily move to the conduction band by thermal excitation. In p-type material the substitute is a member of the 3rd group (acceptor), which leads to a missing electron in the covalent bonding. This introduces a new energy level around ~ 0.01 eV above the valence band which can be occupied by an thermally excited electron from an adjacent germanium atom. This process generates a vacancy in the valence band and thus creates a hole.

- **p-n junction**

  A p-n junction is created by connecting a p- and n-type semiconductor. This can be achieved in a crystal through doping. Mostly a strong asymmetric doping is used for detector production and consequently a lightly doped bulk material is therefore heavily doped on the edges with the opposite impurity. At the junction electrons from the n-type and holes from the p-type material drift to the other site and recombine, leaving a free charge depleted zone. Since their mother atoms are fixed in the lattice, positive and negative ions are left behind and create an electric field. This electric field limits the diffusion until an equilibrium is reached. By applying a reverse bias (e.g. positive potential on the n-type site) to the junction, this depletion region can be extended over the whole bulk.

2.3 Signal formation

Electron-hole pairs created by incident radiation in the depleted volume move parallel to the electric field towards the electrodes. Holes move towards the p^+-electrode and electrons

towards the n^+-electrode (see chapter 3.2.1). These moving charges q induce a charge Q on the electrodes which is converted to a voltage pulse through a charge sensing amplifier. See fig. 2.5.

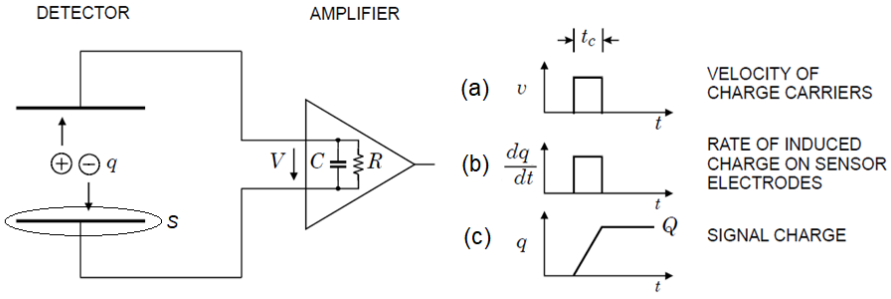

Fig. 2.5 Schematic drawing of a detector as a capacitor. (a) illustrates the charge velocity, (b) the induced current and (c) the induced charge on the readout electrode. Taken from [32]

The time dependent signal on the readout electrode can be calculated as a function of the moving charge q within the detector volume. The Gauss law relates the total charge Q inside a volume, in our case the electrode, to the flux of the electric field through the surface S enclosing this volume:

$$Q = \oint_S \varepsilon \vec{E}(\vec{x}) \cdot d\vec{S} \tag{2.4}$$

where ε is the dielectric constant of the medium, $\vec{E}(\vec{x})$ the electric field and S the enclosing surface of the electrode volume. The calculation of this integral for each given time t along the drift path of the moving charge q gives the time profile of the induced charge Q on the electrode. Since the electric field $\vec{E}(\vec{x})$ needs to be calculated for each position of q individually this is very tiresome and computing time consuming.

A simple approximation for the quasi-steady[1] case was introduced independently by Shockley [33] and Ramo [34]. This approximations uses a weighting potential $\phi_0(\vec{x})$ and weighting field $\vec{E}_0(\vec{x})$ to calculate the induced charge Q and the corresponding current i. They are linked through the following equations:

$$Q = -q \cdot \phi_0(\vec{x}) \tag{2.5}$$

[1] In semiconductors the quasi-steady case is valid since the speed of light is much higher than the drift velocity of charge carriers

$$i = q\vec{v} \cdot \vec{E}_0 \tag{2.6}$$

where $\vec{v}$ is the velocity of the moving charge q. Now just the trajectories and one field need to be calculated to determine the signal.
The basic idea of this approximation is to split the electric potential $\phi(\vec{x})$[2] into three parts:

$$\phi(\vec{x}) = \phi_0(\vec{x}) + \phi_S(\vec{x}) + \phi_q(\vec{x}) \tag{2.7}$$

with

$$\begin{aligned} \nabla^2\phi_0(\vec{x}) &= 0, & \phi|_S &= V \\ \nabla^2\phi_S(\vec{x}) &= -\rho(\vec{x})/\varepsilon, & \phi|_S &= 0 \\ \nabla^2\phi_q(\vec{x}) &= -q \cdot \delta(\vec{x} - \vec{x_q})/\varepsilon, & \phi|_S &= 0 \end{aligned} \tag{2.8}$$

The first term $\phi_0(\vec{x})$ represents the potential caused by the voltage on the electrode and no space charge present. The second term $\phi_S(\vec{x})$ is the potential generated only by the stationary space charges and the electrode on ground. And the third one $\phi_q(\vec{x})$ is the potential caused by the moving charge itself.
This results in the following equation for the induced charge Q:

$$Q = \oint_S \varepsilon\vec{E}_0 \cdot d\vec{S} + \oint_S \varepsilon\vec{E}_S \cdot d\vec{S} + \oint_S \varepsilon\vec{E}_q \cdot d\vec{S} \tag{2.9}$$

Now its clearly visible that only the third term relates to the moving charge q and thus the induced charge Q only depends on the configuration of the device (the first two terms) and the location of the moving charge.
A full review of the Shockley-Ramo theorem and its extension to semiconductor detectors with present space charges can be found in [35].

2.4 High Purity Germanium detectors

The production of high purity germanium crystals with a low impurity concentration of $\sim 10^{10}$ per cm^3 enables the realization of large volume diodes with a feasible depletion voltage ($\sim$5 kV). There are two main types available on the market: First the so-called

[2] Which satisfies Poisson's equation with the Dirichlet boundary condition:

$$\nabla^2\phi(\vec{x}) = -[(\rho(\vec{x}) + q \cdot \delta(\vec{x} - \vec{x_q})]/\varepsilon), \qquad \phi|_S = V$$

where V is the potential on the electrode and $\rho(\vec{x})$ the stationary space charge density.

semi coaxial geometry where one electrode is realized through a bore hole in the middle of the cylinder, see fig. 2.6. These detectors can reach a mass of up to 3 kg. In the second configuration the p^+-electrode is realized through a point-like contact on the base. The n^+-electrode is produced by lithium diffusion and covers the mantle and top surface of the detector. This kinds of detector can reach a mass of 1 kg but are usually in the range of 500-850 g. Using a point-like contact minimizes the capacitance of the detector and thus reduces the electronic noise. This leads to a superior energy resolution and a lower energy threshold. The use of a point like contact results in a strong inhomogeneous electric field concentrated around it. This field configuration enables an event classification through pulse shape analysis described in section 2.5. Two designs by the leading manufacturers Canberra and ORTEC are presented in detail in the following subsection.

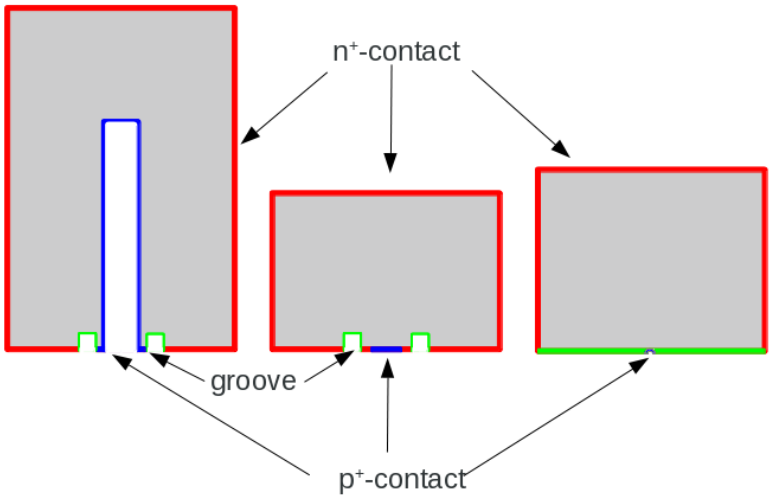

Fig. 2.6 Schematic drawings of semi coax (left), BEGe (middle) and ORTEC PPC (right) detectors. The lithium diffused n^+-contact is drawn in red, the p^+-contact in blue and the passivation layer in green.

2.4.1 BEGe (Broad Energy Germanium detectors)

The BEGe detectors are produced by Canberra Industries. The ingots are pulled by Canberra Oak Ridge and the individual detectors are then manufactured in different branches, therefore the detector designs vary. BEGes are made from p-type crystals with a lithium diffused n^+-contact of approximately 1 mm thickness [36] which covers the whole top and mantle of the detector and most of the bottom, see fig. 2.6. This makes the detector easy to handle since this so called dead layer is robust against light mechanical force. The p^+-contact is

realized via boron implantation on the base of the crystal and has a thickness of only 0.2 μm. Its diameter varies between 6 mm and 15 mm. Both contacts are separated by a several millimeter thick groove around the p^+-contact. In order to minimize the leakage current, the surface in the groove is passivated with silicon oxide or amorphous germanium. The exact properties and the manufacturing process of this passivation layer is the company's secret.

2.4.2 p^+ Point Contact detectors from ORTEC

Point contact detectors produced by ORTEC are 25 mm to 50 mm high and have a diameter of 60 mm to 70 mm. The average mass of the detectors manufactured for the MAJORANA Demonstrator is 840 g with a mean impurity concentration of $7 \cdot 10^{10}$ per cm^3 [37]. This purity of crystals allows to keep the operational voltage under 5 kV despite the large mass. The ORTEC detectors have a smaller p^+-contact compared to the BEGes with 3.6 mm diameter and do not have a groove around it. Here the full base of the detector is passivated. This area is very sensitive, since any damage or contaminations of the passivation layer can lead to an increasing leakage current. The characterization results for the first two prototype detectors from ORTEC will be discussed in chapter 5.

2.5 Pulse shape discrimination

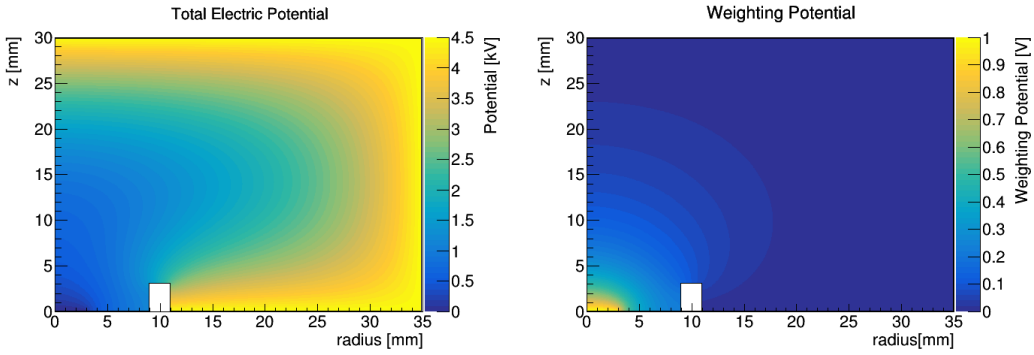

Fig. 2.7 Simulated electric (left) and weighting (right) potential for a BEGe detector

The small point-like contact produces a localized weighting potential, as shown in fig. 2.7. The electrons created in the bulk are drawn to the n^+-contact and contribute little to the induced charge on the electrodes since they do not pass through the strong weighting potential. Due to the electric field configuration in BEGe detectors the holes are first drawn to the middle of the crystal before they are collected at the p^+-contact with the strong weighting potential. This is the so called funneling effect [38]. This leads to similar pulse shapes for the

current pulse of single site events independent of the interaction point since the main rise of the pulse is created close to the point contact. Multi site events can be seen as a superposition of single site events and since these have a different drift length for the individual interaction points the current pulse shows multiple peaks as shown in fig. 2.8. The ratio of the maximum of the current pulse (A) and the amplitude of the charge pulse (E) is constant for single site events in a wide energy range and thus provides an easy possibility to distinguish between multi and single site events. (See fig. 2.9.) Other event classes like slow pulses and events close to the p^+-contact can also be identified by this parameter. Slow pulses which are often created by β particles in the n^+-layer have a large charge cloud size which results in a degraded A/E. Events with an energy deposition inside the strong weighting potential have a larger A/E value than a SSE since here also electrons contribute to the signal. Alpha contamination inside the groove and on the p^+-contact can create such events.

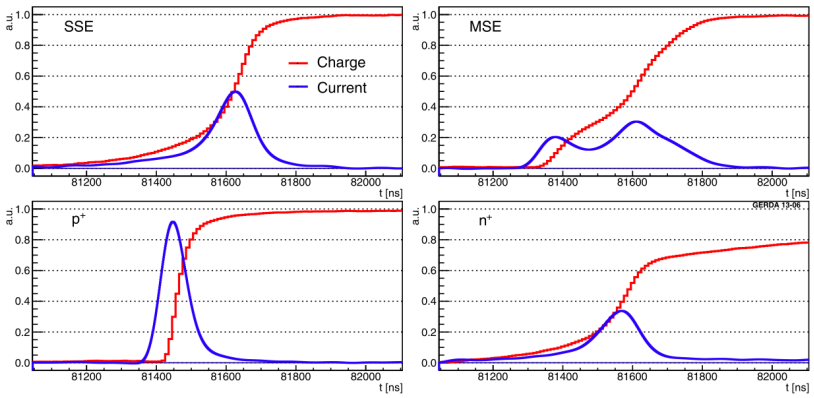

Fig. 2.8 Example pulse shapes for different event classes: Top Left: Single Site Event, Top Right: Multi Site Event, Bottom Left: p^+-contact event, Bottom Right: Slow pulse, originating from the n^+-contact. From [38].

A source with a gamma energy greater than 2 MeV is usually used to calibrate the pulse shape discrimination parameter A/E since the single and double escape peak from pair production, as described in subsection 2.1.2, provide excellent samples for single and multi site events. Fig. 2.10 shows the A/E parameter for these two classes. Events in the DEP are mostly SSE and the A/E parameter shows a peak around the maximum A/E value with a small tail to lower values which are due to multi Compton scattered events. The SEP is mostly populated by MSE and thus has a broad distribution from the minimum to maximum A/E value. The small peak at the maximum is caused by the single Compton events. A detailed description of the procedure can be found in [39].

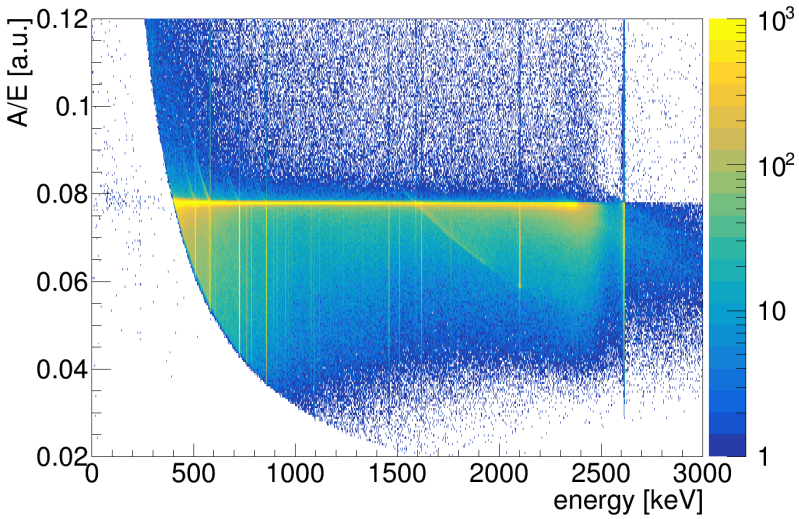

Fig. 2.9 A/E vs energy scatter plot for a BEGe. The SSE band is clearly visible at the A/E value of ~ 0.078 [a.u.]. MSE and slow pulses are populating the area below and events close to the p^+-contact the area above the SSE band.

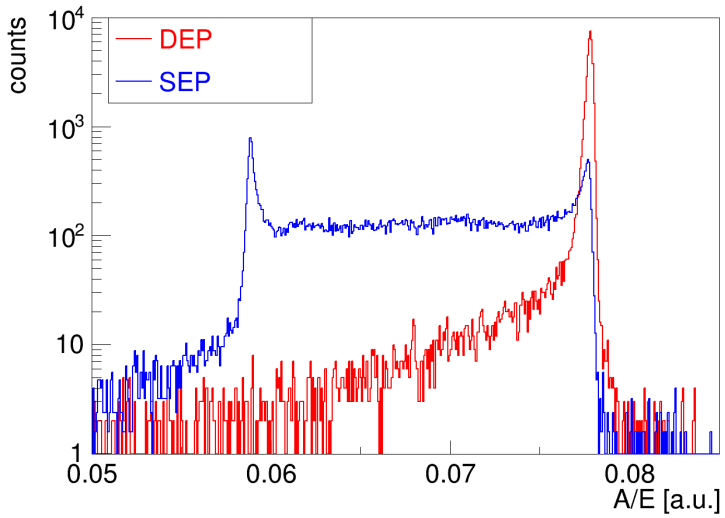

Fig. 2.10 A/E classifier for the SSE dominated DEP (red) and the MSE dominated SEP (blue)

Chapter 3

Pulse shape simulation

For the simulation of the germanium detector pulses discussed in the next two chapters two software packages were used. The MaGe framework [28] which calculates the interaction points of ionizing radiation inside the crystal and the `mjd_siggen` package [2] which generates the corresponding pulse. The first step is the calculation of the electric and weighting potential by the standalone code `mjd_fieldgen` [2]. Second is the calculation of the drifting trajectories of the charge carriers and the induced signal using the Shockley-Ramo theorem introduced in section 2.3.

3.1 Field simulation

The electric potential $\Phi(\vec{x})$ for a given detector geometry is given by the Poisson equation:

$$\nabla^2\Phi(\vec{x}) = -\frac{\rho(\vec{x})}{\varepsilon_0\varepsilon_r} \tag{3.1}$$

with the net impurity distribution $\rho(\vec{x})$, the vacuum permittivity ε_0 and the permittivity of germanium $\varepsilon_r = 16$. The electric field $\vec{E}(\vec{x})$ is then given by the gradient of the electric potential. The weighting potential $\phi_0(\vec{x})$ corresponds to the electric potential of a space charge free detector and the read out electrode on unit potential. The geometries of the existing detectors are not trivial and thus the fields and potentials are calculated numerically on a regular grid via a relaxation algorithm. Since the detectors have a rotational symmetry, the potential calculation can be reduced to a 2 dimensional problem using the cylinder coordinates. The grid size can be adjusted for the precision needed in the simulation. To converge, the relaxation algorithm needs boundary conditions. These are given by the n^+- and p^+-contact. The passivation layer on the base of the ORTEC PPC detectors and the

inside of the groove of BEGe detectors is treated in a way that reflection symmetry is given. This means that the electric field is parallel to the passivated surface if no surface charge is present on it. In case of BEGe detectors, which have a groove around the p^+-contact, the different permittivity of vacuum is taken into account in the calculations.

Besides the bias voltage and the detector geometry, the electric potential and field depend on the spatial net impurity distribution. (See fig. 3.1) This is usually measured by the manufacturer on the top and bottom of each ingot slice. A linear dependency in z-direction is used in most cases and is sufficient to reproduce the measured results. More complicated distributions like a radial dependence or space charges on the passivated surface are included in the code for special cases and are used in section 4.6.

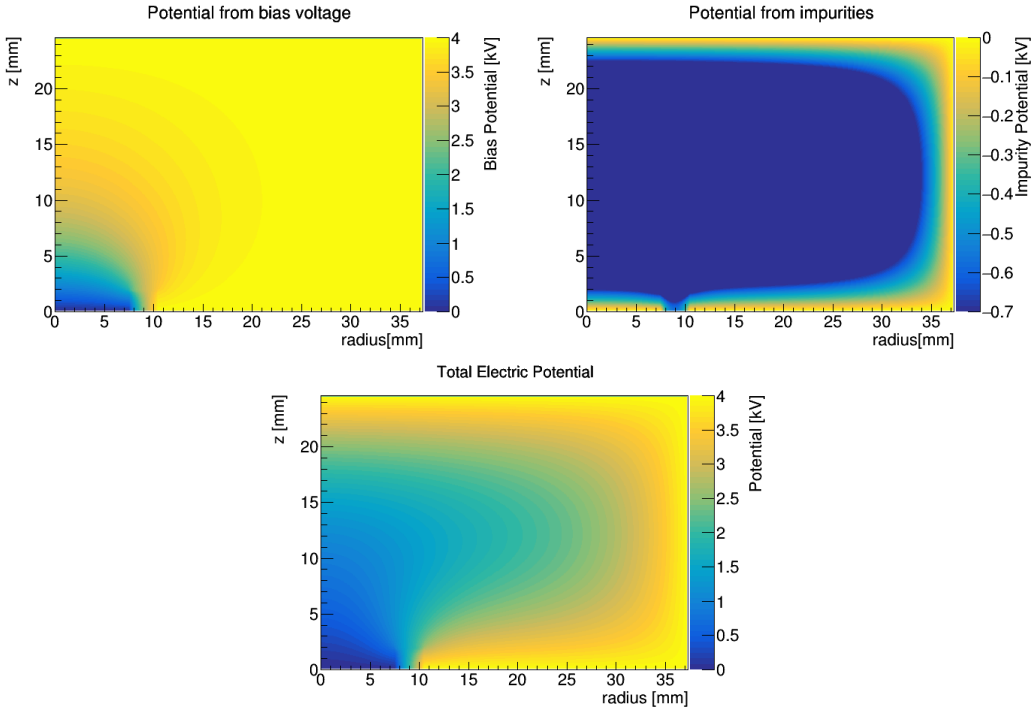

Fig. 3.1 Simulated total electric potential (bottom) and its components: Bias potential (left) and impurity potential (right).

One key feature of `mjd_fildgen` is the proper handling of undepleted regions for the electric potential calculation since it finds them iteratively inside the detector volume. They are indicated as local minima/maxima for p/n-type material in the potential from the impurity concentration. If an undepleted voxel occurs during the calculation, its space charge is set to zero. Undepleted regions connected to the read out electrode are handled as its extensions and unconnected ones do not have an electric field inside them and thus trap the charge

carriers. Both cases are taken into account for the calculation of the electric and weighting potential and thus allow a realistic simulation of detectors with undepleted regions.

3.2 Signal generation

For the signal calculation the charge carrier drift trajectories as a function of time and the weighting potential are needed. Under special circumstances also the charge cloud size and its evolution with time can play a significant role. Finally the electronic response of the preamplifier needs to be taken into account to simulate the final pulse. In `mjd_siggen` this is done by a simple RC-integration time constant. In the following subsection the individual effects will be described in detail.

3.2.1 Charge carrier drift

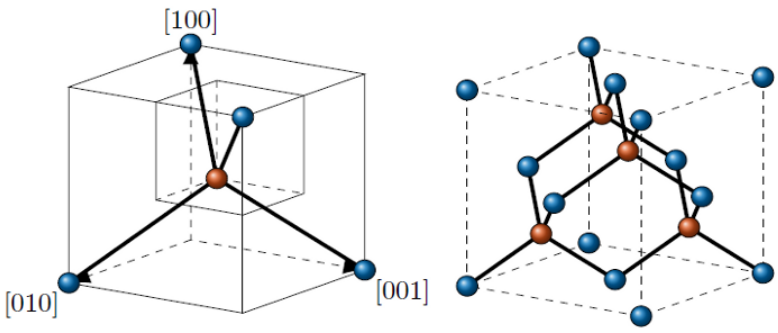

Fig. 3.2 Diamond lattice structure of germanium with one atom at the center of the cell and four others tetrahedrally bonded around it. Taken from [40].

Germanium has a diamond lattice structure configuration as shown in fig. 3.2 with the following crystallographic directions <100>, <110> and <111> by Miller indices [41][42]. Since the charge carrier mobilities are anisotropic along the different axis orientations [43][44], the drift velocities are not parallel to the electric field unless the field is aligned with one of them. The velocity $\vec{v}_{e/h}$ is thus connected to the electric field $\vec{E}$ via a mobility tensor $\mu_{e/h}$ [25]:

$$\vec{v}_{e/h} = \hat{\mu}_{e/h} \cdot \vec{E} \tag{3.2}$$

From measurements, an empirical formula for the drift velocities at liquid nitrogen temperature (∼77 K) was derived by Omar and Reggiani [45] and modified for high electric fields by Mihailescu [46]:

$$v_{exp} = \frac{\mu_0 E}{\left(1 + (E/E_0)^{\beta}\right)^{1/\beta}} - \mu_n E \tag{3.3}$$

with μ_0 as low field mobility and μ_n as the high field mobility correction (which normally does not play a role in germanium detectors since the fields are below 300 $\frac{V}{mm}$) and the fitting parameters β and E_0. Fig. 3.3 shows the velocities used in the `mjd_siggen` package for the drift simulation. It uses a charge-drift model [47] developed by I-Yang Lee for `GRETINA` [48] in which the irrotationality condition [1] the velocity tensor is used to calculate the effect of the axis orientation. Further simulated and measured values were gathered by Bruyneel et al. for the AGATA collaboration and can be found in [49] [50].

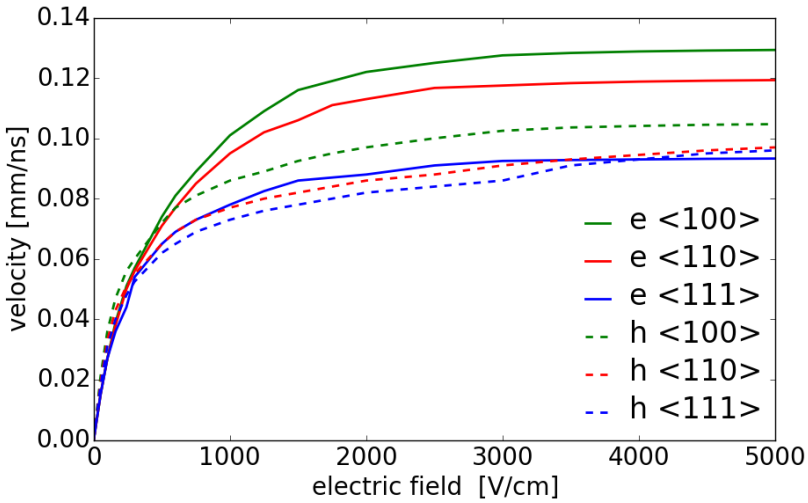

Fig. 3.3 Calculated velocities along different crystal axis in germanium: solid lines for electron, dashed lines for holes.

3.2.2 Charge carrier cloud size

As shown in chapter 5 the final charge cloud size can have a major impact on the signal pulse shape for detectors with low electric field regions. The charge cloud size is modified by three major effects during its drift to the read out electrode. The first effect is the self-repulsion of the electrons and holes after the separation of both clouds due to the different drift directions.

[1] $\nabla \times \mathbf{v} \equiv 0$

This effect depends on the charge density of the initial cloud and thus on the deposited energy at each interaction point. For the further expansion of the charge cloud radius in the longitudinal direction, the electric field of the detector and the charge cloud itself are taken into account. A detailed study of this effect for electrons can be found in [51].
The second effect is the thermal diffusion of the cloud through time. The distribution is approximated with a Gaussian function with the standard deviation $\sigma = \sqrt{2D_{e/h}t}$, where $D_{e/h}$ is the diffusion coefficient and t the elapsed time [25]. The diffusion coefficient can be estimated by the following relation $D_{e/h} = \mu \frac{kT}{e}$ where k is the Boltzmann constant, T the temperature, e the electric charge and μ the mobility for holes and electrons. A diffusion coefficient of $D_{e/h} \approx 400 \frac{\mathrm{cm}^2}{\mathrm{s}}$ in germanium at 77K was measured by Jacoboni et al. [52] and is used in the simulations.
The third effect is caused by the acceleration and deceleration of the charge cloud along the drift path through the electric field. Especially in low fields this effect can lead to a big increase of the longitudinal charge cloud size. The trailing time t_0 between the leading and trailing charges from the same cloud is fixed by the initial longitudinal size S_0 and the velocity v_0 at the energy deposition point. The longitudinal charge cloud size S_f at the read out contact is then given by the final velocity v_f after the acceleration through the high electric field close to the contact and the trailing time t_0.
The charge cloud size is constantly computed for each time step along the trajectory, taking all effects into account. Their individual contributions are added in quadrature to calculate the final FWHM of the charge cloud. For the time-domain convolution function of the signal only the dominant longitudinal charge cloud size is used. The increase of the transversal size is smaller since it is not affected by the acceleration effect.

Chapter 4

BEGe characterization

In Phase II the GERDA experiment is using BEGe detectors to increase its target mass to 35.8 kg. This chapter will give a brief overview on the production cycle of these detectors and describe in detail their testing procedure and the facility used for it. The obtained results and observed effects will be discussed and modeled by a pulse shape simulation.

4.1 Detector production

The thirty BEGe detectors for the GERDA Phase II setup were manufactured by Canberra Semiconductors N.V. Olen, Belgium [53]. Before that, the germanium was enriched in ^{76}Ge from its natural abundance of 7.8% to approximately 87 % in the Production Association Electrochemical Plant (ECP) in Zelenogorsk, Russia [54]. The first step in this process is the fluorination of ^{nat}Ge to $^{nat}GeF_4$ and after that this gas can than be enriched through centrifugation. Afterwards it is converted through hydrolysis to $^{nat}GeO_2$. A total sum of 53.4 kg of $^{enr}GeO_2$ was produced in 2005, which corresponds to 37.5 kg of ^{76}Ge. [17]. The 4N (99.99%) purity grade $^{enr}GeO_2$ was then reduced under a H_2 atmosphere to metallic germanium and after that zone-refined by PPM Pure Metals GmbH, Langelsheim, Germany [55]. This purification process leads to a purity level of 6N with a yield of 94.5%. Fig. 4.1 is showing the metalized enriched germanium.
After further zone-refining to 11N material, nine crystal ingots were grown in two batches by Canberra Inc. [22], Oak Ridge (TN), USA. These were cut to a total of thirty slices with the following specifications: diameter 75 ± 5 mm and height of 30^{+10}_{-5} mm. Since the ingots taper to the tail and seed ends (see fig. 4.2), nine of the slices are conical to ensure a maximum yield of the ^{enr}Ge. The remaining 21 slices are cylindrical. (see fig. 4.3).
Three of the slices do not satisfy the specifications: two slices have a smaller diameter with 68.9 and 66.4 mm and one slice is only 23.3 mm high. The following steps were performed

Fig. 4.1 Photograph of the ^{enr}Ge after zone-refinement. Photo taken from [16].

Fig. 4.2 Photographs of a germanium crystal. Photo taken from [16].

Fig. 4.3 Left: A cylindrical crystal slice. Right: A cone-shaped crystal slice. Photo taken from [16].

by Canberra Semiconductors N.V. in order to turn the crystal slices to functional detectors. The outer n^+ electrode is manufactured through lithium diffusion. The crystal slices are heated up to a temperature of 200-500 $°C$ and exposed to a solution containing lithium. The thin p^+ point-like contact is produced by boron implantation. To ensure an isolation between the electrodes a 1-2 mm deep groove was drilled around the point like contact and passivated with silicon oxide.

4.2 HEROICA @ HADES

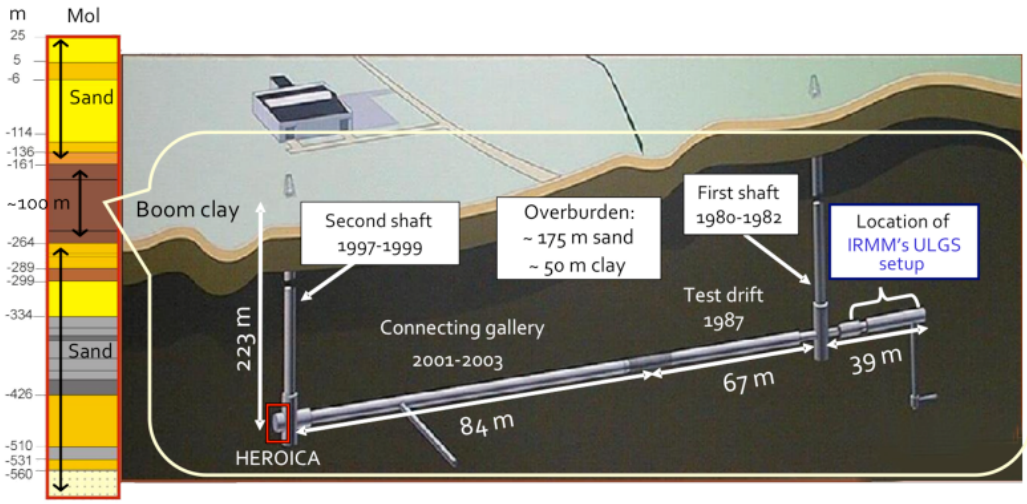

Fig. 4.4 Layout of the HADES facility, the HEROICA test site is highlighted in red. Taken from [56]

The HEROICA (Hades Experimental Research Of Intrinsic Crystal Appliance) [57] project site is located at the HADES (High Activity Disposal Experimental Site) Underground Research Laboratory [56] in Mol, Belgium. The site lies 223 m below surface in a 'bloom clay' layer. This overburden corresponds to ca. 500 meter water equivalent and reduces the cosmic muon flux by four orders of magnitude to $10^{-1}\mathrm{m}^{-2}\mathrm{s}^{-1}$ compared to see level [58]. The close geographical proximity to the manufacturer and the high suppression of the cosmic rays turn HADES into a perfect storage and test site for the new enriched detectors.
To fulfill this task a full testing infrastructure was built. This consists of two fixed calibration measurement setups and three fully automated scanning systems, which will be described in more detail in the next subsection. An analog and digital DAQ system as well as a public server were installed to provide remote access. In order to minimize the noise level in the detectors a new damped floor was built and all electronic devices were grounded. More

detailed information on the test site can be found in the dedicated paper [57].
The purpose of the HEROICA project was to measure the following key specifications:

- depletion and stable operational voltage, the latter should be ≤ 4 kV
- energy resolution, should be smaller than 2.3 keV FWHM at 1.33 MeV
- leakage current, should be smaller than 50 pA at depletion voltage
- active volume of the detector
- dead layer and its uniformity

The full description of the characterization procedure and the corresponding results can be found in [56].

4.3 ^{241} Am scanning setup

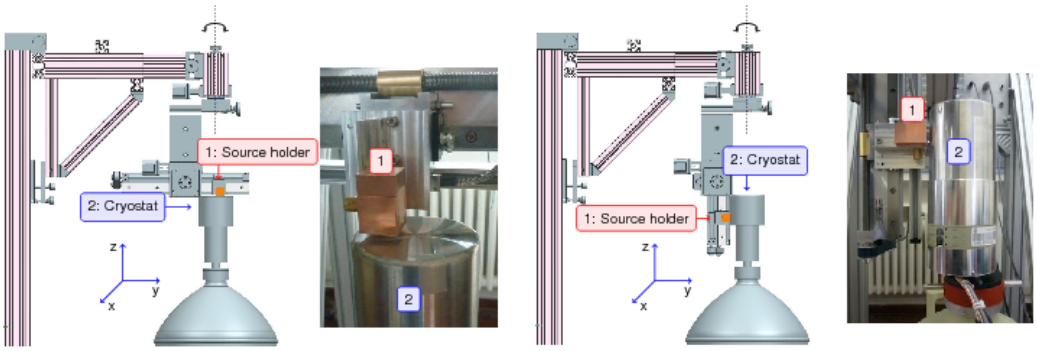

Fig. 4.5 Automated scanning table: Left: position of the source for a top scan. Right: position of the source for a lateral scan. Figures taken from [16].

For a better understanding of the spatial detector performance and dependence and surface effects in the BEGe detectors three automated scanning tables were produced. Each of them hosts a 5 MBq ^{241}Am source[1] in a copper box. The boxes have a 1 mm hole, serving as a collimator. Since the prominent γ-line of the ^{241}Am source has an energy of 59.5 keV and for this energy region the prime interaction mechanism is the photo effect, most of the events have a SSE character and are located close to the surface.
The copper box is mounted on an arm which can be moved with a precision better than 1 mm.

[1] Reference date: March 1st, 2012

At the same time the arm itself can be rotated along the x-axis to allow measurements on the top and side of the detector. The whole system again can be rotated in 1° steps around the z-axis. This makes it possible to illuminate each point on the top and lateral surface of the detector with an accuracy of 1 mm, like shown in fig. 4.5.

4.4 ^{241} Am scanning measurements

In this section a summery will be given of the circular top and lateral scans of the second batch of detectors. This batch consist of 23 detectors which were produced out of 7 germanium ingots. Six of them have a conical shape, one with the cone facing the point contact. For reference, two detectors made out of depleted germanium were also scanned and included in the analysis.
I will not include the analysis of the first batch since this was already done in [59].
Two types of scans were performed for the top surface. First the so called linear scans with a fixed angle through the center of the detector. These were performed to measure the diameter of the active volume and the exact position of the center. With that information the second type of scans were performed, the so called circular scans. In this case the radius was fixed to different values (mostly from 0-30 mm in 3 mm steps) and the source was rotated around the z-axis in steps of 95° for the most inner ring to 9° for the most outer ring. With these measurements the whole top surfaces of the detectors were scanned.
The scans of the lateral surfaces were performed in a similar way. First a linear scan in 0.5 mm steps from top to bottom was used to measure the placement and size of the crystal inside the cryostat. Afterwards the source was rotated around the z-axis in different heights in 5° steps. The results of the linear scans for one detector are shown in Fig. 4.6.
Tables 4.1 and 4.2 give a summary of the performed scans, for the analysis of each detector one top and lateral scan with the best data quality and the biggest spatial coverage was selected.
Each position in the scans was illuminated 120-300 s with a collimated 5 MBq ^{241}Am source. This leads to 1200-3000 counts in the ROI ($\pm$5 sigma) of the 59.5 keV peak as shown in fig. 4.7. These events were then selected to extract the key features like: peak position, resolution, rise time and the A/E pulse shape analysis parameter. The results are shown and discussed in the next section 4.5.

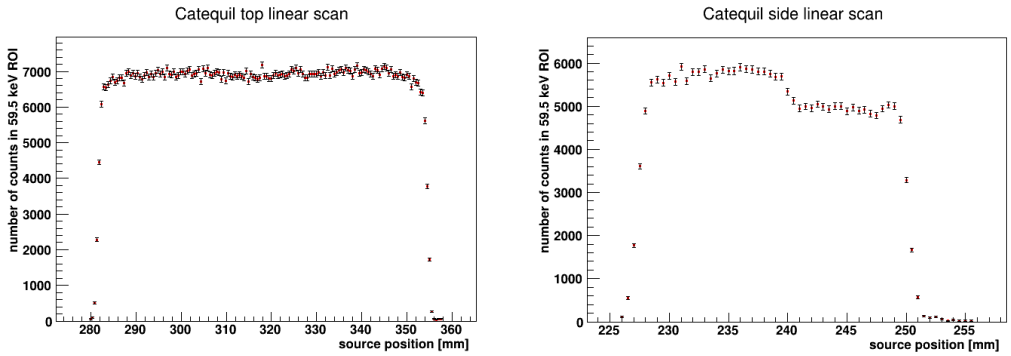

Fig. 4.6 Linear scans of the Catequil detector: Left: top scan, showing the number of counts in the 59.5 keV ROI Right: lateral scan, showing the number of counts in the 59.5 keV ROI, the decrease of the counts in the lower part are due to the structure of the holder

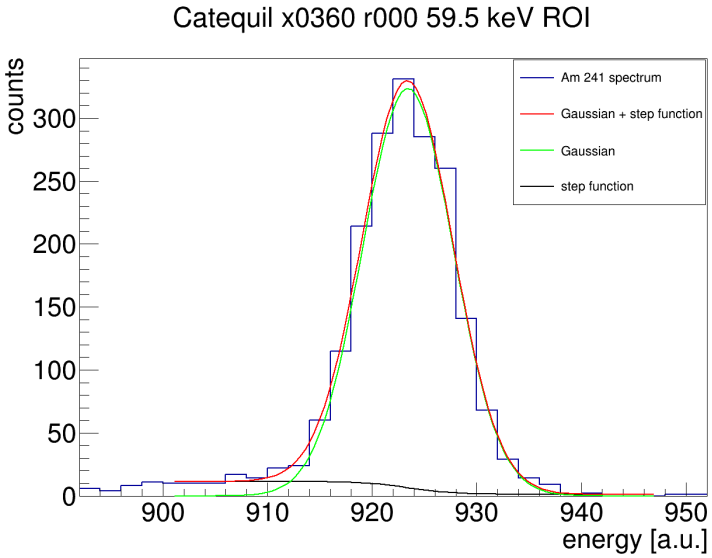

Fig. 4.7 In blue the 59.5 keV peak in the ^{241}Am spectrum, in black the step function representing the background, in green the Gaussian fit and in red the superposition of both: $f(x) = \frac{P_0}{P_1 \cdot \sqrt{2 \cdot \pi}} \cdot \exp(-\frac{(x-P_2)^2}{2_1^2}) + P_3 + \frac{P_4}{\exp(\frac{x-P_2}{P_1 \cdot 2})+1}$, to extract the peak position and resolution.

Table 4.1 Top scan summary. The detectors are sorted by the crystals and the slice type they were made of, where AA is the slice from the seed side and DD the one from the tail. The table also states the total number of points measured and the amount of rings with the minimum and maximum radius in the scan. The zero radius refers to a measurement point at the center position.

crystal	slice	name	number of points	number of rings	min. radius in mm	max. radius in mm
2461	AA	Chaos	217	5	0	25
2461	BB	Chiyou	221	11	0	30
2461	CC	Cassiopeia	221	11	0	30
2476	BB	Enkidu	168	11	0	24
2476	CC	Briseis	217	5	0	30
2479	BB	Babel	217	5	0	30
2479	CC	Bastet	217	4	0	33.5
2491	AA	Buri	217	4	0.5	20
2491	BB	Calypso	221	11	0	30
2491	CC	Bhima	217	4	0.5	21.5
2491	DD	Caesar	226	5	0	30
2500	AA	Cheops	85	5	0	28
2500	BB	Chronos	221	11	0	30
2500	CC	Bellerophons	217	4	0	26
2500	DD	Brahma	217	5	0	35.2
2502	AA	Bes	221	11	0	30
2502	BB	Bacchus	217	3	2	12
2502	CC	Centaur	221	11	0	30
2502	DD	Diana	148	11	0	27
40189	AA	Brian	217	5	0	20
40189	BB	Cleopatra	221	11	0	30
40189	CC	Catequil	221	11	0	30
40189	DD	Durius	168	11	0	30
depl.Ge	BB	Ge9	217	5	0	35
depl.Ge	DD	Dd	183	5	0	30

Table 4.2 Lateral scan summary. The detectors are sorted the same way as in table 4.1. For the detectors with only one ring measured only the minimum height is given in the table.

crystal	slice	name	number of points	number of rings	min. distance top surface in mm	max. distance top surface in mm
2461	AA	Chaos	144	2	6	26
2461	BB	Chiyou	358	10	4	22
2461	CC	Cassiopeia	379	11	1	21
2476	BB	Enkidu	180	5	4	16
2476	CC	Briseis	72	1	6	
2479	CC	Bastet	144	2	5	25
2491	AA	Buri	72	1	9	
2491	BB	Calypso	358	10	3	21
2491	CC	Bhima	72	1	3	
2491	DD	Caesar	72	1	7	
2500	AA	Cheops	67	1	6	
2500	BB	Chronos	379	11	1	21
2500	CC	Bellerophons	144	2	5	25
2500	DD	Brahma	73	1	15	
2502	AA	Bes	321	10	0	27
2502	BB	Bacchus	72	1	8	
2502	CC	Centaur	379	11	2	22
2502	DD	Diana	276	8	3	24
40189	BB	Cleopatra	287	8	0	21
40189	CC	Catequil	357	10	4	22
40189	DD	Durius	180	5	2	14
depl.Ge	BB	Ge9	72	1	2	
depl.Ge	DD	Dd	108	3	1	25

4.5 ^{241} Am scanning results

One of the most important characteristics to ensure a good detector performance is the homogeneity of the pulse height and resolution for the whole active volume of a detector. The circular top and lateral scans show that all detectors except 2502DD ("Diana") fulfill this requirement by having a stable peak position for 59.5 keV line of ^{241}Am, with a standard deviation smaller than 0.035%. An example is given in fig. 4.8. The peak position and resolution were reconstructed with a Gaussian fit with a step function as shown in fig. 4.7. The Diana detector displays an extreme spatial peak position dependence especially in the lateral scans where it varies by more than 10% as seen in fig. 4.9. This detector shows an overall reduced performance since the crystal is changing its p-type doping to n-type near the top surface. This also leads to a degraded charge collection efficiency and partially inactive volumes near the top surface as illustrated in fig. 4.10.
All enriched detectors have an average FWHM (full width at half maximum) less than 1 keV at the 59.5 keV line (see fig. 4.11). The theoretically achievable resolution is given by:

$$FWHM = 2.35 \cdot \sqrt{\frac{F \cdot w}{E}}$$

and varies between 235 and 355 eV for the energy E=59.5 keV depending on the used Fano factor F. This factor varies between 0.058 [60] and 0.13 [61] in the corresponding literature. $w = 2.96$ eV is the mean energy needed to create an electron-hole pair.
The two depleted BEGes show a slightly better FWHM resolution of $\sim$0.5 keV than the enriched ones which is due to the better signal to noise ratio. It is not clear why the noise was slightly smaller in these measurements. One possible explanation is the usage of preamplifiers from a different batch for the depleted detectors since they were produced earlier. In the standard resolution measurement with ^{60}Co and the corresponding 1.332 MeV line the enriched detectors show the same performance as the depleted ones. In this energy region the signal to noise ratio is much better and the noise does not contribute that much anymore to the FWHM.

4.5.1 Rise and drift time

The measurements in HADES were recorded with the Struck SIS3301 FADC in calibration mode to reduce the amount of data since the capacity was limited. This means that the 40 or 160 µs sampled traces were recorded with 100 MHz but 4 samples were summed into one. Only a short part of the trace was sampled with the full 100 MHz, namely 3 µs before and 2 µs after the trigger. This is sufficient for the rise time extraction since the drift time for

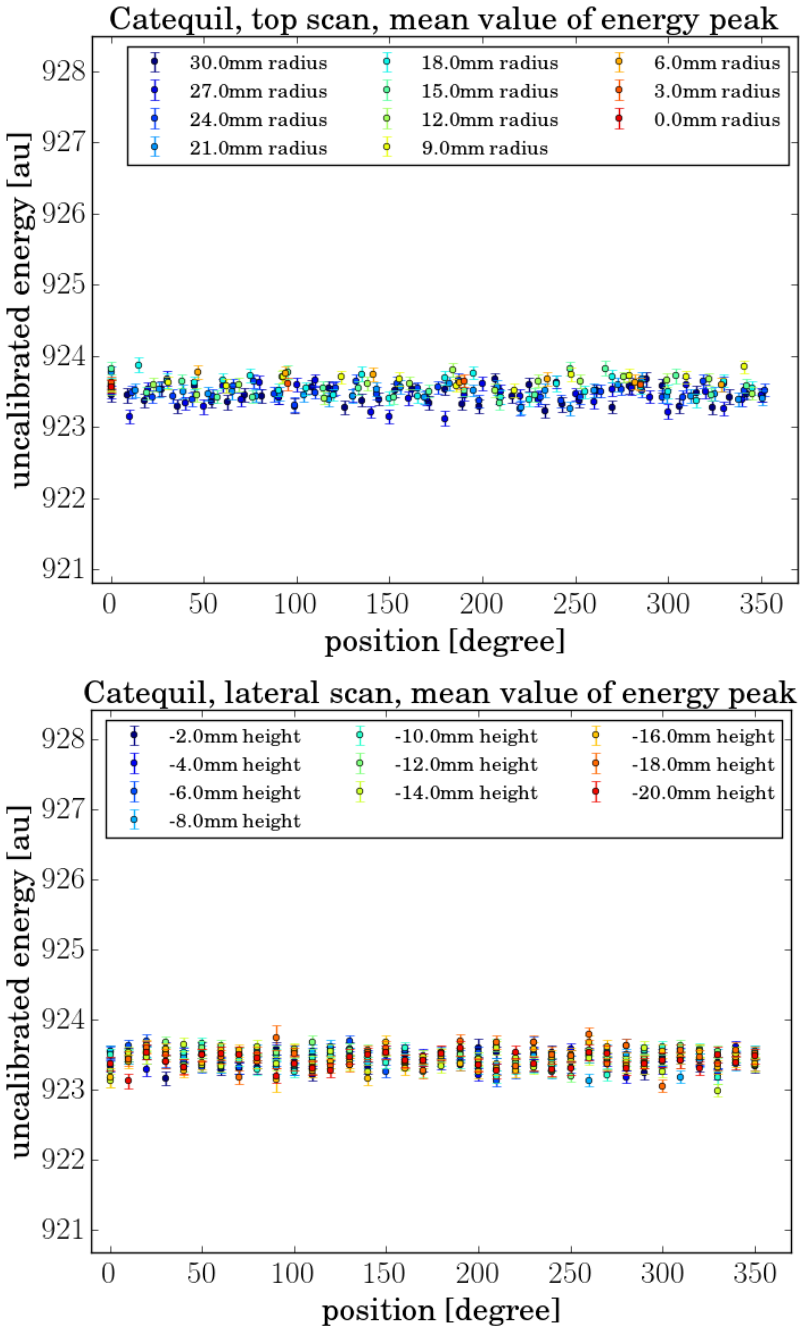

Fig. 4.8 Circular scans of the Catequil detector showing the peak position of the the 59.5 keV line. Top: top scan, Bottom: lateral scan

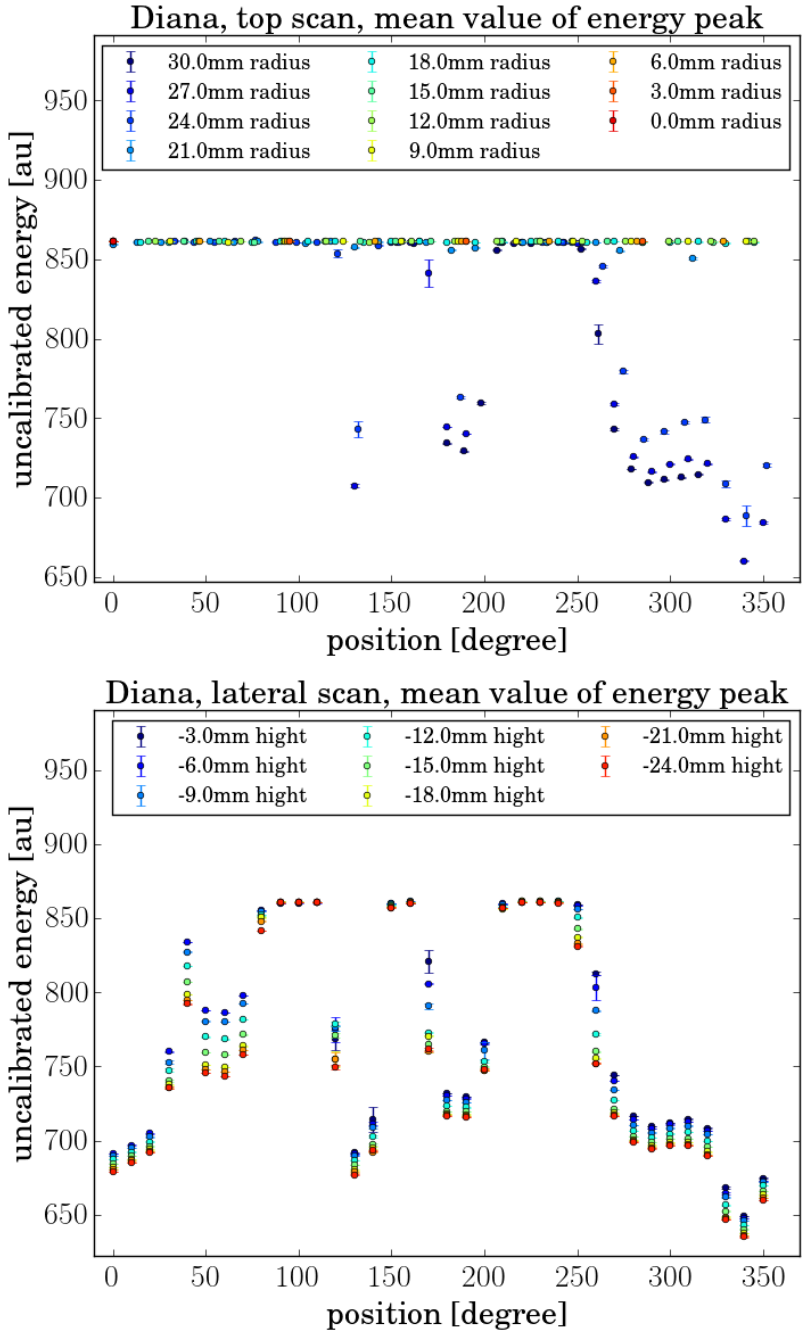

Fig. 4.9 Circular scans of the Diana detector showing the peak position of the the 59.5 keV line. Top: top scan, Bottom: lateral scan

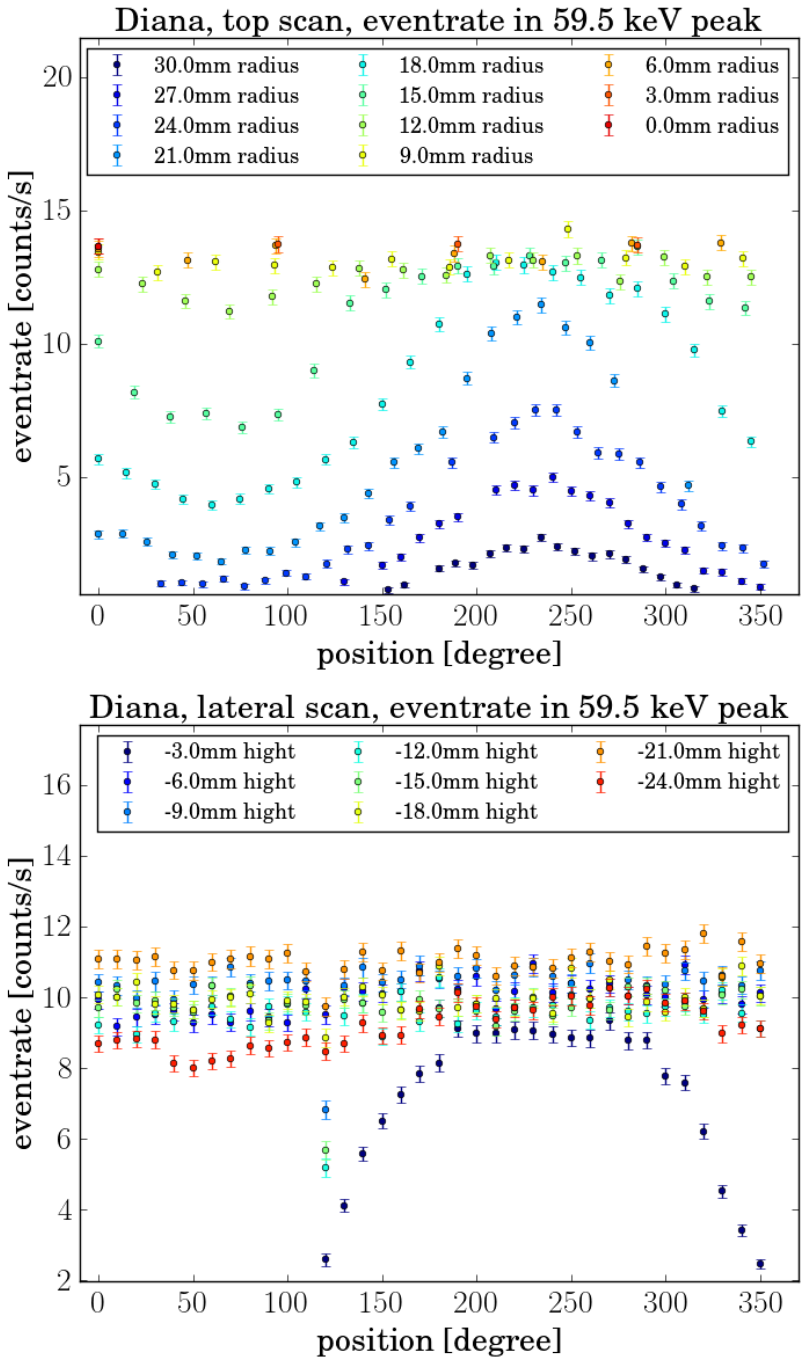

Fig. 4.10 Circular scans of the Diana detector showing the event rate in the 59.5 keV ROI, Top: top scan, Bottom: lateral scan

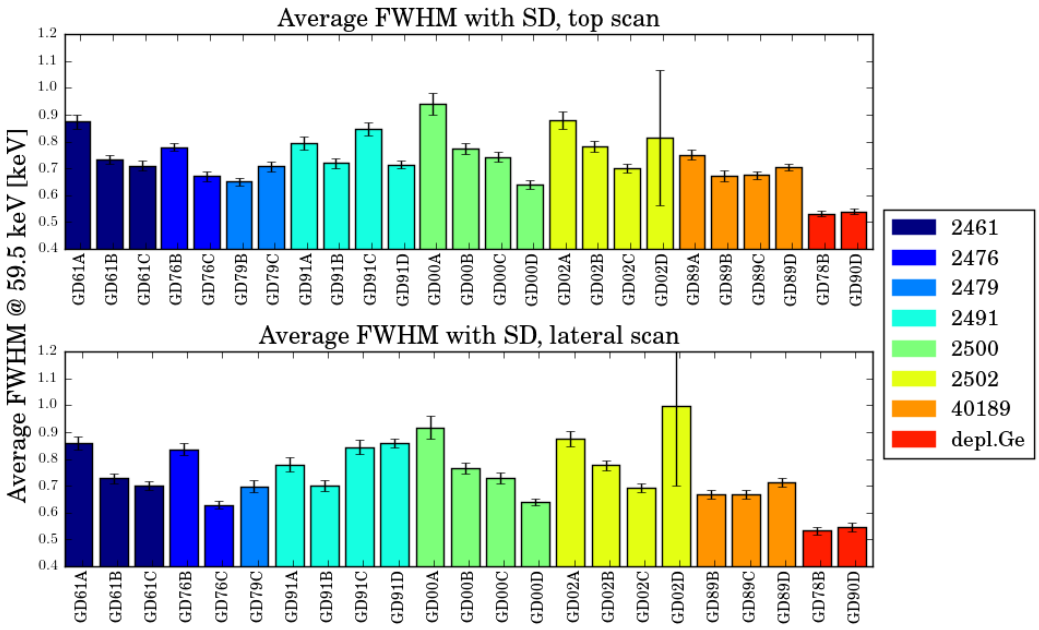

Fig. 4.11 Average FWHM @ 59.5 keV for all measured points with the standard deviation drawn as error bars. Detectors made from the same ingot are marked with the same color and are sorted by their slice type.

normal pulses in the BEGe detectors normally does not exceed 1 µs. Before the rise time extraction the pulses were shaped with a 50 ns moving average window and interpolated with ten intermediate steps. (see fig. 4.12). This reduces the probability of misidentifying noise wiggles as the start of a pulse. For each event in the 59.5 keV ROI the time, one pulse needs to develop from 1 to 90 % of the maximum amplitude was histogrammed and fitted with a Gaussian. (see fig. 4.13). The right tail in the histogram is caused by slow pulses from the transition layer. The 1-90 % rise time was chosen since it reproduces the real drift time of the charges, quite well as described in section 5.3 The rise time increases with the radius since

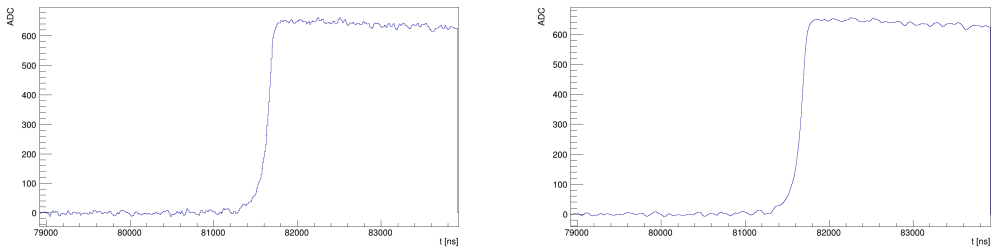

Fig. 4.12 Left: Raw 100 MHz sampled auxiliary waveform, Right: Waveform after shaping and interpolation

also the drift distance to the point contact increases for the holes. Considering that only the

holes are traveling through the strong weighting potential near the point contact only they contribute to the pulse. For all events except the ones near the point contact the contribution from the electrons can be neglected. The distribution of the rise time for the outer points is wider than for the center point which is due to the weak weighting potential for bigger radii. The charges are drifting here without a significant contribution to the total pulse height which makes it difficult to find the precise time when the pulse reaches the 1% level. Two examples for different radii are shown in fig. 4.13.

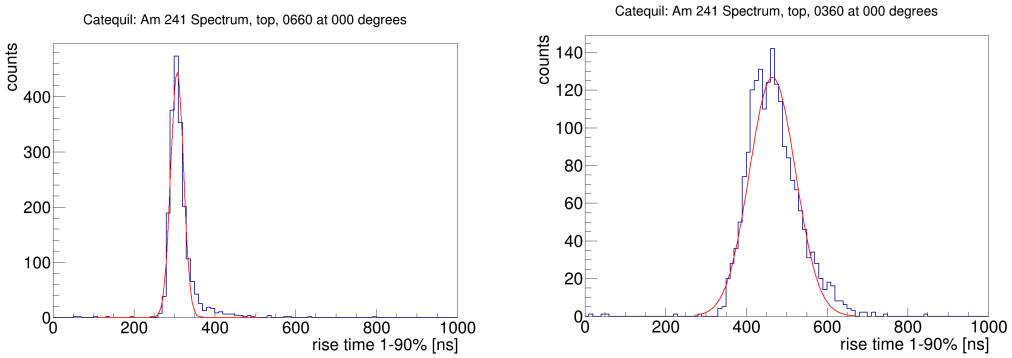

Fig. 4.13 1-90 % rise time distribution for the 59.5 keV ROI of Catequil. Left: Center point. Right: A point with 30 mm distance to the center.

The detectors can be divided into two groups. First, the majority of the detectors that show a clear oscillation for the rise time along the azimuth with a period of 90°. (see fig. 4.14). This behavior is expected due to the different mobilities along the crystal axes as described in section 3.2.1. The oscillation is only visible for bigger radii close to the detector edges in the top circular scans since only for them the drift path in the x-y-plane is long enough to produce a measurable difference. In the lateral scans the oscillation is visible for all heights since here the drift path is maximal in the x-y-plane.

As shown in fig. 4.14, the mean 1-90 % rise time does not change for the two outer rings in the top circular scan which are 5 mm apart from each other. Also in the lateral circular scan the mean rise time is the same for different heights although the drift path is different. This means that the 1-90% rise time does not represent the full drift time of the holes for the outer radii. In this region the weighting potential is nearly zero and thus only a small current is induced on the read out electrode by moving charges. Also the poor signal to noise ratio of the 59.5 keV signals makes it difficult to measure a small increase in the pulse height and to calculate the start of the signal properly. This high noise for the small signals is a trade-off the high dynamic range of the FADC. It was set to measure signals up to several MeV and so its own electronic noise is prominent in small signals.

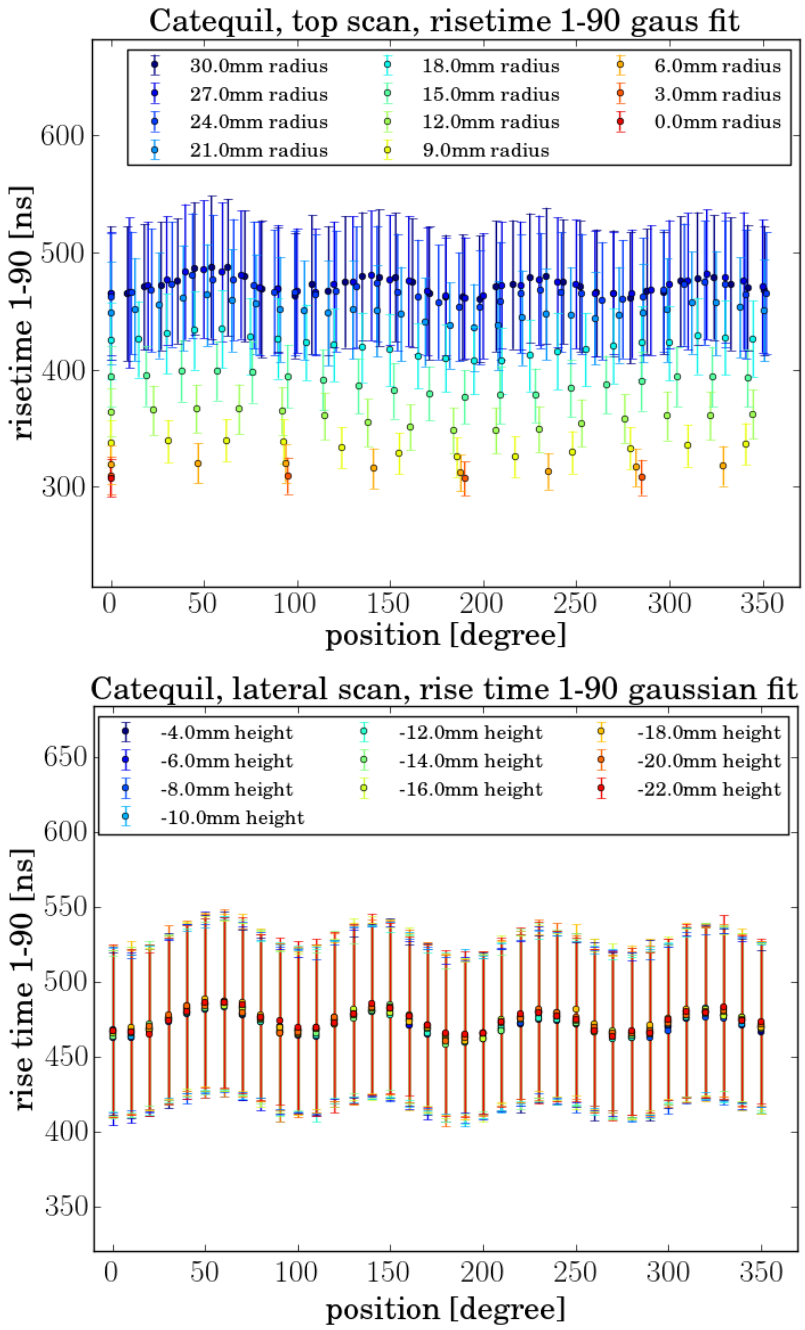

Fig. 4.14 Each point in the graph represents the mean of the Gaussian fitted to the rise time distribution in the 59.5 keV ROI with the σ as error bars. Top: Top circular scan. Different radii are plotted in different colors. The center point is plotted as r=0 mm and ϕ=0°. Bottom: Lateral circular scan. Each color represents a different z position in the scan with the top surface of the detector as z=0.

For radii up to 15 mm an oscillation period of 180° is observed. This is most likely due to a non perfect alignment of the scanning apparatus to the crystal center. In this case the drift distance in the x-y plane for holes varies also with a 180° period. The rise time difference of ∼30-35 ns between two rings for the inner part of the detector (r<21 mm) is similar for all rings. The oscillation amplitude within a ring can be up to 20 ns. This indicates a misalignment of approximately 1 mm from the center.
The second group of detectors does not show a clear oscillation pattern. The distribution seems to be disturbed like in fig. 4.15. In this case the variation cannot be explained by the misalignment of the scanning arm since the oscillation is also disturbed in the lateral scans where the distance from source to detector does not have a strong correlation to the rise time. For these scans only the azimuthal angle plays a role. This effect is most likely caused by a deformed weighting potential along the azimuth caused by inhomogeneous trapped charges on the passivation layer in the groove. The influence of such charges on the weighting potential and wave forms was simulated and is discussed in section 4.6.

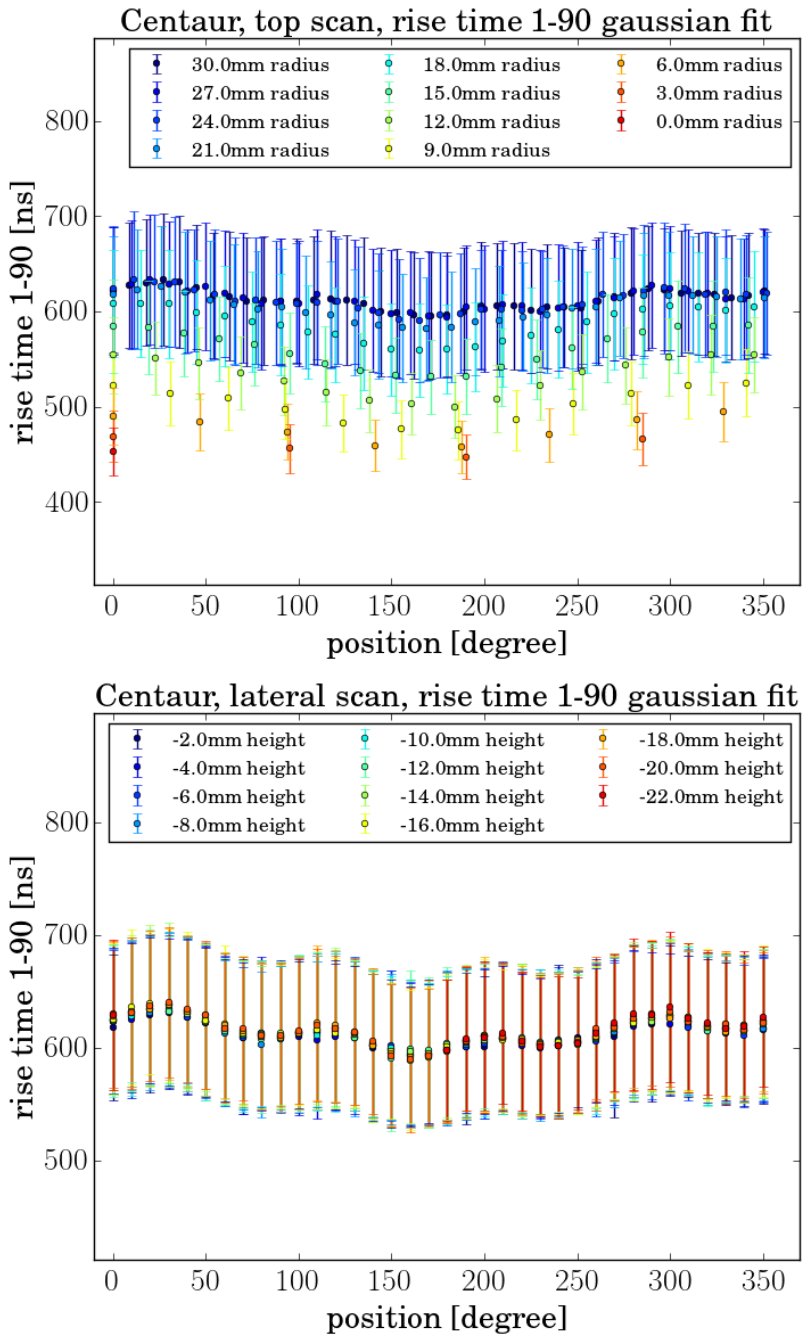

Fig. 4.15 Each point in the graph represents the mean of the Gaussian fitted to the rise time distribution in the 59.5 keV ROI with the sigma as error bars. Top: Centaur top circular scan. Different radii are plotted in different colors. The center point is plotted as r=0 mm and ϕ=0°. Bottom: Centaur lateral circular scan. Each color represents a different z position in the scan with the top surface of the detector as z=0.

4.5.2 A/E parameter

The A/E parameter provides an easy and powerful discrimination possibility between multi and single site events in a BEGe detector. The discrimination efficiency is strongly correlated to the A/E distribution for single site events at a given energy. The narrower the distribution, the better is the differentiation between these two event classes. While testing the first batch of detectors, it was found that most of the enriched detectors have a wider and non-Gaussian like distribution of the A/E parameter in contrast to most detectors made out of depleted material. The circular scans were used to check the detectors for a spatial dependence of the A/E parameter. For each scanning point the parameter was histogrammed like for the rise time and fitted with a Gaussian. Since the 59.5 keV ROI mostly consists out of SSE, the A/E parameter follows a normal distribution with a small tail to lower values composed of MSE and slow pulses from the transition layer as shown in fig. 4.16.

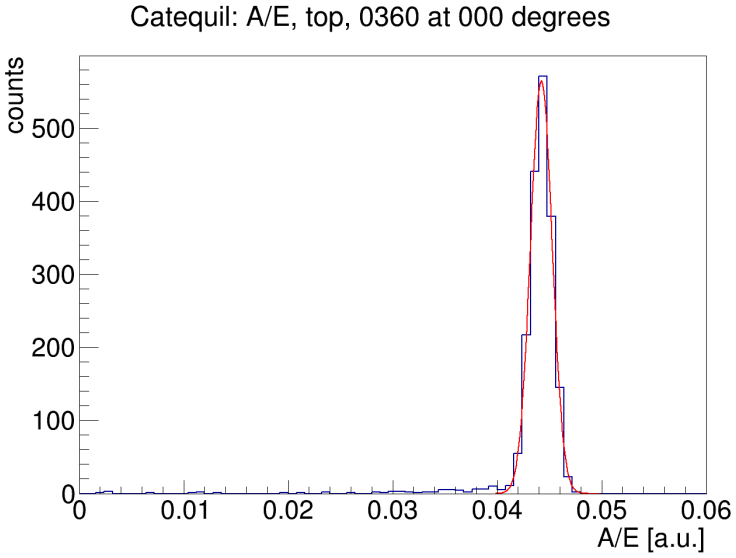

Fig. 4.16 Catequil: A/E @ 59.5 keV ROI at r=30 mm and 0° fitted with a Gaussian.

The enriched detectors can be classified in three groups concerning their A/E spatial dependence.

The first group which consists only of one detector, Caesar (GD91D), does not show a significant spatial dependence (A/E variation < 1 %) and thus behaves similar to the depleted detectors as seen in fig. 4.17.

This detector also has a Gaussian A/E distribution for the double escape peak (DEP) of ^{208}Tl like the depleted detectors. The DEP consist mostly of SSE because the energy is deposited in a small volume by the electron-positron pair after pair production. Fig. 4.18 shows the normalized DEP A/E distribution for Caesar and the depleted detector Ge9.

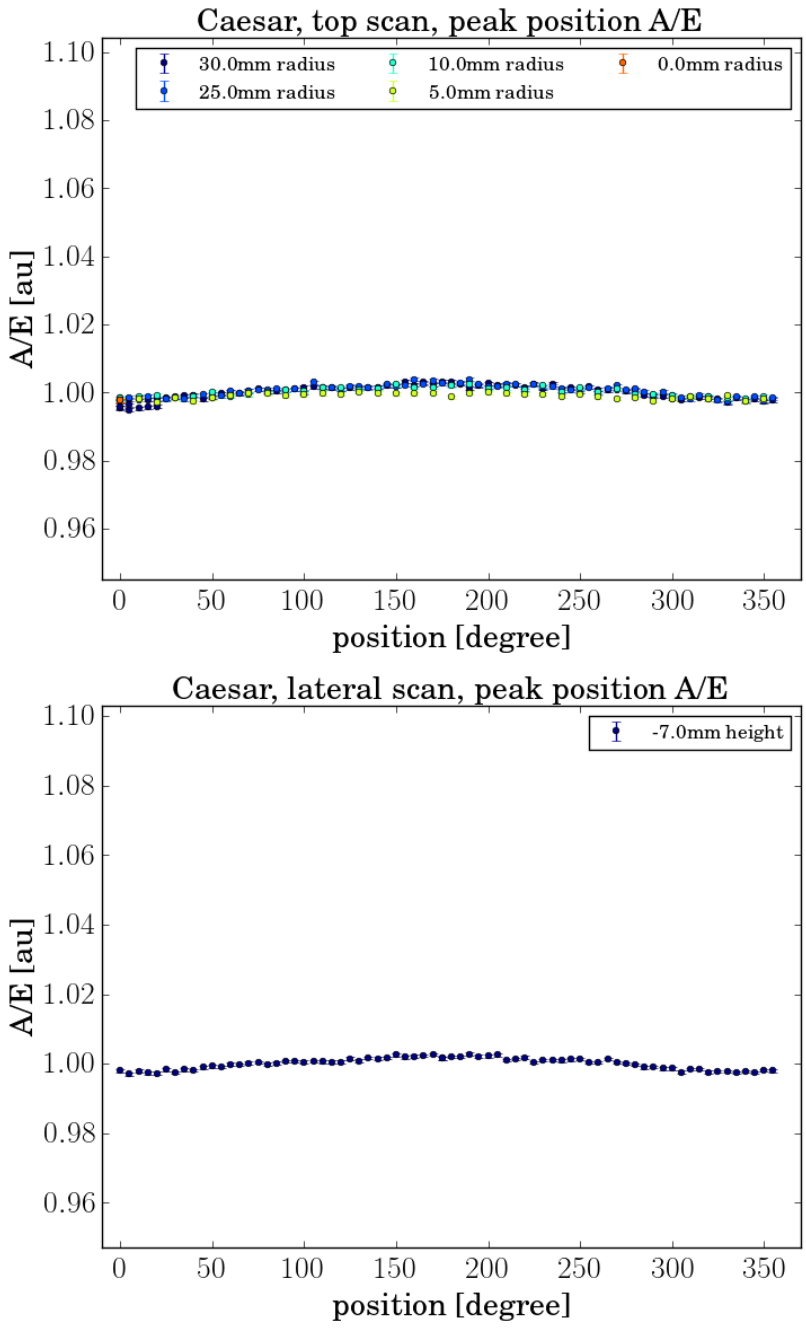

Fig. 4.17 Each point in the graph represents the mean of the Gaussian fitted to the A/E distribution in the 59.5 keV ROI. Top: Caesar top circular scan. Bottom: Caesar lateral circular scan.

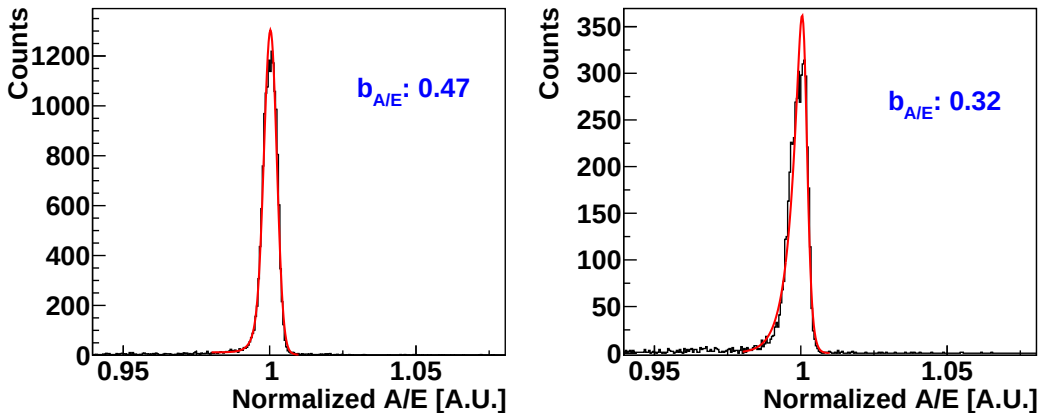

Fig. 4.18 The normalized A/E distribution of the ^{208}Tl DEP fitted with a Gaussian and an asymmetric tail. Taken from [62] Left: Caesar, Right: Ge9 made from depleted Ge.

The second group shows a degradation of A/E parameter towards the center of the detector and an oscillation for outer radii along the crystal axis as depicted in fig. 4.19. Both variations differ for each detector. The degradation can be up to 6 % off the mean value for all points but is usually smaller. The amplitude of the oscillation can be up to 3 % off and shows the same pattern as the one for the rise time along the crystal axis.

The decrease of the A/E parameter towards the center does not always correlate with the A/E resolution for the DEP since the probability for two gammas to escape the detector without energy deposition is higher in the detector edges and thus the majority of the DEP events is located at outer radii. Because of that and the procedure to fit an asymmetric tail to the A/E distribution to take the MSE into account, the A/E calibration with the DEP is not sensitive to this variation since these events are misinterpreted as MSE. For example the Bellerophons detector shows a strong radial A/E dependence with a difference of 2.6 % between the minimum A/E value for the center point and the maximum A/E for a point on the detector edge, but still has good A/E DEP resolution of 0.58 % [62].

To investigate the impact on the PSD performance the energy depositions for the ^{228}Th source which is used for the A/E DEP calibration were simulated for the Catequil detector with the MaGe framework [28]. The corresponding coordinates were used to calculate the amount of DEP events in rings of 3 mm width along the radius of the top surface corresponding to the circular top scan of the detector. Then the A/E distribution for all 59.5 keV ROI events, for all measurement points in one ring, were plotted and weighted with this values as shown in fig. 4.20. Since there is no scanning measurement for the outermost ring from 31.5 mm to the edge, the A/E value for the 30 mm measurement was used in the normalization which is stable for all rings starting from 21 mm radius. As seen in fig. 4.20. most events within

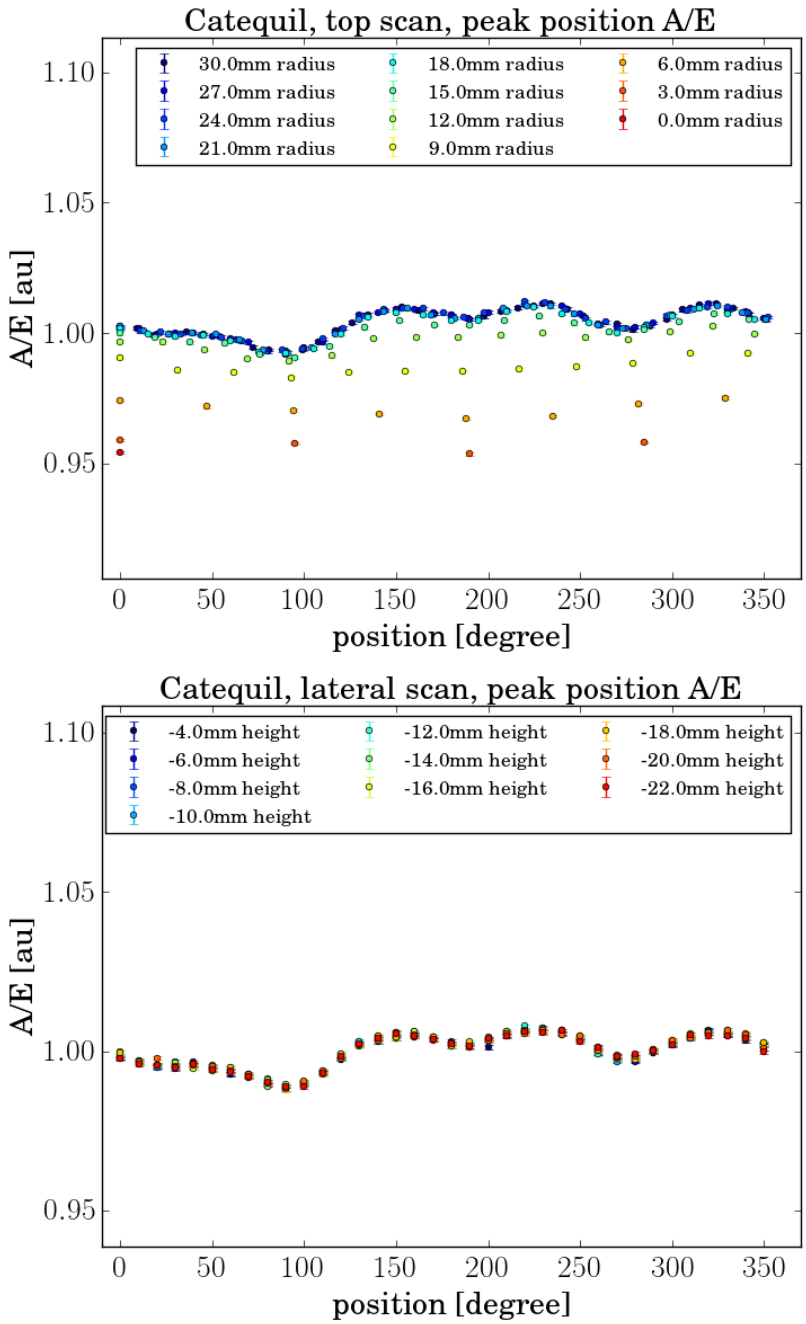

Fig. 4.19 Each point in the graph represents the mean of the Gaussian fitted to the A/E distribution in the 59.5 keV ROI. Top: Catequil top circular scan. Bottom: Catequil lateral circular scan.

a radius smaller than 7.5 mm would not survive the standard A/E cut used in the common GERDA analysis. This corresponds to an efficiency loss of $\sim 5\%$.

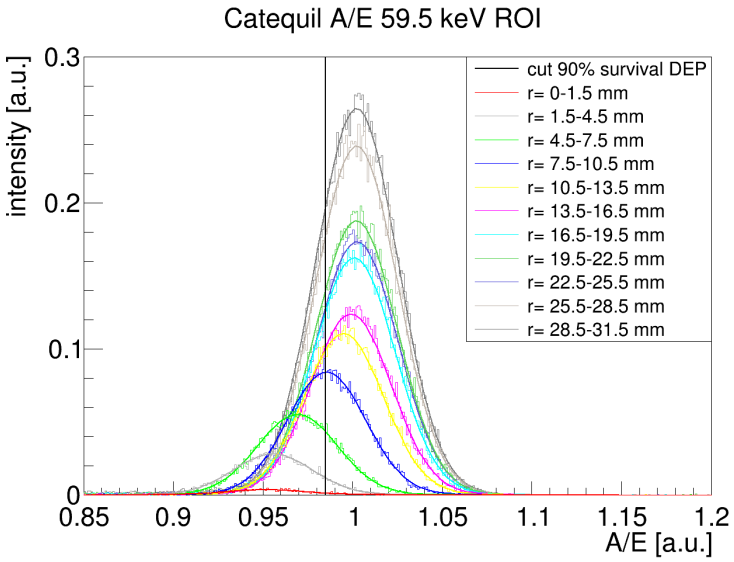

Fig. 4.20 For each ring with increasing radius the A/E distribution for the 59.5 keV ROI was plotted and fitted with a Gaussian and normalized to its geometrical abundance of the DEP spatial distribution from the MaGe simulation. The black line represents the cut value for the 90% DEP survival.

The last group shows an irregular A/E distribution along the detector surface as seen by the example of Centaur in fig. 4.21.

The feature of a decreasing A/E towards the center is also present in this group. These detectors tend to have a very broad or multi peak A/E distribution for the DEP events of ^{208}Tl as shown in Fig 4.22. The double peak structure for Centaur can be explained by the asymmetric A/E structure in the scans. The measurement points between $\sim 75°$-$200°$ have a bigger A/E value for the outer radii which leads to the observed double peaking of the A/E parameter in the DEP ROI. (see fig. 4.21).

As shown in fig. 4.23, the centroid of the A/E Gaussian distribution for the individual scanning points varies much stronger for the enriched detectors in comparison to the two depleted ones. The resolution for individual points in contrast is stable and comparable for both detector types as illustrated in fig. 4.24. The A/E resolution for low energies is dominated by the electronic noise because of the small signal to noise ratio and therefore is mostly worse for the ^{214}Am scans than for the DEP ROI.

The A/E DEP resolution can be linked to the spatial variation of the A/E mean for the circular scans as shown in fig. 4.26, especially for the lateral ones since the DEP events are mostly located in the edges of the detector. This part of the detector is well represented in the lateral scans even with just one vertical position measured since most of the detectors do not show an A/E dependence along the z-axis for events close to the mantle. Calypso does show such a

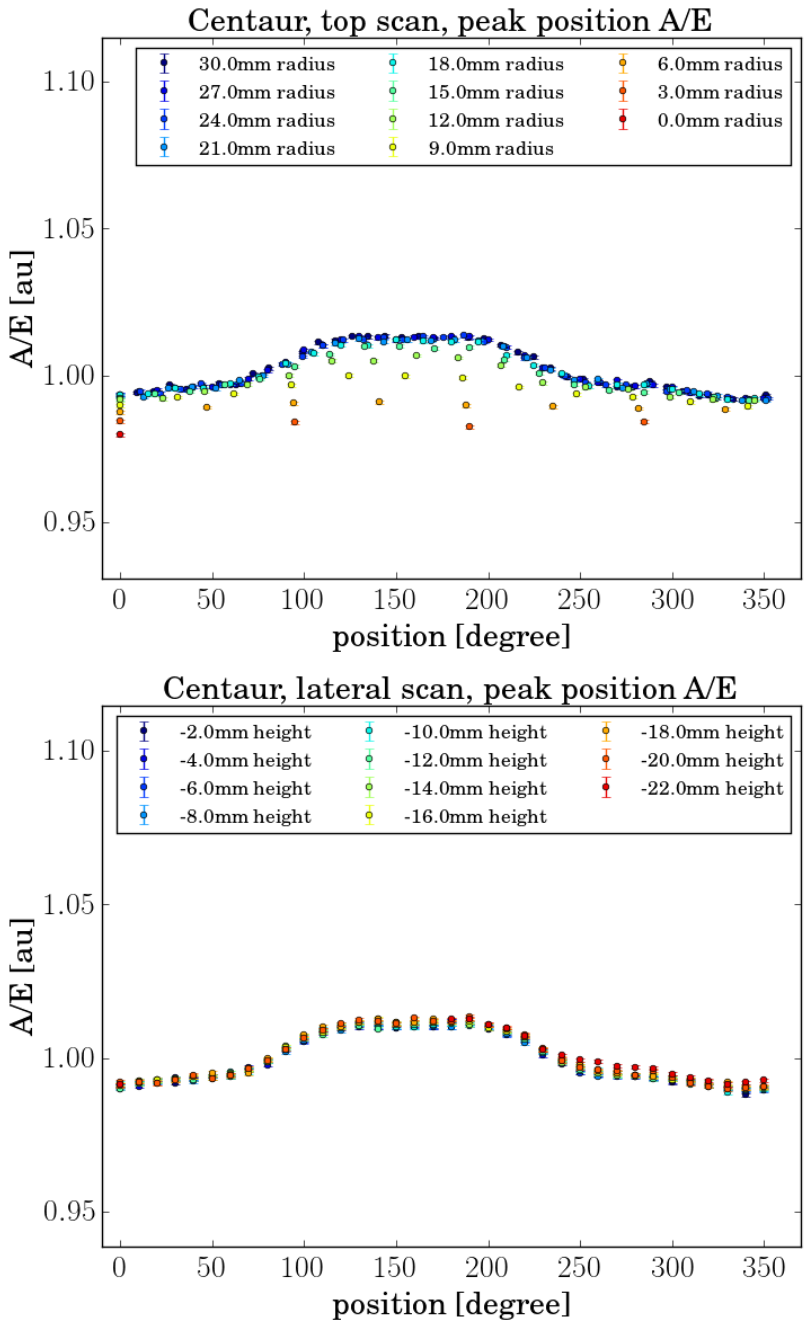

Fig. 4.21 Each point in the graph represents the mean of the Gaussian fitted to the A/E distribution in the 59.5 keV ROI. Top: Centaur top circular scan. Bottom: Centaur lateral circular scan.

dependence along the z-axis and therefore does not follow the overall trend. But as shown in fig. 4.27 the DEP A/E resolution does not always correlate with the maximum A/E difference for two scanning points as mentioned earlier. Briseis and Bellerophons are good examples

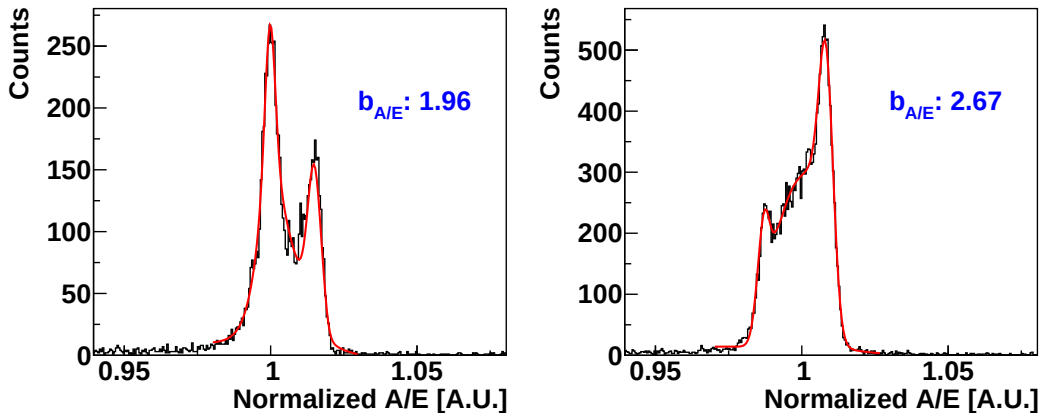

Fig. 4.22 The normalized ^{208}Tl DEP A/E distribution fitted with multiple Gaussians and an asymmetric tail. Taken from [62] Left: Centaur, Right: Bhima.

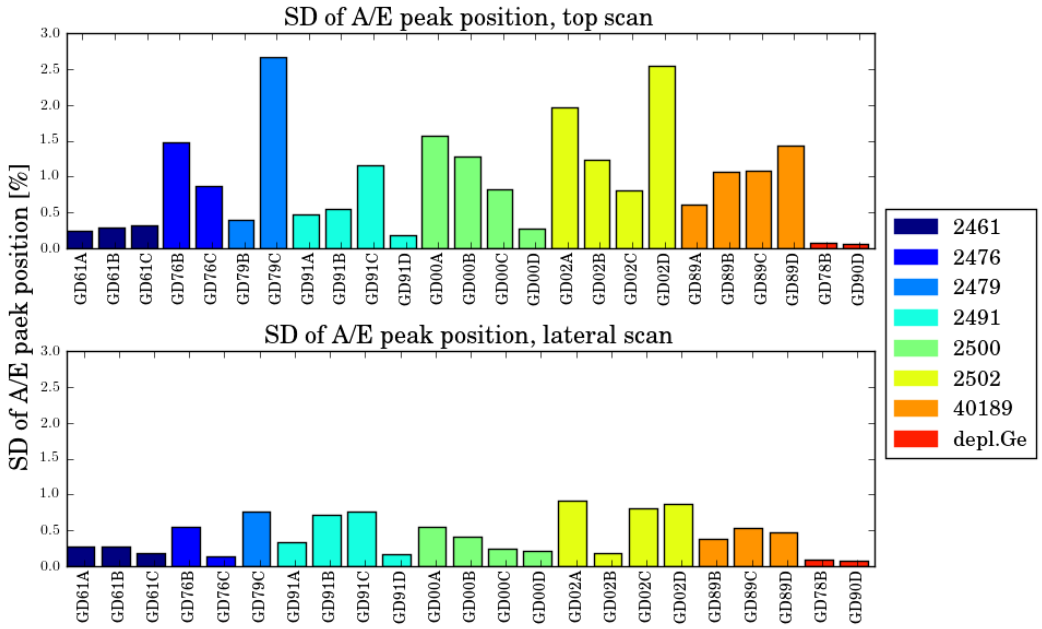

Fig. 4.23 Standard deviation of the centroid of the A/E distribution @ 59.5 keV ROI for all measured points.

for this effect. Both have a good DEP A/E resolution (0.40 and 0.56 %) but still show a degradation of the parameter towards the center. (see fig. 4.25) This can effect the efficiency of the standard pulse shape discrimination for background suppression by misidentifying SSE from the center as MSE.

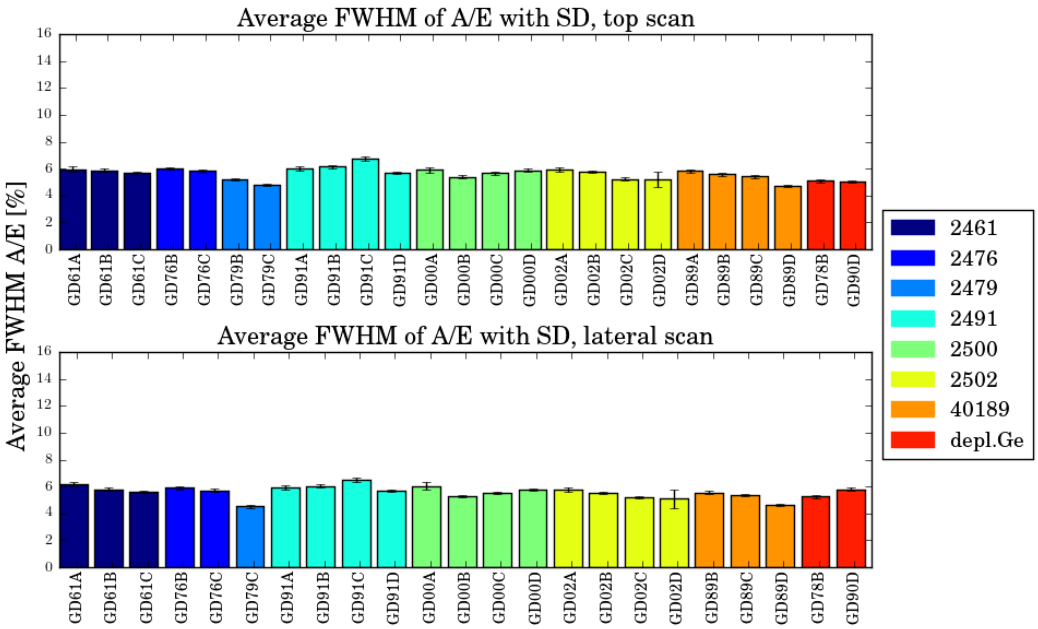

Fig. 4.24 Average FWHM of the A/E distribution @ 59.5 keV ROI for all measured points with the standard deviation drawn as error bars.

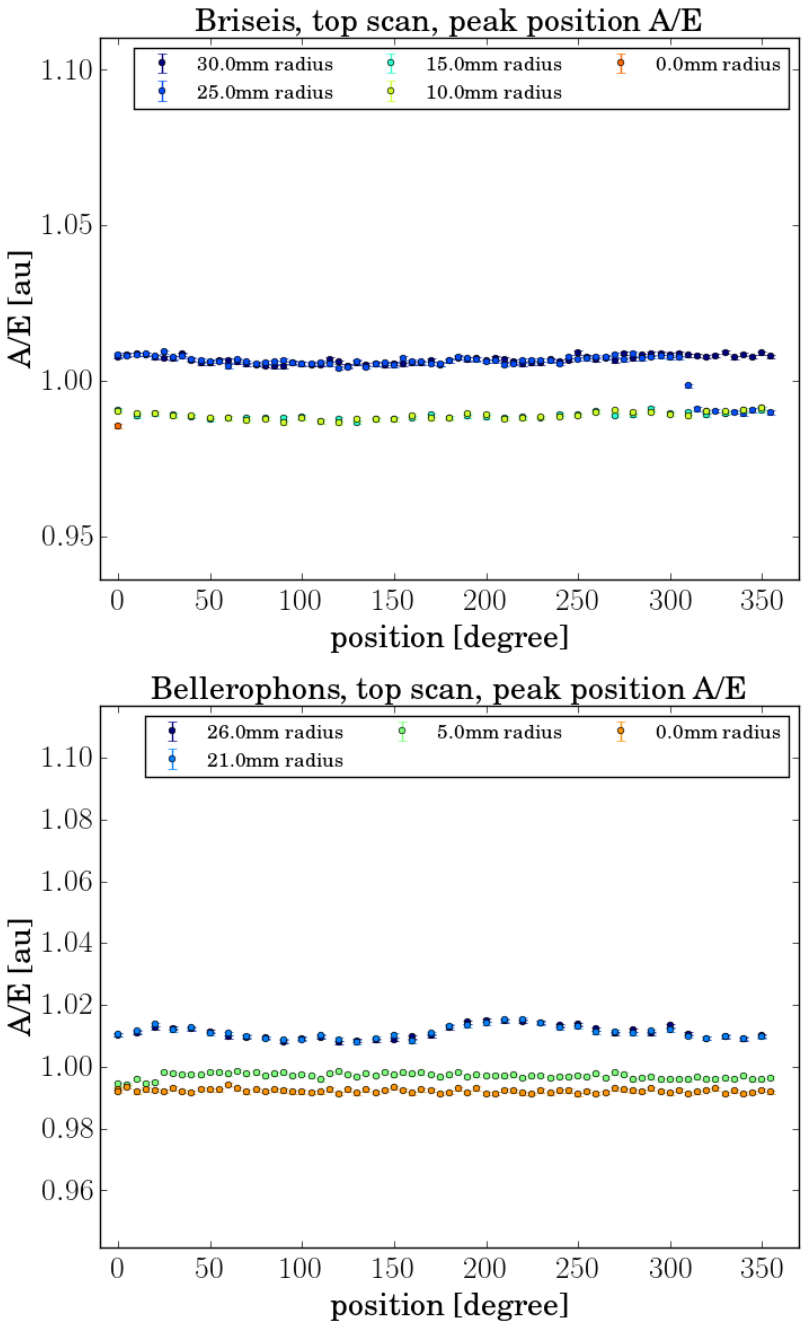

Fig. 4.25 Each point in the graph represents the mean of the Gaussian fitted to the A/E distribution in the 59.5 keV ROI. Top: Briseis top circular scan. Bottom: Bellerophons top circular scan.

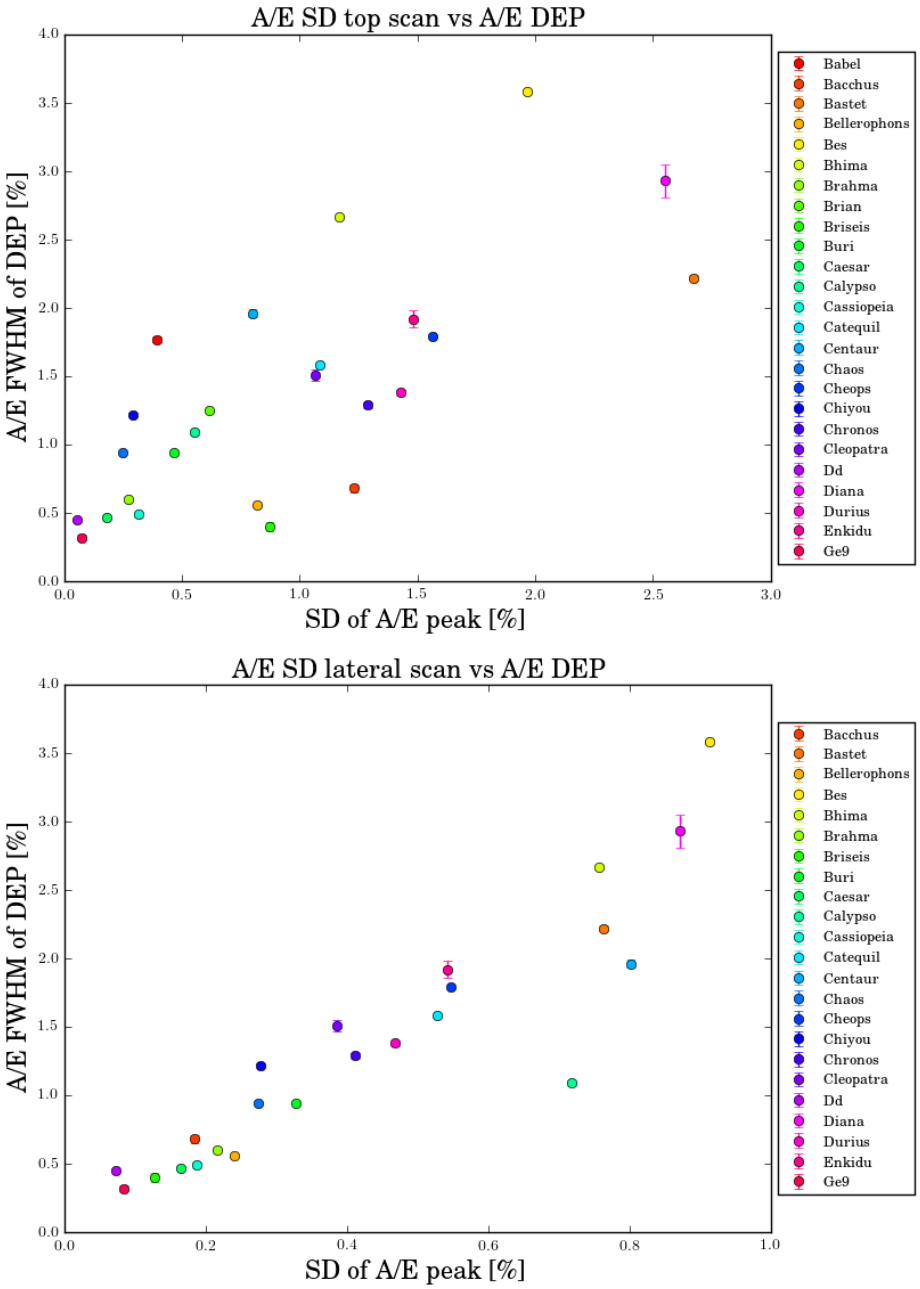

Fig. 4.26 FWHM of the A/E distribution for the DEP events is plotted vs the standard deviation of the centroid of the A/E distribution in the 59.5 keV ROI for individual points in the circular scans. Top: Top scan, Bottom: Lateral scan. The FWHM values of the A/E DEP distributions were taken from [62].

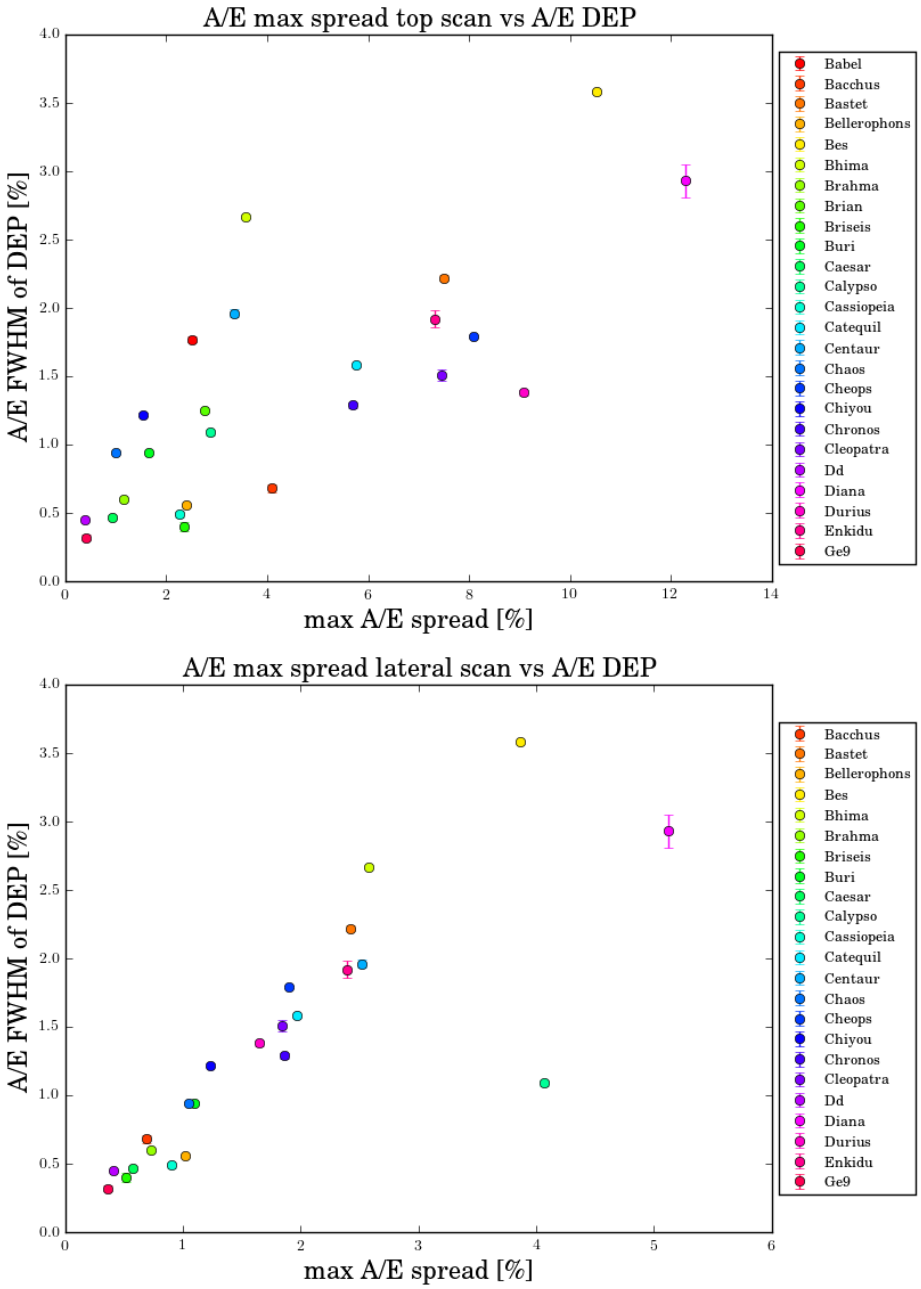

Fig. 4.27 FWHM of the A/E distribution for the DEP events is plotted vs the maximum difference of the centroids of the A/E distribution in the 59.5 keV ROI for two individual points in the circular scans. Top: Top scan, Bottom: Lateral scan. The FWHM values of the A/E distributions were taken from [62].

4.6 Comparison with the simulations

For a better understanding of the A/E anomaly and to probe the hypothesis that trapped charges inside the groove are responsible for it, detector pulses were simulated with the `mjd_siggen` package as described in chapter 3. Before that, the scanning setup was simulated with MaGe to calculate the energy deposition positions for the 59.5 keV γ-ray of the ^{241}Am source as illustrated in Fig 4.28. For each simulated event all interaction points of the gamma inside a 1 mm sphere were summed up and the weighted mean was used as the interaction position for the pulse shape simulation. The simulated pulses were then analyzed with GELATIO. The same parameters as for the measured pulses were used for the calculation of rise time and the A/E parameter. Before the extraction of the relevant parameters, white

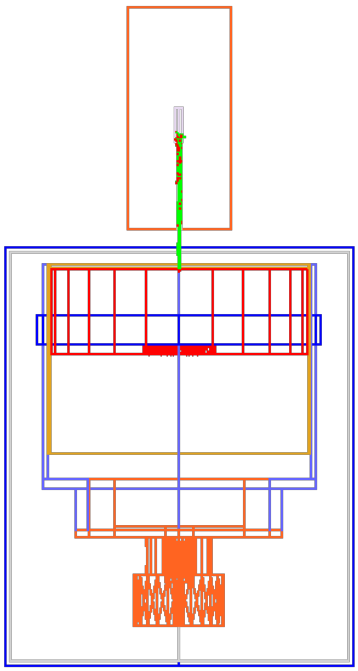

Fig. 4.28 Detector and collimator geometry used in MaGe. The sensitive volume of the crystal is drawn in red, above it the source is drawn in cyan inside the copper housing. The photon paths are drawn in green and the interaction points with matter in red.

noise was added to the pulses (see fig. 4.29).
Besides the geometry, the important parameters for the pulse simulations are the net impurity concentration and the impurity gradient since they are contributing to the effective electrical field and the shape of the weighting potential. For the simulation of the Catequil detector a net

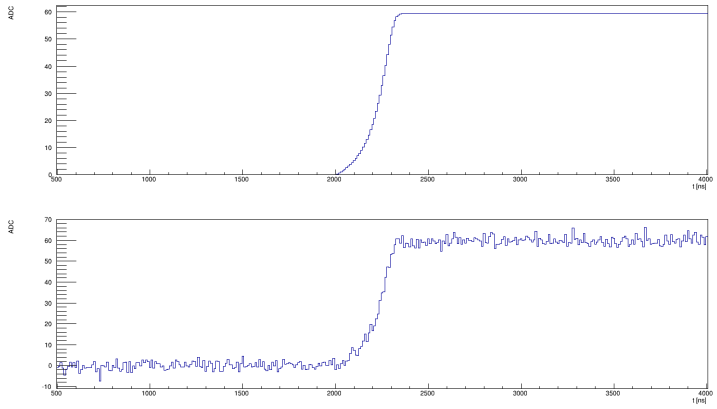

Fig. 4.29 Top: Simulated pulse of the Catequil detector. Bottom: Simulated pulse with white noise.

impurity concentration of $2.7 \cdot 10^{10} \frac{e}{cm^3}$ at the point contact side was used. A linear gradient of $0.4 \cdot 10^{10} \frac{e}{cm^4}$ was chosen since the detector is a C slice from the middle of the ingot. The net impurity concentration at the top and bottom of the crystal slice was measured by the manufacturer. To test the influence of trapped charges inside the groove on the passivation layer a charge density of $35 \cdot 10^{10} \frac{e}{cm^2}$ was placed on it in the simulation.
As seen in fig. 4.30 the absolute rise time for events close to the corners is underestimated in the simulations with and without additional charges. The error on the mobility for low electric fields used in the simulation is big and thus could explain the discrepancy between measurement and simulation. The value for the center position is in a good agreement and the measured oscillation pattern along the crystal axis is well reproduced in the simulation. The simulation without the additional charges shows only a small position dependence for the A/E distribution and thus looks similar to the ones of the depleted BEGes. By adding charges to the groove the measured oscillation and the decrease for smaller radii is reproduced in the simulation as illustrated in fig. 4.31. The measured oscillation is not completely symmetric which indicates that the distribution of the charges in the groove is not homogeneous.
Fig. 4.32 shows simulated hole drift paths for different starting positions on the top surface of the detector. The two outer starting points have the same radius but are shifted by 45^0 and thus the holes move along different crystal axes. Because of the faster drift along the <100> plane the hole hits the point contact closer to the center. It seems that the additional charges deform the electrical field in a way that the funneling effect is not working properly. The drift paths for interactions near the mantle end closer to the groove, which leads to a higher A/E value. This distortion also leads to a bigger spread between the drift paths along different crystal axes and reproduces the measured A/E oscillation. Table 4.3 contains the absolute A/E values for the different starting points and field configurations.

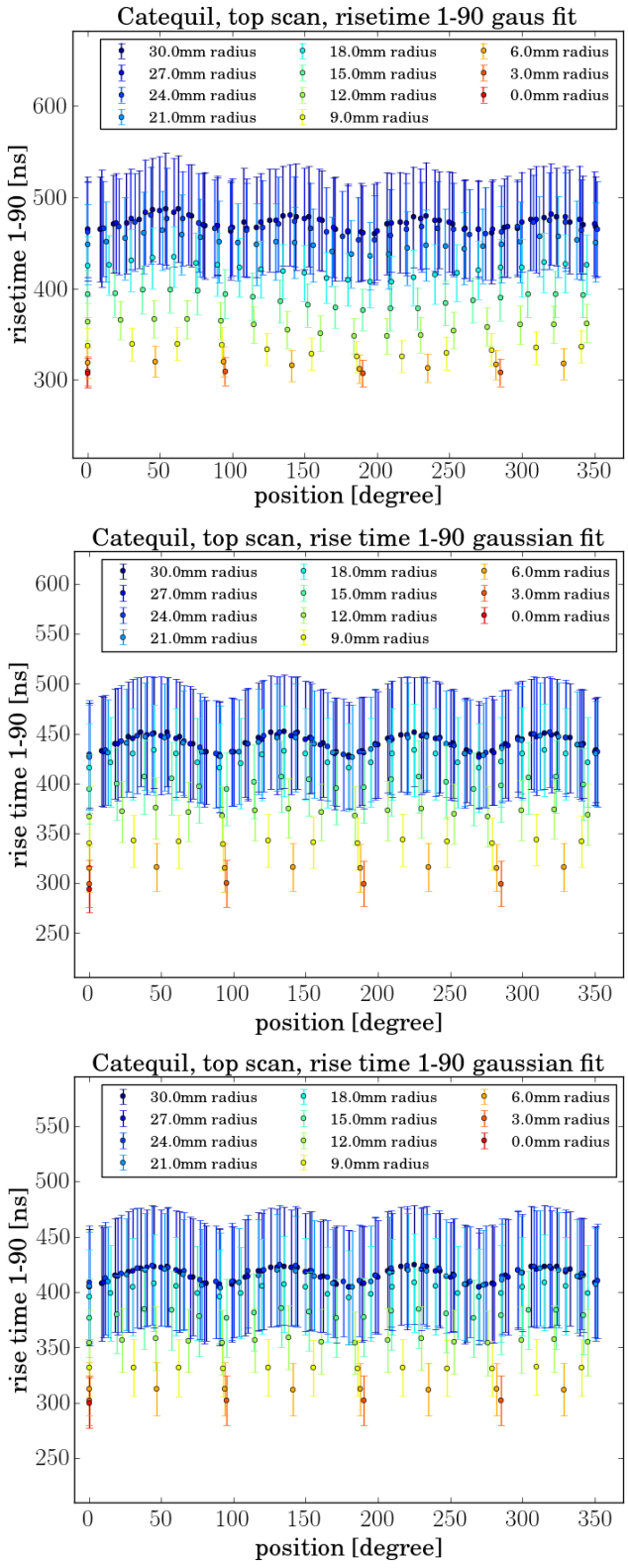

Fig. 4.30 Each point in the graph represents the mean of the Gaussian fitted to the rise time distribution in the 59.5 keV ROI with one sigma as error bars. Different radii are plotted in different colors. The center point is plotted as r=0 mm and ϕ =0^0. Top: Measured top circular scan. Middle: Simulated top circular scan. Bottom: Simulation with additional charges in the groove.

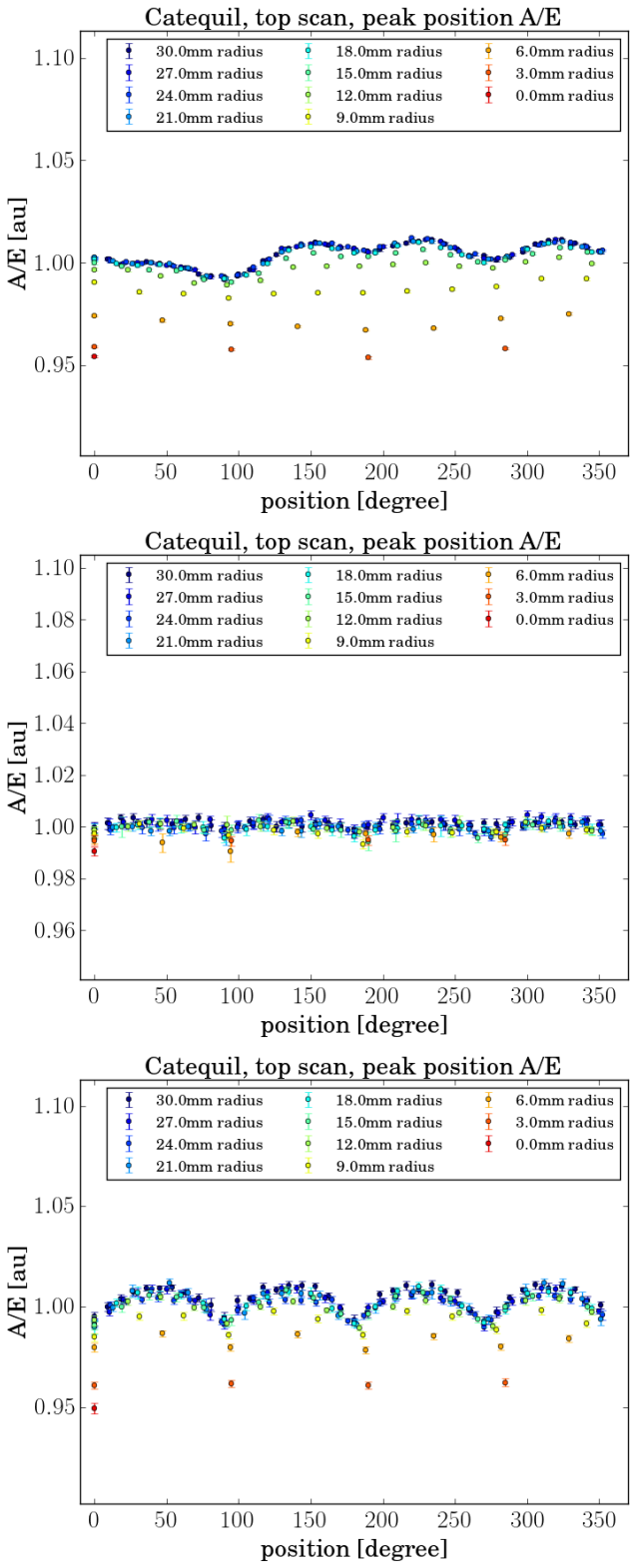

Fig. 4.31 Each point in the graph represents the mean of the Gaussian fitted to the A/E distribution in the 59.5 keV ROI. Different radii are plotted in different colors. The center point is plotted as r=0 mm and ϕ =0^0. Top: Measured top circular scan. Middle: Simulated top circular scan. Bottom: Simulation with additional charges in the groove.

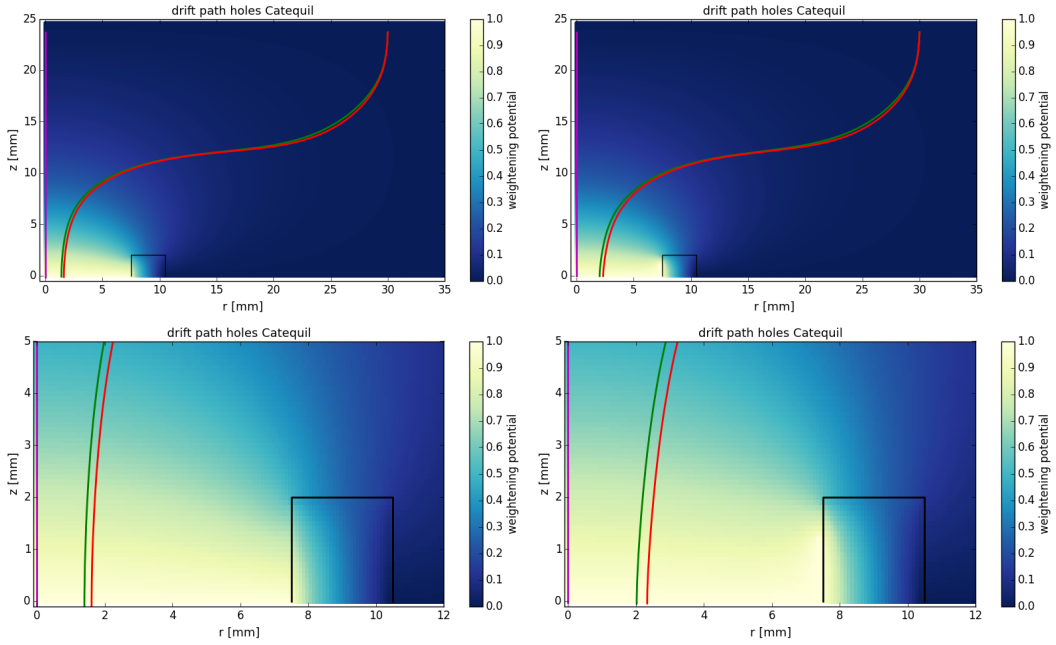

Fig. 4.32 Simulated hole drift paths for the Catequil detector. Left: Normal weighting potential. Right: Distorted weighting potential by additional charges in the groove. Violet line: Hole is starting from the center position. Green line: Hole is starting from r=30 cm and ϕ =0^0 in the <100> plane. Red line: Hole is starting from r=30 cm and ϕ =45^0 in the <110> plane. Bottom: Explosion plots of the centered region around the point contact.

Table 4.3 Summary for the simulated drift paths for the Catequil detector with and without the additional charges on the groove surface.

field configuration	A/E at center point	A/E in the <100> plane	A/E in <110> plane	diff. center and <110>	diff. <100> and <110>
no charges	0.0855	0.0862	0.0863	0.86 %	0.14 %
add. charges	0.0752	0.0788	0.0799	5.9 %	1.4 %

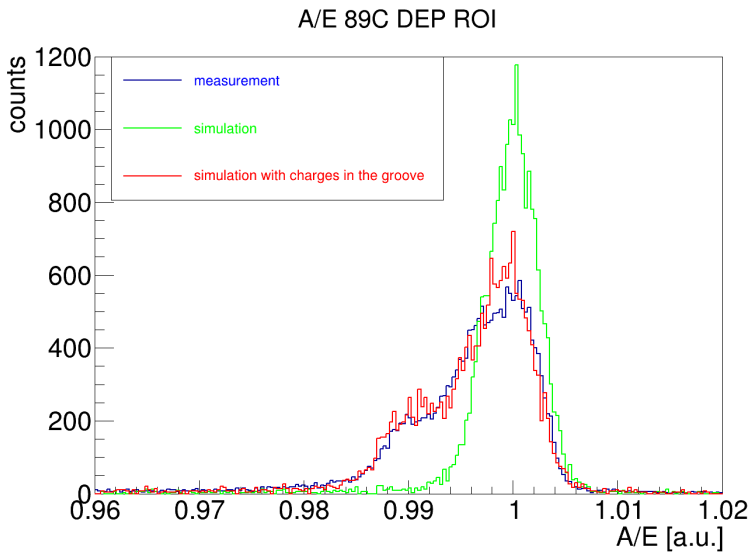

Fig. 4.33 Measured and simulated A/E distribution of the DEP events of ^{208}Tl in the Catequil detector. The distributions were normalized and the maximum was set to 1. In blue: Measurement. In green: Simulation. In red: Simulation with additional charges in the groove.

Fig. 4.33 shows the measured and simulated A/E distribution of the DEP events of ^{208}Tl line from the ^{228}Th chain. The simulation was done in the same way as the circular scan simulation and reproduces the measured results well. The good agreement strengthens the hypothesis that the spatial variation and degraded PSD performance is caused by additional charges in the groove.

4.7 Thermal cycle on detector Bes

In December 2012 a thermal cycle was performed on the Bes detector to check if an inhomogeneous charge distribution in the groove is responsible for the strong asymmetric A/E variation in the circular scans. The cold finger of the cryostat was placed in boiling water while the cryostat chamber was pumped. The rise in temperature increases the mobility of the trapped charges and either removes them or at least distributes them more homogeneously in the groove. As shown in fig. 4.34, the A/E scan after the thermal cycle has a less asymmetric distribution, which is more similar to the other detectors. After heating, the oscillation pattern along the crystal axis is visible even though the shape is still a little distorted. The difference between the minimum and maximum A/E value is still very big which indicates a dense charge distribution since the A/E spread between the center and outer positions scales with the amount of charges in the simulation. The change in the spatial A/E dependence after the

thermal cycle shows that this irregular dependence is caused by surface effects which change at a temperature of 100° C or less since the detector was only heated up to this temperature. Bulk crystal properties like impurity concentration or lattice defects are highly unlikely to change at this temperature.

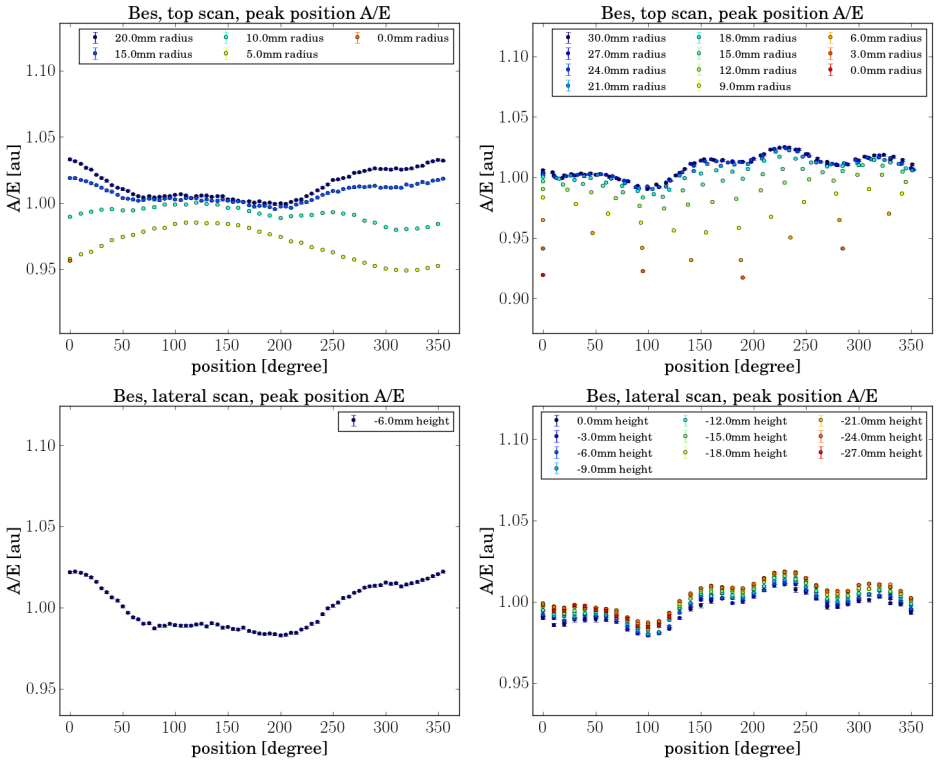

Fig. 4.34 Each point in the graph represents the mean of the Gaussian fitted to the A/E distribution in the 59.5 keV ROI. Top left: Bes top circular scan before thermal cycle. Top right: Bes top circular scan after thermal cycle. Bottom left: Bes lateral circular scan before thermal cycle. Bottom right: Bes lateral circular scan after thermal cycle.

4.8 Collimated ^{228}Th measurements on detector Bes

To verify the measured spatial A/E dependence in the ^{241}Am scans and check what role the event energy has on its distribution, collimated ^{228}Th measurements were performed on the Bes detector. The gammas from the ^{208}Tl line were collimated by a 5 cm thick lead brick with an 8 mm opening hole. One position at the center of the detector and four with distance of 30 mm from it were measured. Unfortunately only the center position and the point P1 were measured subsequently after each other without any changes on the system. Consequently only for these two measurements the A/E distributions are directly comparable

and do not need any normalization except on the total number of counts. Fig. 4.35 shows the two A/E distributions normalized to the number of events in the DEP ROI ($\pm 5\sigma$). The distribution in the center of the detector is wider and has a prominent left shoulder. Holes from the events collimated at the center drift directly to the point like contact and thus hit the whole of its surface. As shown in the previous section 4.6, the presence of additional charges in the groove can lead to a dependence of the A/E value on the impact point of the holes on the p^+-contact. The A/E distribution for the outer point is narrower and does not show a left shoulder like the central position. The holes from events in this region of the detector follow a similar path because of the funnel effect and thus have a similar A/E for SSE.

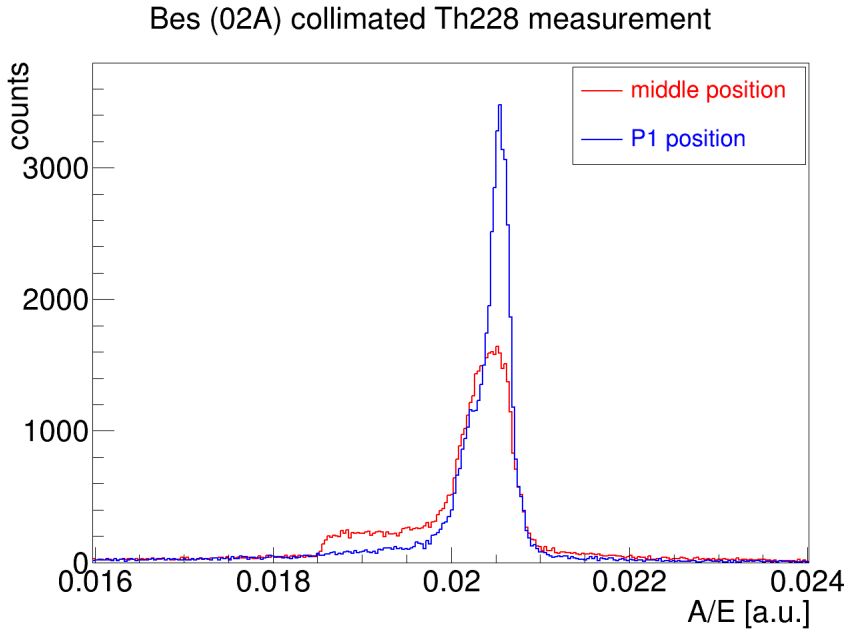

Fig. 4.35 A/E distribution for collimated ^{228}Th measurements on Bes: Red central point. Blue outer point with 30 mm distance from the center.

This measurement shows that the A/E degradation at the center is not caused by surface effects on the face side of the detector or due to the low energy of ^{241}Am gammas.

4.9 Conclusion

As described in this chapter, all detectors were successfully tested and scanned. Due to time constraints not all detectors could be scanned in full detail with the collimated ^{241}Am source, but the obtained results are sufficient to explain the observed effects and anomalies. It was shown through simulations that the asymmetric and broad A/E distribution for the DEP in the

^{228}Th measurements as well as the degradation of the A/E value towards the center and the oscillation along the crystal axis in the ^{241}Am-scans are linked to additional charges located on the passivation layer in the groove. It was shown by M. Barnabé Heider [63] that the passivation layer can trap free charges. This negative effect can be neutralized by removing the passivation layer through additional etching of the groove before the integration of the detectors in GERDA. Fortunately, the passivation layer is not mandatory for a low leakage current when the detectors are operated in a liquid noble gas which is the case in GERDA.

Chapter 5

Ultra high purity germanium detectors

To minimize the background caused by ambient radiation sources, it is advantageous to minimize the detector surface to volume ratio since this increases the self shielding effect. Higher mass of individual detectors reduces the amount of readout channels and electronic components close to the detectors. Nevertheless the impurity concentration must be kept to a very low level to enable the full depletion of the detectors at a reasonable bias voltage ($\lesssim$ 5 kV). Furthermore, in modern detectors with a point contact design the electric field in the corners is dominated by the impurity concentration and not anymore by the bias voltage like in the coaxial configurations. This can lead to low electric field regions causing an enormous increase of the charge cloud size and, as shown in the following chapter, to a degradation of the pulse shape discrimination performance described in section 2.5. To measure this effect and gain more knowledge on the charge cloud size evolution two prototype detectors (PONaMa I and PONaMa II) manufactured by ORTEC were tested and characterized at the Lawrence Berkeley National Laboratory. Table 5.1 summarizes the general specifications and performance parameters of the detectors. Both crystal slices were cut from the same ultra pure p-type ingot. PONaMa I was built from the part close to the seed and has an average net impurity concentration of $\sim 2.5 \cdot 10^9\, cm^{-3}$ which is one magnitude purer than usual detectors. PONaMa II has even a lower net impurity concentration of $\sim 6 \cdot 10^8\, cm^{-3}$ (between $\sim 2 \cdot 10^9\, cm^{-3}$ and zero). The tail part it was made of stays longer in the liquid phase, which has a higher solubility for n-type impurities.

Two kinds of measurements were performed on these detectors, first a radial scan with a collimated ^{241}Am source and second a drift time coincidence measurement with a NaI detector using a ^{22}Na source. The following chapter will describe the experimental setups in detail and discuss the physics results. See also [64].

Table 5.1 Summary of the general specifications and performance parameters of PONaMa I and II provided by the manufacturer and measured at LBNL. The operation voltage is chosen to be much higher than the depletion voltage to ensure full charge collection efficiency in the detector corners.

	PONaMa-I	PONaMa-II
Height	50.5 mm	47 mm
Radius	34.5 mm	34.5 mm
Leakage current	3.4 pA	6.4 pA
Capacitance	1.64 pF	1.56 pF
Operating voltage	2000 V	3000 V
Depletion voltage	880 V	450 V
Deduced mean impurity concentration	$\sim 2.5 \cdot 10^9$ cm^{-3}	$\sim 6 \cdot 10^8$ cm^{-3}
FWHM @ 1.33 MeV	2.11 keV	1.99 keV
FWHM @ 59.5,keV	603 eV	666 eV

5.1 PONaMa field simulation

The electric and weighting fields for both PONaNa detectors were simulated with `mjd_fildgen` as described in chapter 3. The impurity concentration and gradient were optimized to be in agreement with the numbers provided by the manufacturer and the dedicated measurements. The measurement of the depletion voltage is a good way to determine the impurity concentration since both values are directly connected to each other. In the simplest configuration of a planar detector the depletion voltage V_D is given by:

$$V_D \cong \frac{d^2 e N_I}{2\varepsilon}$$

where d is the detector height, e the electric charge, ε the permittivity and N_I the net impurity concentration [25].

Fig. 5.1 shows the simulated electric field and potential for PONaMa I and its components. The electric potential is dominated by the bias voltage close to the point contact but in the corners it is caused by the impurities. A clear gradient is visible towards the point contact and thus defines the drift paths for the charge carriers. The weighting potential responsible for the signal formation is localized around the point contact and is close to zero in the upper third of the detector.

PONaMaİI effectively has no net impurities close to the top surface and the corners. This results in a shallow electric potential and a weak electric field in these regions as shown in fig. 5.2. The electric field here drops to values of ∼20 V/mm. The mobility of charge carriers

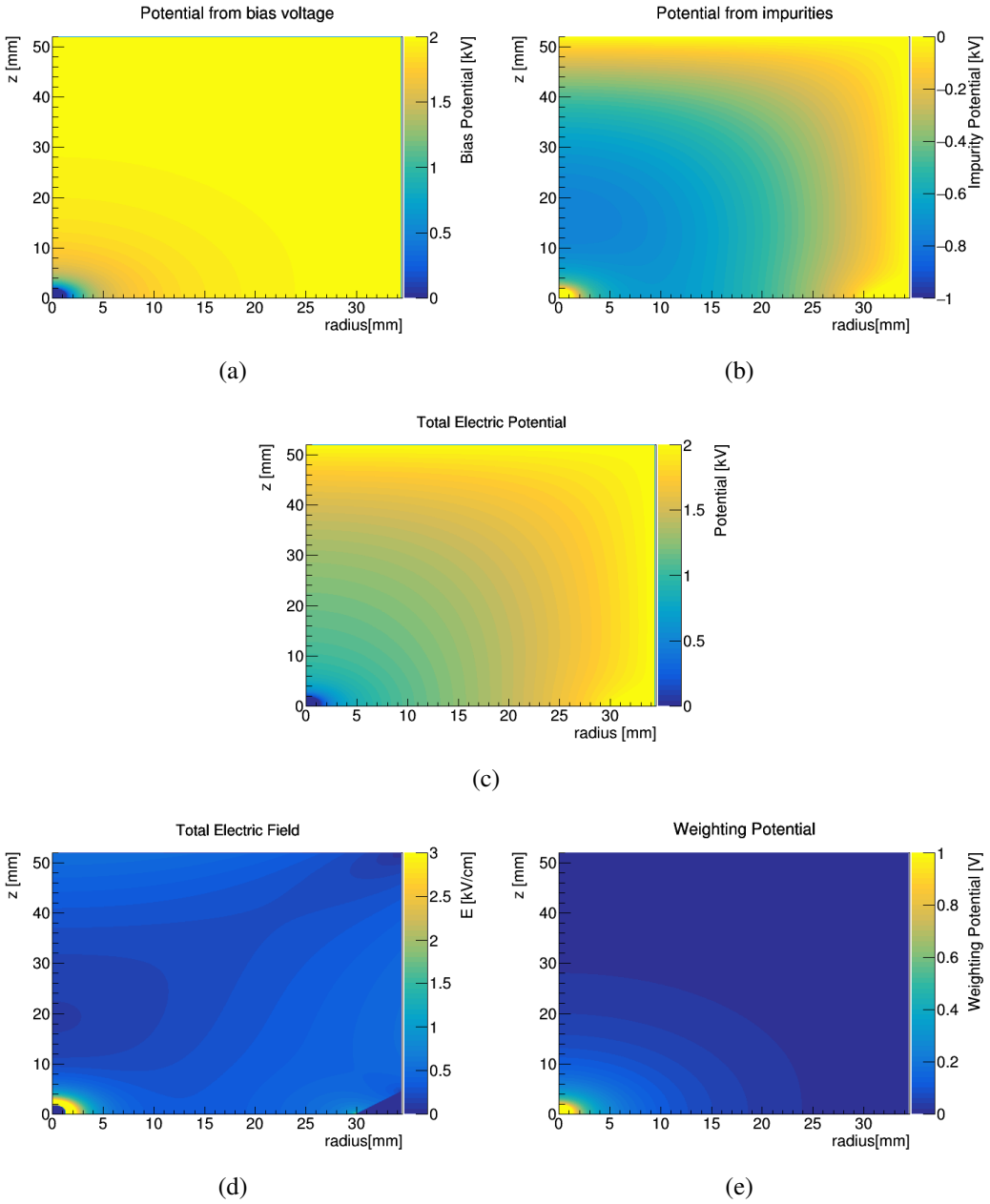

Fig. 5.1 Simulated electric and weighting potential in PONaMa I. (a) Potential generated by bias voltage, (b) Potential generated by impurity concentration, (c) superposition of (a) and (b), (d) the total electric field and (e) the weighting potential.

in these low fields are not well known which introduces a big uncertainty into the drift time simulation and the charge size evolution.

5.2 ^{241}Am scanning measurements

Scanning a detector with a collimated ^{241}Am source provides information on the spatial dependence of pulse shapes, especially on the A/E parameter since the majority of the events have a SSE signature as described in section 4.3. A linear scan was performed on both ORTEC prototype detectors to measure the radial dependence of the key parameters like charge collection efficiency, rise time and the A/E pulse shape discrimination parameter.

5.2.1 Experimental setup

An automated scanning setup was built for this purpose and is shown in fig. 5.3. The ^{241}Am source is collimated by a tungsten disc with an opening of 1 mm and is placed in an aluminum housing. The apparatus has an electrical motor which moves the source with a precision of 1 mm and is controlled with the ORCA [65] DAQ software. ORCA is also used to record the detector pulses which are digitized with the Struck SIS3302 FADC. The dynamic range of the used Struck card is 10 V which unfortunately leads to a low signal to noise ratio for the 59.5 keV events of the ^{241}Am source as shown in fig. 5.4. Nevertheless, the data quality is good enough to measure the important parameters.

5.2.2 Results and simulations

The top surface of both detectors was scanned in 1 mm steps and the events in the 59.5 keV ROI ($\pm$ 2 σ) were selected to extract the key parameters. The pulse shapes were then simulated with the MaGe and `mjd_siggen` package to compare the model with the results. The response of the preamplifier circuit was simulated with a RC-integration with a time constant of 26 ns for PONaMa I and 21 ns for PONaMa II. These values are a free parameter in the simulation and were optimized to reproduce the measured results.

Charge collection efficiency

The most important parameter for the detector performance is the uniformity of the charge collection efficiency. This parameter can easily be measured by the amount of counts in the 59.5 keV peak in such an ^{241}Am scan with a fixed exposure time. The 59.5 keV peak was fitted with a Gaussian and a step function in the same way as described in section 4.4 and

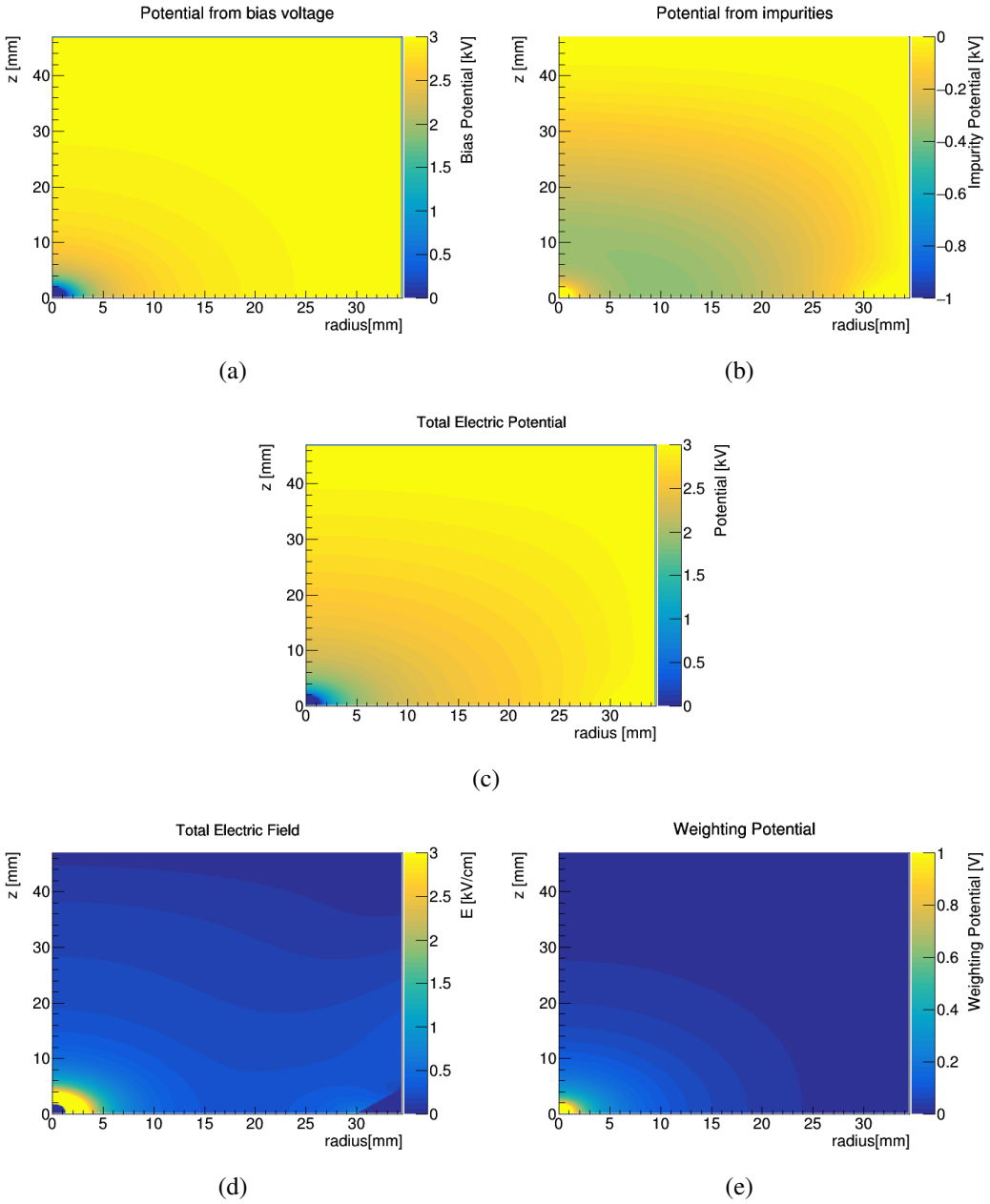

Fig. 5.2 Simulated electric and weighting potential in PONaMa II. (a) Potential generated by bias voltage, (b) Potential generated by impurity concentration, (c) superposition of (a) and (b), (d) the total electric field and (e) the weighting potential.

Fig. 5.3 Photograph of the ^{241}Am scanning setup at LBNL

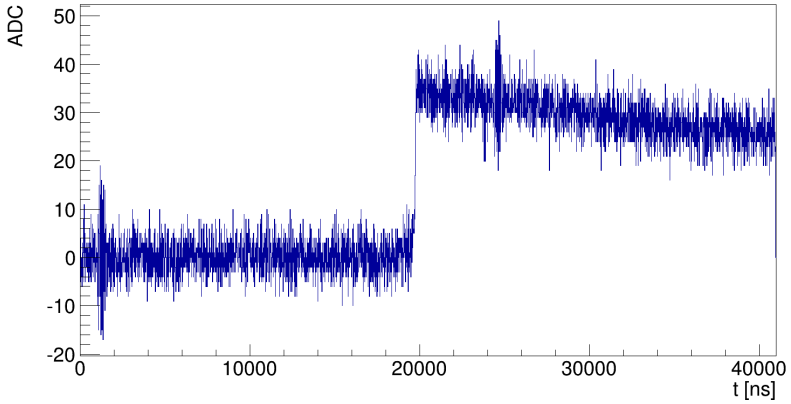

Fig. 5.4 Example pulse of the PONoMa I detector illuminated with a collimated ^{241}Am source. The displayed pulse corresponds to an energy deposition of 59.5 keV.

shown in fig. 5.5 and fig. 4.7. As illustrated in fig. 5.6 both detectors show a stable rate along the top surface and only in the corners the rate drops a little. This drop is unlikely to be caused by an inhomogeneous dead layer width. The dead layer is produced by an diffusion process and thus its width should be relative stable across the same surface. Its more likely that the decrease in the rate is caused by a low charge collection efficiency due to a low electric field. This is well reproduced in the simulations.

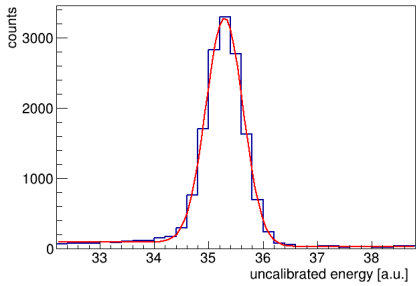

Fig. 5.5 In blue the 59.5 keV peak in the ^{241}Am spectrum, in red the Gaussian fit with a step function

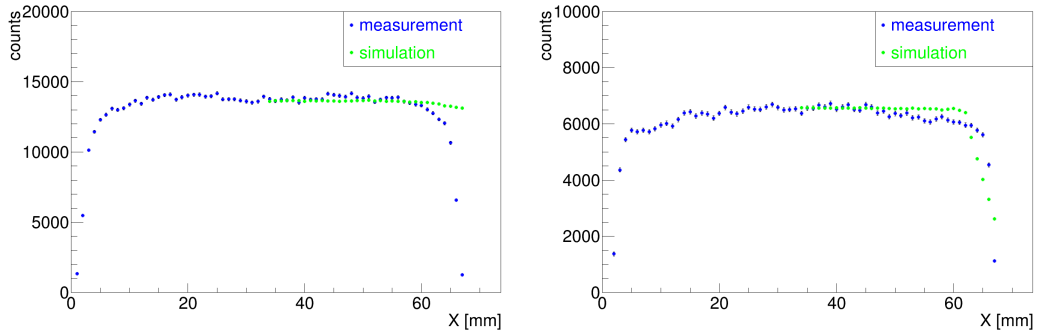

Fig. 5.6 Linear scans of the PONaMa detectors: Left PONaMa I and right PONaMa II. In blue the measured and in green the simulated number of counts in the 59.5 keV ROI. The simulated results were scaled to the measured numbers and provide a qualitative value of the uniformity of the charge collection.

A/E parameter

The A/E parameter for all events in the 59.5 keV ROI and each point in the scan was histogrammed and fitted with a Gaussian as shown in fig. 5.7. The parameter is stable along the radius for PONaMa I but decreases for PONaMa II with the radius as illustrated in fig. 5.7 and fig. 5.8. The ultra high purity of PONaMa II leads to extremely low electric field in

the corners. This results in a low initial drift velocity, long drift times and a stretching of the charge cloud. Fig. 5.9 shows example pulses and the corresponding A/E parameters at different radii for PONaMa II. At a distance of 30 mm the rise of the pulses is so slow that the maximum of the differentiated pulse is dominated by noise and the A/E parameter drops to its minimum.

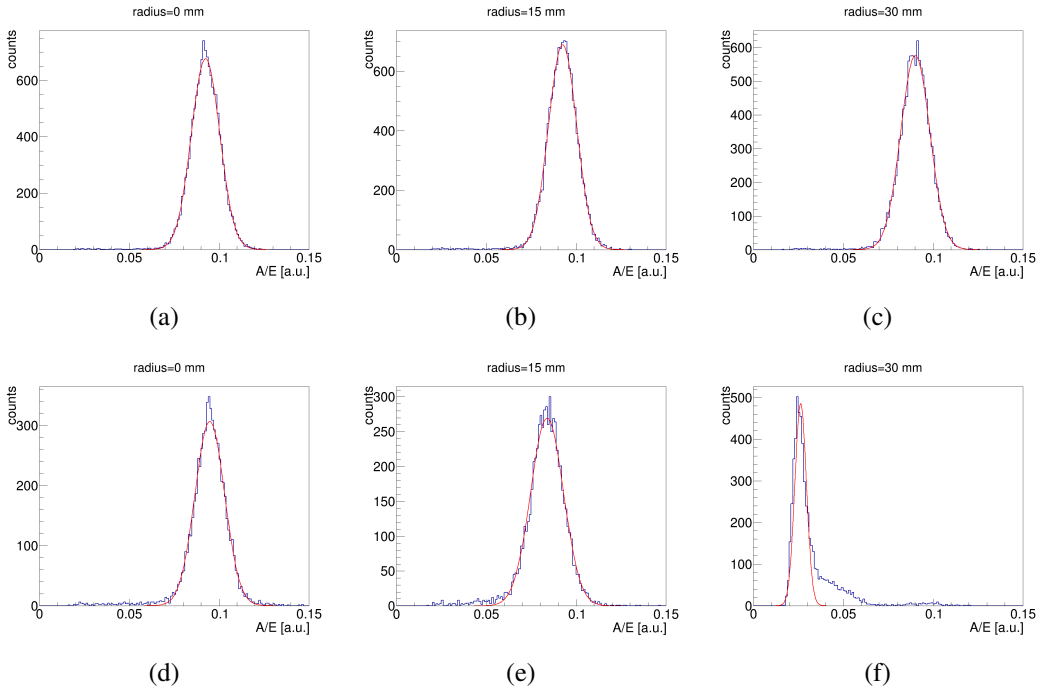

Fig. 5.7 A/E distribution of the 59.5 keV events at different radii (0 mm, 15 mm and 30 mm). In blue the histogrammed data and in red the Gaussian fit. Top row is showing PONaMa I and bottom row PONaMa II.

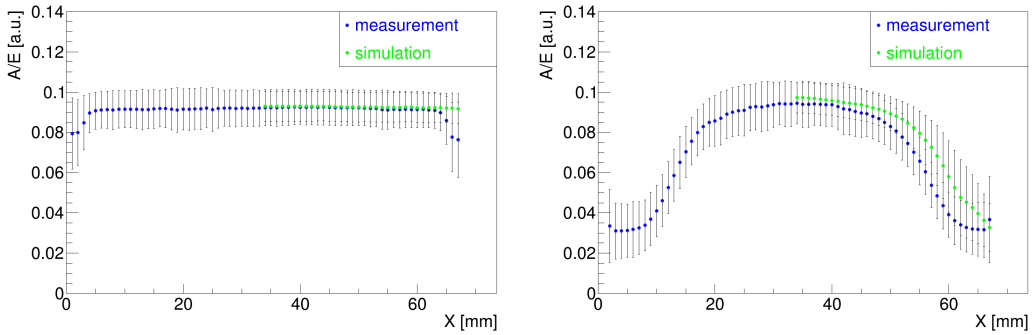

Fig. 5.8 Linear scans of the PONaMa detectors: Left PONaMa I and right PONaMa II. In blue the measured and in green the simulated A/E distribution in the 59.5 keV ROI.

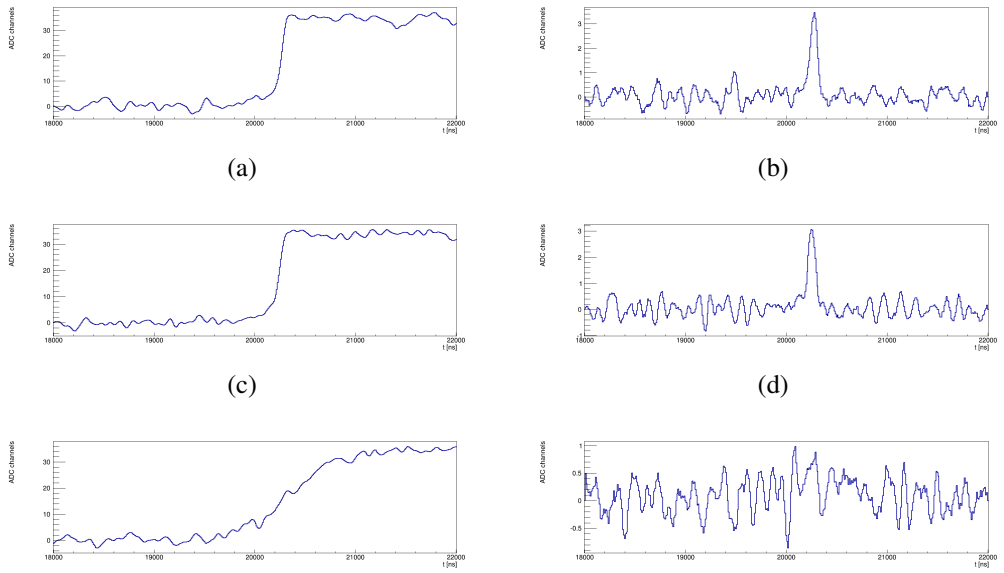

Fig. 5.9 PONaMA II sample wave forms for a 59.5 keV event at different radii ((a) at 0 mm, (c) at 15 mm and (e) at 30 mm). The left column is showing the charge pulse and the right column its derivative with its maximum A.

This behavior was partially reproduced in the simulations but not to the full extent. This is due to the incomplete knowledge of the impurity distribution in the crystals which is needed for the field simulation. The transition layer is also not modeled yet in the simulation and could play a role in the A/E degradation at low fields.

Rise time

The 1-90 % rise time of the pulses was analyzed in the same way as the A/E parameter. As shown in fig. 5.10, the 1-90 % rise time for PONaMa I stays constant over the whole surface, which is due to the high noise which does not allow to reconstruct the precise time the pulse reaches 1 % of it maximum. As expected the simulated drift time shows a clear radial dependence and is much higher than the measured 1-90 % rise time. The charge carriers created by incident radiation close to the detector top surface drift for a long time $\sim$ 500 ns in a low weighting potential (see fig. 5.1 (e) and fig. 5.2 (e)) and thus induce nearly no charges on the read out electrode. The pulse creation starts when the charge cloud reaches the strong weighting potential close to the point contact.
Due to the extreme low field in the corners of PONaMa II the 1-90 % rise time increases dramatically for events with a distance greater than 20 mm from the detector center. The pulse shapes in this region are degraded to slow pulses. This behavior is only partially reproduced

in the simulations. An implementation of a transition layer could help to reproduce the measured results and should be further investigated. The time charge carriers need to diffuse out of the transition layer would further increase the charge cloud size and thus reproduce the observed slow pulses.

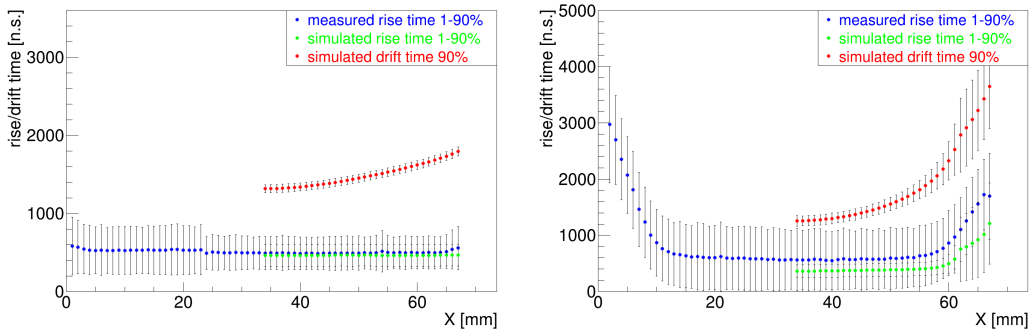

Fig. 5.10 Linear rise time scans of the PONaMa detectors: Left PONaMa I and right PONaMa II. In blue the measured and in green the simulated 1-90 % rise time distribution in the 59.5 keV ROI. Additionally the simulated drift time until the pulse reaches 90% of its maximum is plotted in red.

5.3 Coincidence measurements

Germanium detectors with a point contact geometry do not provide a direct information on the charge drift because of the localized weighting potential. The charge carriers can drift in the detector without any measurable induced charges on the readout electrode until they arrive at the strong weighting potential close to the point contact. The drift time can be measured by a coincident measurement where a second fast detector e.g. NaI provides the start of the signal. For this kind of measurements a β^+ source is used since it provides two back to back gammas with an energy of 511 keV from the positron annihilation. One gamma hits the germanium detector and the second one is used for the timing measurement.

5.3.1 Experimental setup

For the drift time measurement at the LBNL a collimated ^{22}Na source and a NaI detector were used (see fig. 5.11). The scintillation light produced in the NaI crystal is measured with a photomultiplier tube which provides a sharp and fast signal. The gammas from the ^{22}Na source are collimated with a lead brick pierced with an 1.8 mm hole to illuminate a specific region in the germanium detector. Three positions were measured in these tests

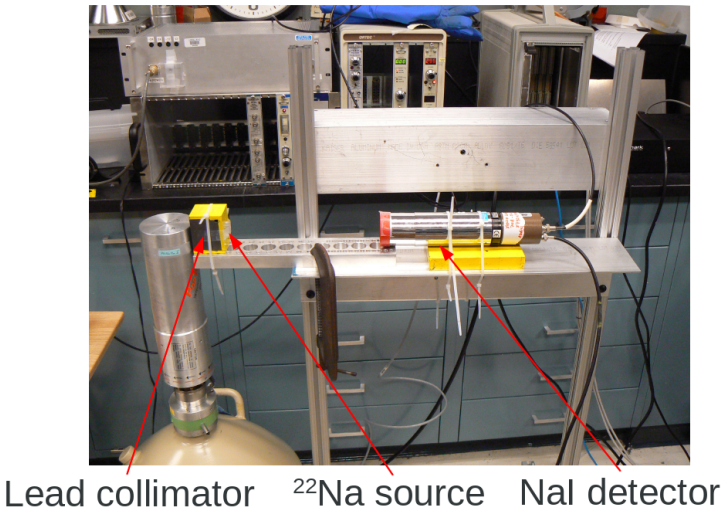

Fig. 5.11 Photograph of the drift time measurement setup at LBNL. The two back to back gammas from the ^{22}Na source are detected with a germanium and a NaI detector.

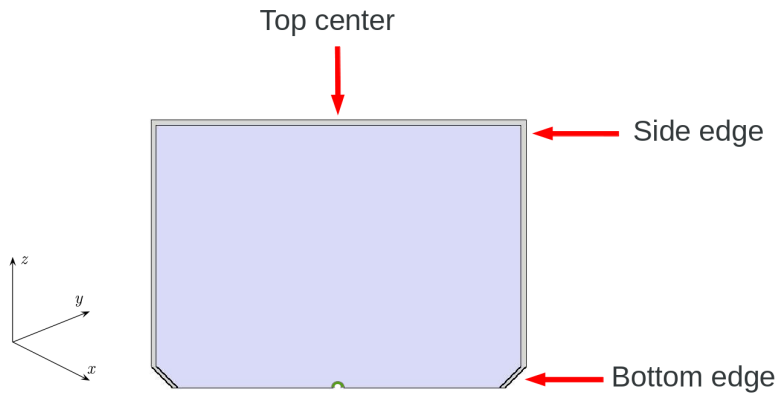

Fig. 5.12 A schematic drawing of a PONaMa detector and the source positions for the coincident measurements. The red arrows show the gamma beam direction.

(see fig. 5.12): One directly at the center of the detector pointing towards the point contact. This position measures the direct drift along the z-axis and provides interaction points close to the point contact in the localized weighting potential where both charge carrier types contribute to the germanium signal. This is also valid for the bottom edge position where the illumination comes from the site directly above the point contact. Here the drift is minimal in the z direction and covers the full drift path range in the xy-plane. In the last position the detector is illuminated at the top side edge towards the center. Here the path along the z-axis is maximal and in the xy-plane it varies from minimum to maximum. In this position the longest drift paths and drift times are reached, also the interaction points of the incident radiation are located in the weak electric field regions.

5.3.2 Analysis chain

The waveforms from the germanium and the NaI detector are both digitized with the same Struck SIS3302 FADC and then analyzed with GELATIO. Fig. 5.13 shows a sample for both waveforms and the time structure. The NaI pulse rises fast and thus provides an exact timing for the event start. The coincident events were selected as followed:

- energy deposition of 511 keV $\pm 1\sigma$ in both detectors see Fig. 5.14
- only one pulse present in the NaI detector trace to ensure the right timing
- NaI pulse appears before the germanium pulse

5.3.3 Results and simulations

Similar to the ^{241}Am scans the experimental setup was simulated with MaGe and `mjd_siggen`. The NaI detector is not considered in the simulations since the event start is known per default in the simulated pulses.

Drift time

The time difference between the NaI pulse and the time the germanium detector signal reaches 90 % of its maximum value defines the drift time of the holes. This is not valid for pulses close to the point contact since in this region also the electrons contribute to the signal formation.
Fig. 5.15 shows the measured and simulated results for the two PONaMa detectors. The drift times for PONaMa I vary between 100 ns for pulses close to the point contact and 2000 ns

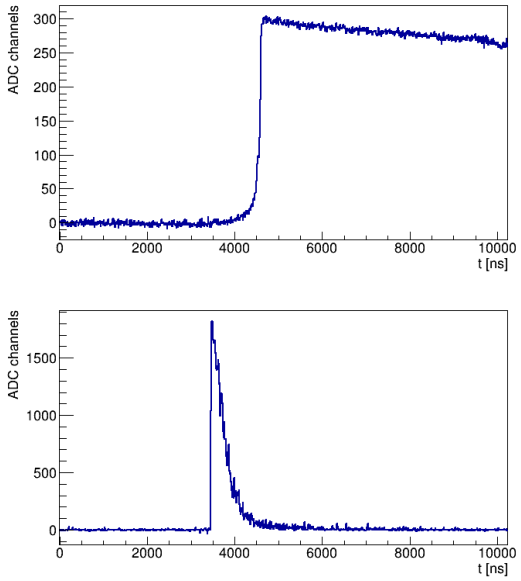

Fig. 5.13 Drift time measurement sample waveform. Top: PONaMa I trace of a 511 keV event. Bottom: NaI trace of a 511 keV event. Time difference between the NaI event and the time the PONaMa I signal reaches 90 % of its maximum values defines the drift time of the charge carriers.

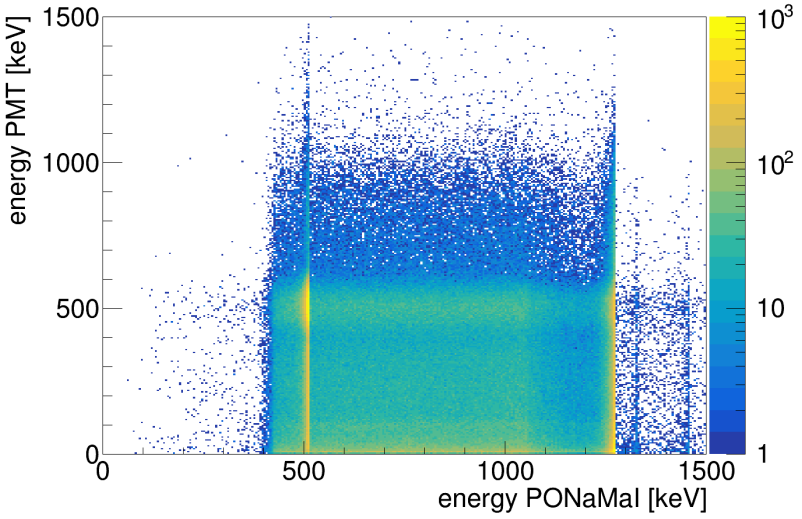

Fig. 5.14 Scatter plot of the detected energy in the PONaMa I and the NaI detector. The number of events is color coded in log scale. A clear enhancement is visible at 511 keV for both detectors.

for events in the top corner. In general, the simulation reproduces the spectral shape of the drift time distribution for PONaMa I quite well. Two features of the measurement are not reproduced properly. First, the very fast events close to the point contact in the top center and side bottom positions are slower in the simulation. This is also the case for the top center position of PONaMa II and thus seams a systematic calculation error in the high weighting potential region. Second, the simulation produces much more pulses with a drift time bigger than 800 ns in the side bottom position than there are in the measurement. All these events are produced by gammas which scattered towards the top of the detector and thus deposited energy farther away from the point contact.
The simulation for PONaMa II also reproduces the measured results well except the side bottom position. In the measurement the peak for fast drift times is missing and the overall spectral shape tend much more to long drift times than in the simulation and for PONaMa I (see fig. 5.15 (d)). In the side bottom position both detectors should show a similar spectral shape since the lower parts of the detectors are geometrically identical. Also the field in this region is dominated by the bias voltage and thus the impurity configuration should not play a large role. The different spectral shape can be well explained by a tilt of the collimator from the y-axis by some degrees. In that case less gammas would hit the strong weighting potential region close to the point contact. For the side bottom position the amount of events close to the point contact is normally large because of the radial detector symmetry. This is visible as an enhancement at fast drift times for PONaMa I (see fig. 5.15 (c)). The tilt would also explain the high number of slower pulses for PONaMa II since it would produce more events farther away from the point contact than a straight beam along the y-axis.

Rise time

The 1-90% rise time agrees well with the drift time for the most parts in the detector as shown in fig. 5.16 and thus can be helpful to characterize detector pulses. It can also be used to improve the energy resolution by correcting the charge collection efficiency for the the drift time dependent charge trapping effect as described in [66]. Only for the side edge position the 1-90% rise time fails to reproduce the actual drift time. In this position the charges drift a long distance in a very weak weighting potential and so do not induce a measurable signal on the read out electrode. This makes it very difficult to measure the exact time when the signal reaches 1% of its maximum with the given electronic noise.
The simulated rise times shown in fig. 5.17 match the measured data for PONaMa I in all positions which means that the drift paths, the electric and weighting potential and their gradients are well reproduced in the simulation. This is not the case for the side edge and side bottom positions of PONaMa II but in the top center position, simulation and measurement

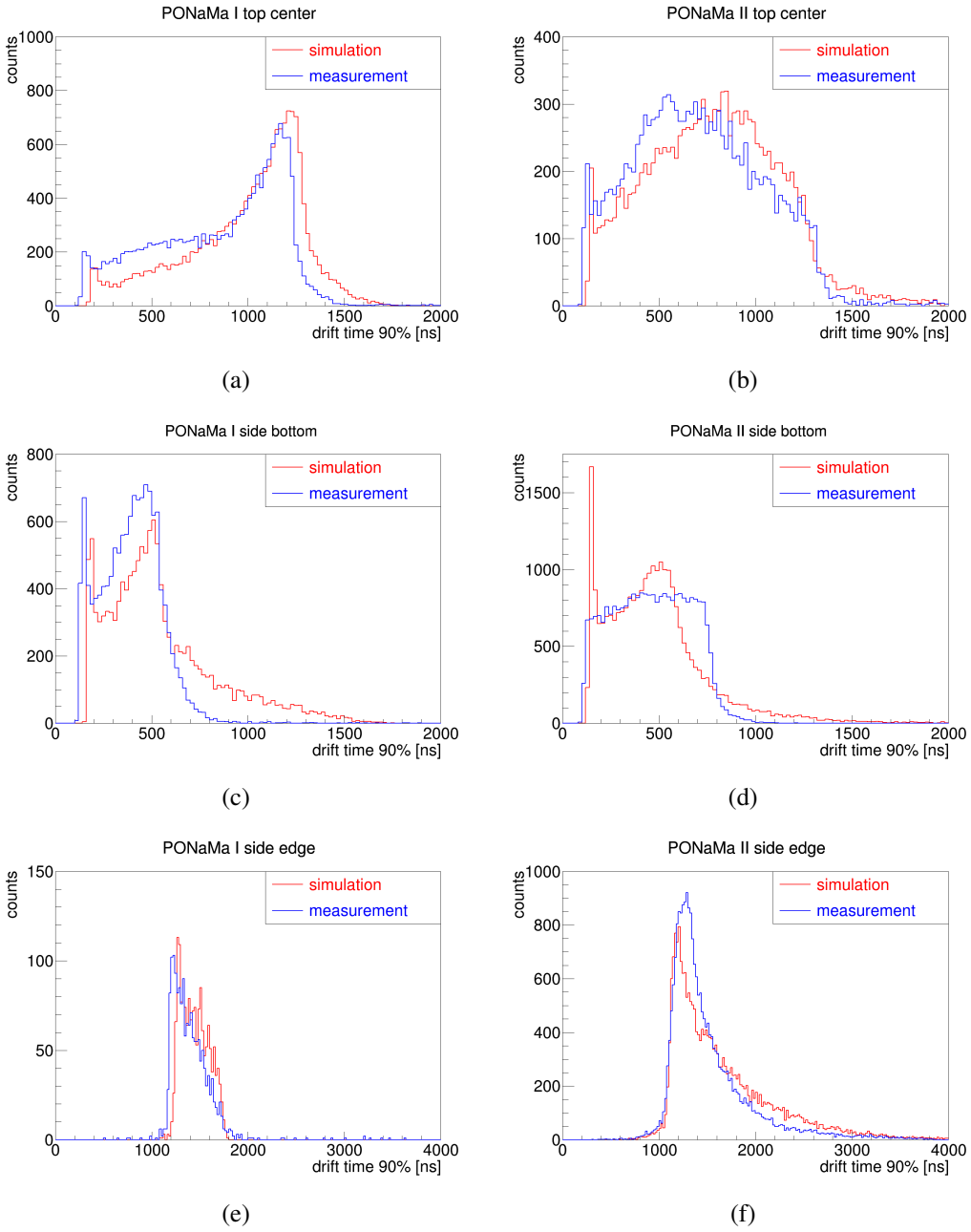

Fig. 5.15 PONaMA I/II: Drift time distribution for the three collimator positions with the measured data in blue and the simulated in red. (a)/(b) at the top center, (c)/(d) at the side bottom and (e)/(f) at the side edge position.

fit well to each other. This indicates that the general impurity profile was chosen correctly for the simulations and only the low field regions with their big uncertainties on the charge carrier mobilities are not reproduced correctly.

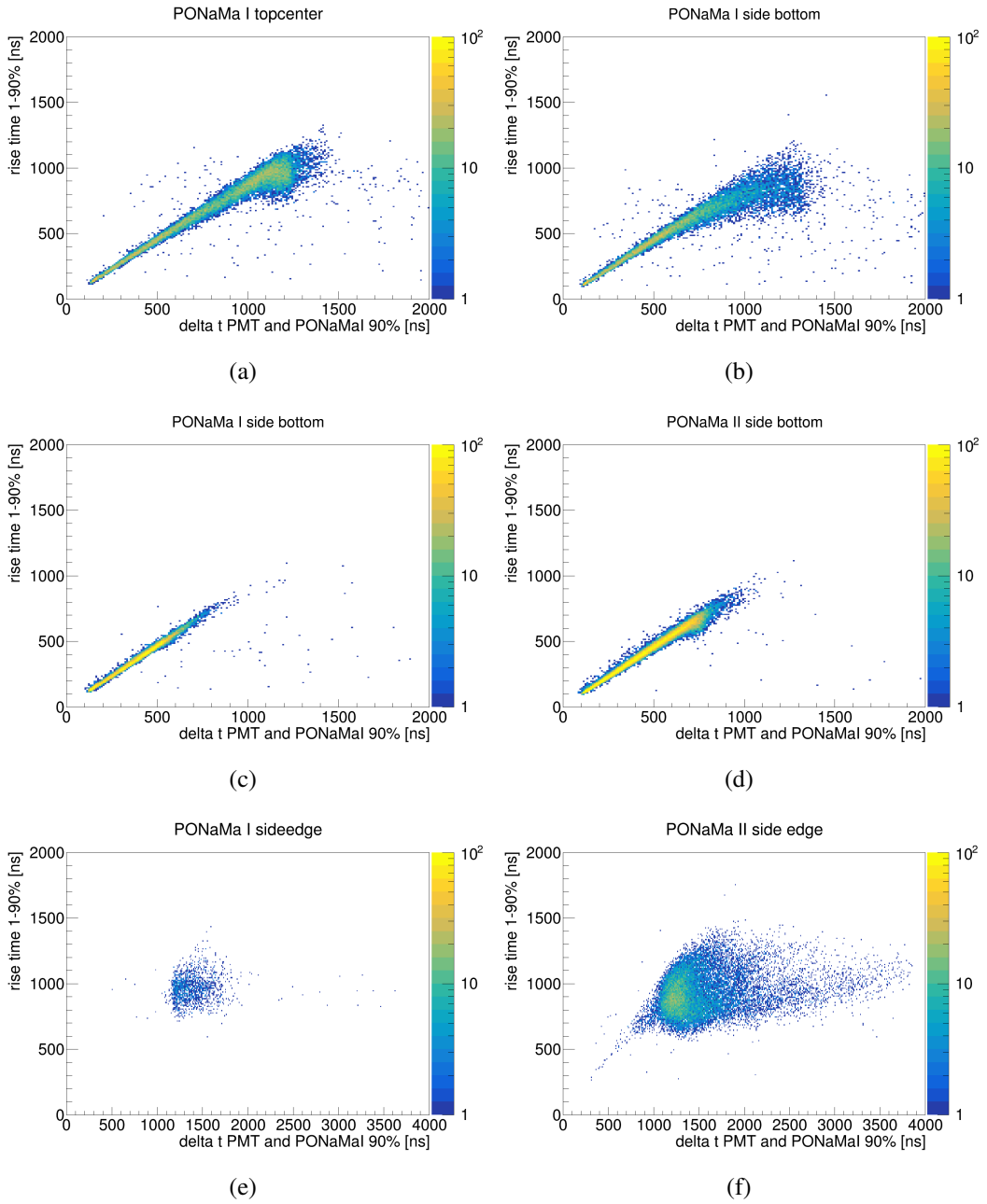

Fig. 5.16 PONaMA I/II: 1-90% rise time vs drift time distribution for the three collimator positions. (a)/(b) at the top center, (c)/(d) at the side bottom and (e)/(f) at the side edge position.

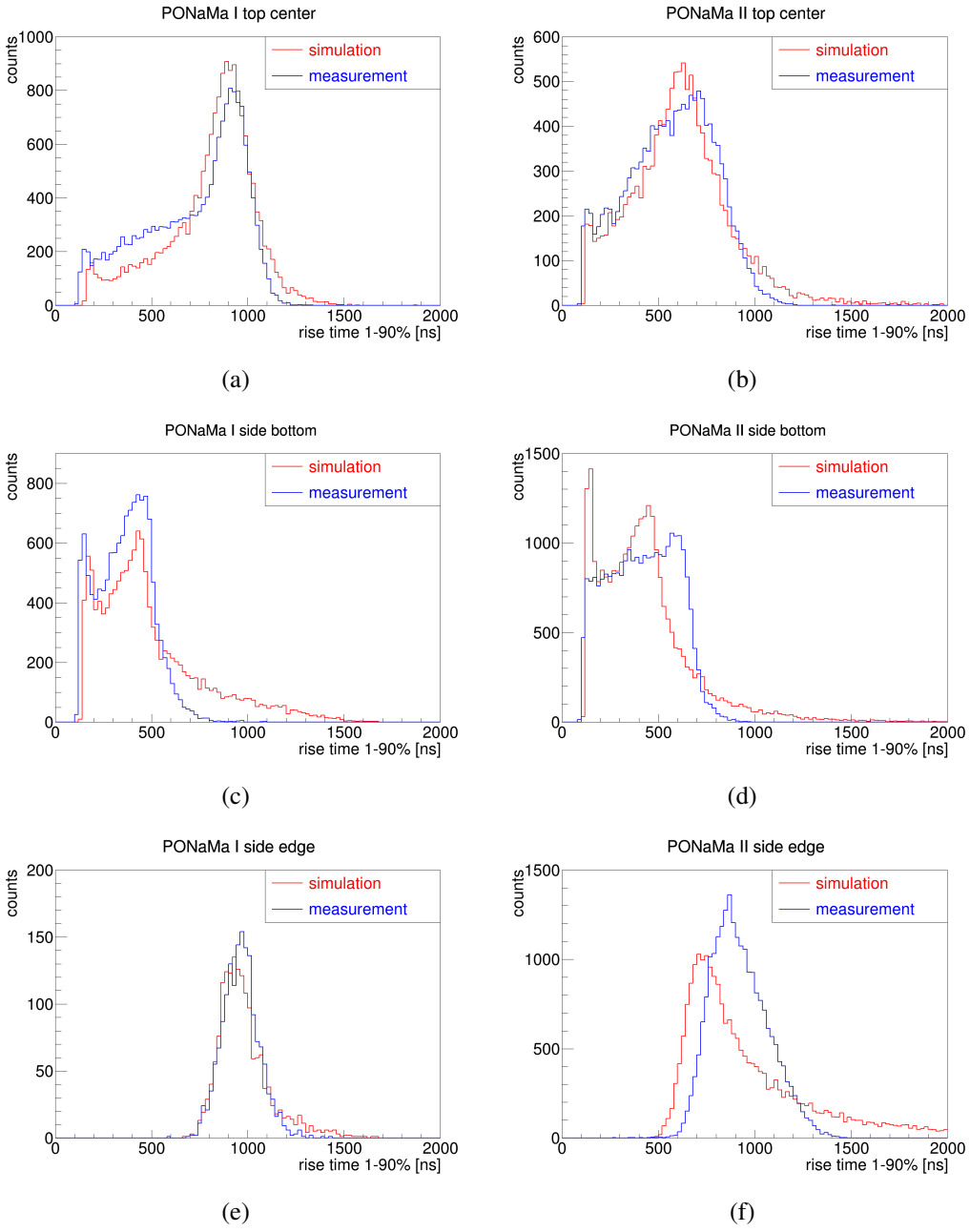

Fig. 5.17 PONaMA I/II: 1-90% rise time distribution for the three collimator positions with the measured data in blue and the simulated in red. (a)/(b) at the top center, (c)/(d) at the side bottom and (e)/(f) at the side edge position.

A/E parameter

The A/E parameter used for the pulse shape discrimination between multi and single site events varies with the final charge cloud size. Because of its spatial extension the individual charge carriers arrive with a delay at the read out contact and thus stretch the signal in the time domain. For large charge clouds the maximum of the derivative of the charge pulse A decreases to lower values. In detectors with an extremely low electric field, the initial charge carrier velocity is very small ($\sim$0.002 mm/ns) which already leads to a massive increase of the cloud size through the acceleration effect described in section 3.2.2. Additionally, during the long drift time to the point contact, in case of PONaMa II this can take up to 5 μs, the charge carriers drift farther apart from each other and the charge cloud grows up to several mm.
Fig. 5.18 shows the A/E distribution for the PONaMa detectors in the three measurement positions. In both detectors, in the top center and side bottom position, a satellite peak for higher A/E values than the main SSE peak is visible. This peak corresponds to the events close to the point contact since here also the electrons contribute to the pulse formation. This is also clearly visible in fig. 5.19, where the A/E parameter is plotted versus the drift time, since the high A/E values correspond to fast drift times for events close to the point contact. In all positions the A/E band for SSE decreases minimally with higher drift times except for the side edge position of PONaMa II where it drops drastically with the drift time. The comparison between PONaMa I and PONaMa II shows that the drift time alone is not responsible for the A/E degradation since the parameter stays stable in the side edge position of PONaMa I (see fig. 5.3.3(e)) even for events with drift times grater than 1.5 μs. At the same time it degrades rapidly in case of PONaMa II since the electric field is much lower in the corners. This shows that it is the final charge cloud size which defines the A/E value. Fig. 5.20 illustrates the influence of the diffusion process on the A/E parameter and shows that a combination of all processes together, as described in section 3.2.2, are needed to model the experimental data.

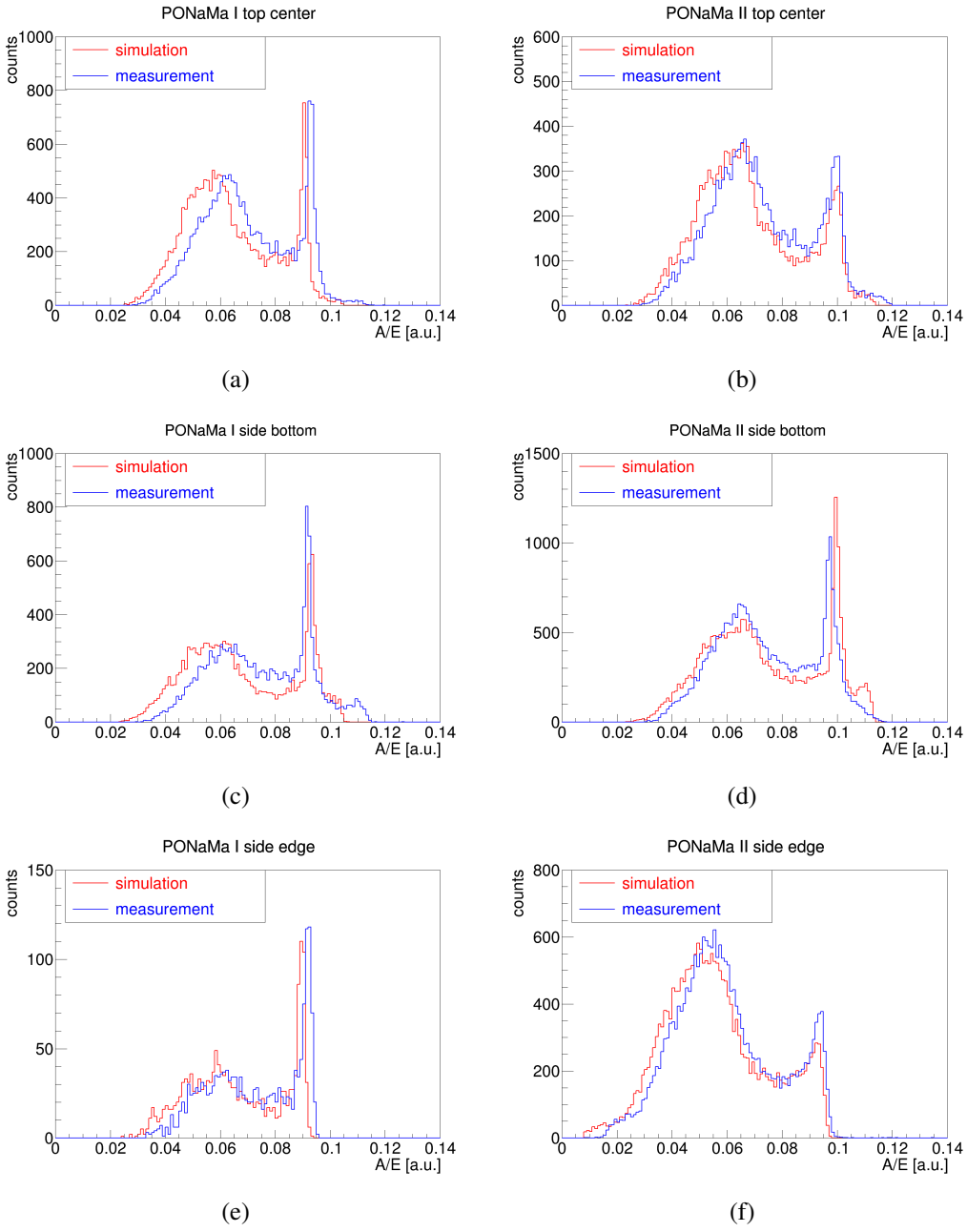

Fig. 5.18 PONaMA I/II: A/E distribution for the three collimator positions with the measured data in blue and the simulated in red. (a)/(b) at the top center, (c)/(d) at the side bottom and (e)/(f) at the side edge position.

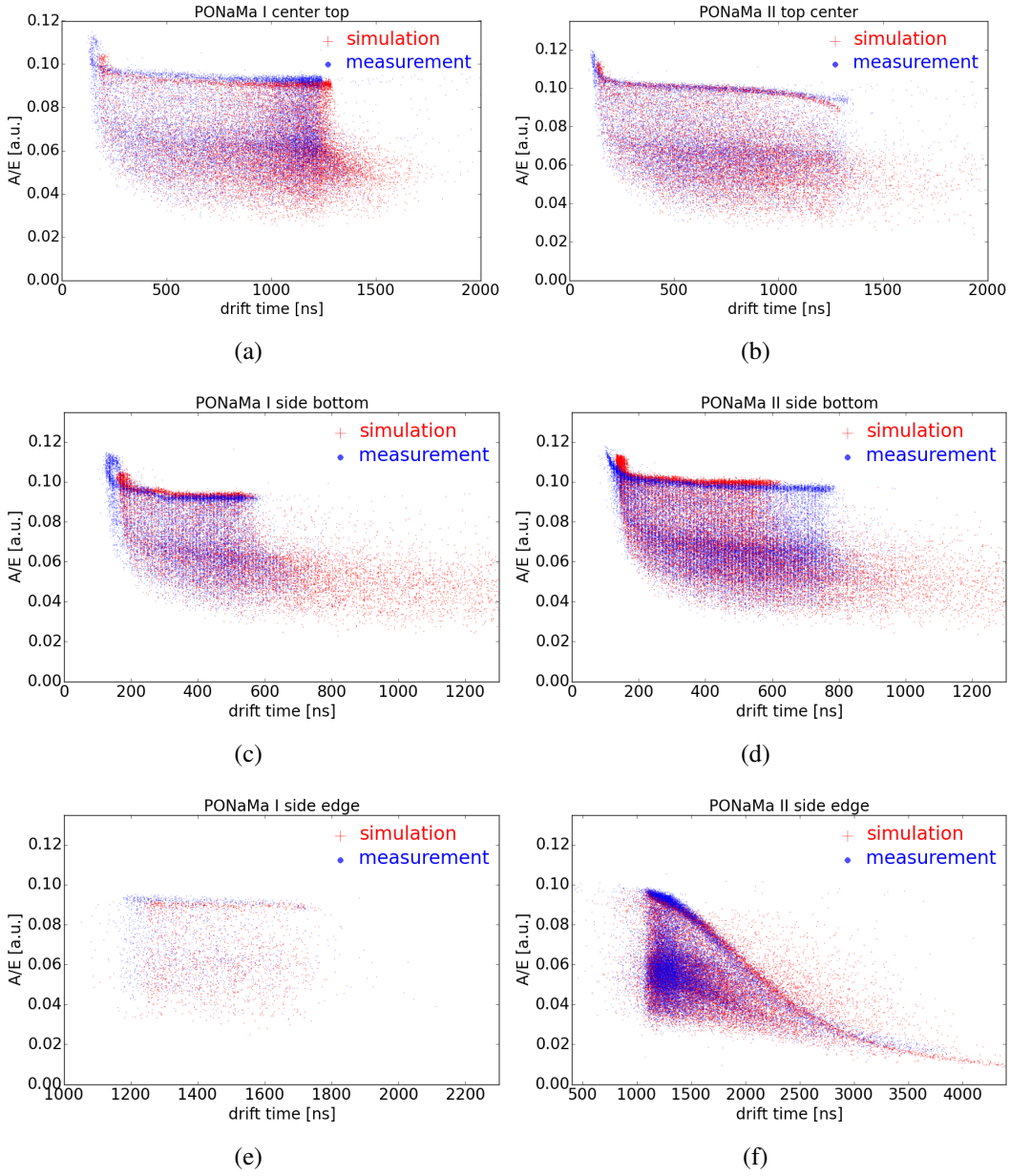

Fig. 5.19 PONaMA I/II: A/E vs drift time distribution for the three collimator positions with the measured data in blue dots and the simulated in red crosses. (a)/(b) at the top center, (c)/(d) at the side bottom and (e)/(f) at the side edge position.

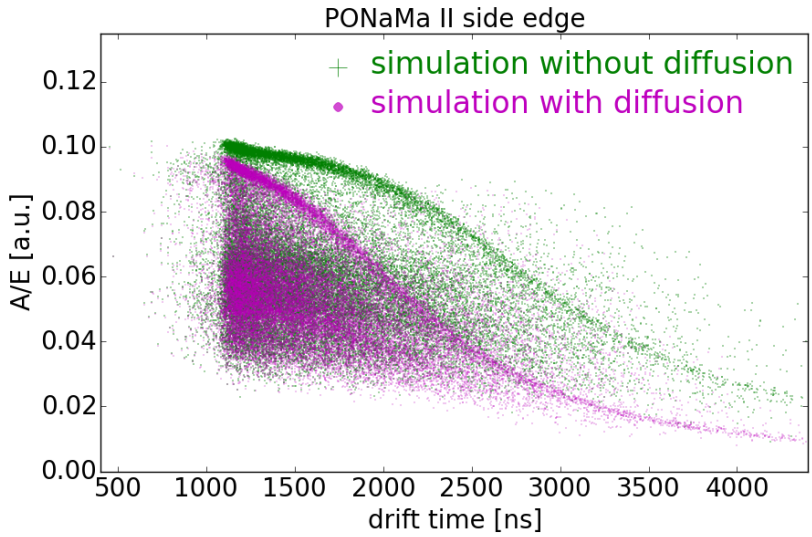

Fig. 5.20 PONaMA II: A/E vs drift time simulated distribution for the side edge position. For the green data set the diffusion process was disabled in the simulation. The data set in magenta was simulated with the charge cloud diffusion.

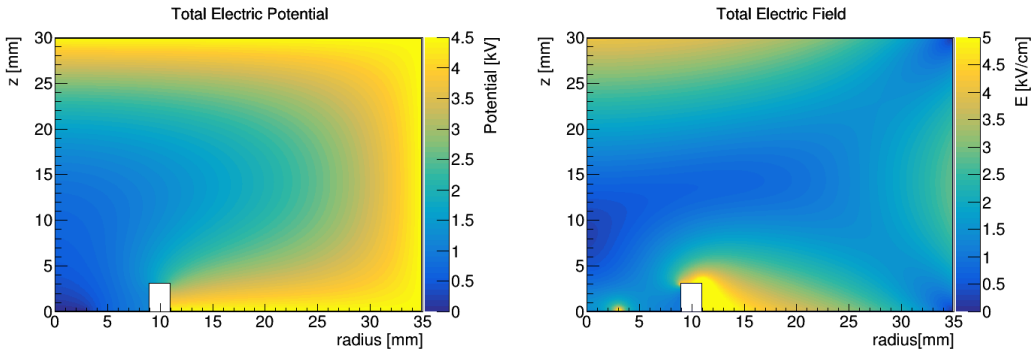

(a) (b)

Fig. 5.21 Simulated electric potential (a) and field (b) in B8684

5.4 Reference measurement

Two BEGe detectors were measured in the same way as the PONaMa detectors as a reference. The first BEGe detector (B8684) was produced by Canberra Meriden (US) and has a small point contact with a diameter of 6 mm. The second BEGe (DD) was manufactured by Canberra Olen (BEL) and has a standard point contact with a diameter of 15 mm. Both detectors have a similar mass of ∼700 g and an impurity concentration of $\sim 2. \cdot 10^{10}\, cm^{-3}$ which is one magnitude higher than in the PONaMa detectors. This higher impurity concentration prevents the development of low field regions inside the detectors (see fig. 5.21) but results in a higher operating voltage of 4 kV and 4.5 kV. The absence of low field regions leads to faster drift times and a stable A/E parameter for SSE in the detector bulk as shown in fig. 5.22 and fig. 5.23.

5.5 Conclusion

Ultra hight purity crystals can lead to extreme low electric fields in point contact detectors and thus decrease their pulse shape discrimination performance between single and multi side events as it is shown on the example of PONaMa II in this chapter. This detector has nearly no net impurities close to its top surface and thus no effective electric field. This leads to enormous increase of the charge cloud size and the above mentioned degraded PSD performance. PONaMa I having a large mass of ∼ 1000 g and a low bias voltage of 2 kV on the contrary shows a great PSD and overall performance. This means a careful selection of the ingot slices and the linked impurity profile enables the production of large ultra pure detectors with a flawless PSD performance.

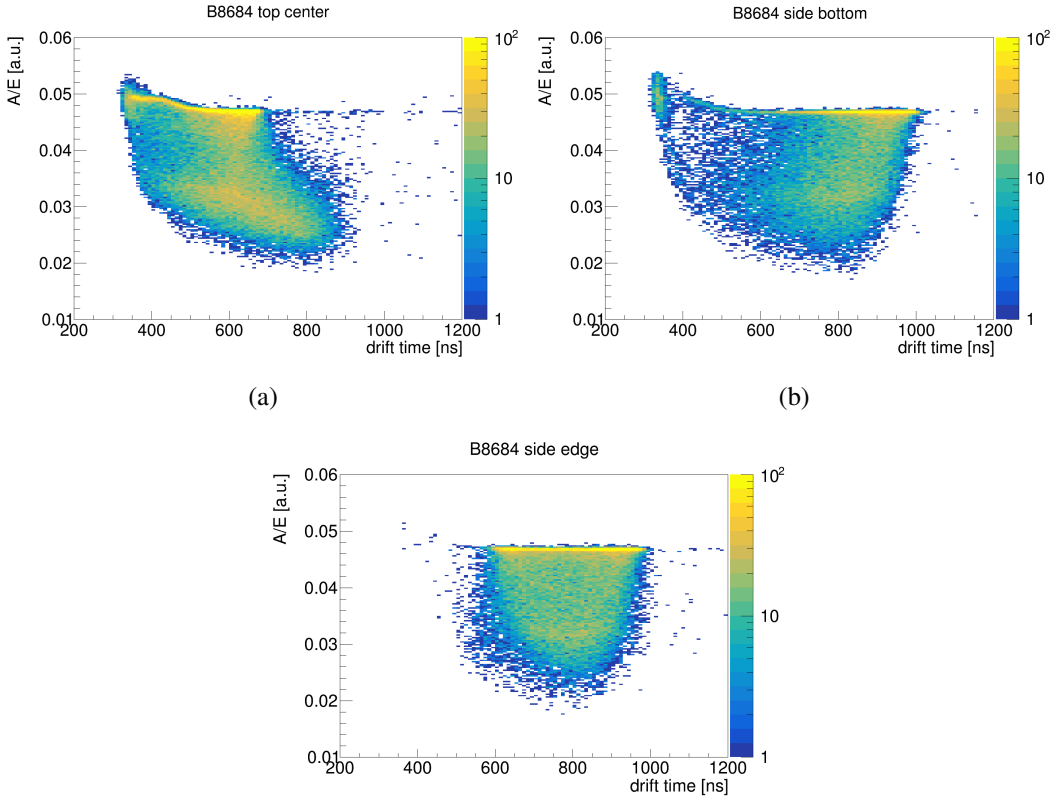

Fig. 5.22 B8684: A/E vs drift time distribution for the three collimator positions. (a) at the top center, (b) at the side bottom and (c) at the side edge position.

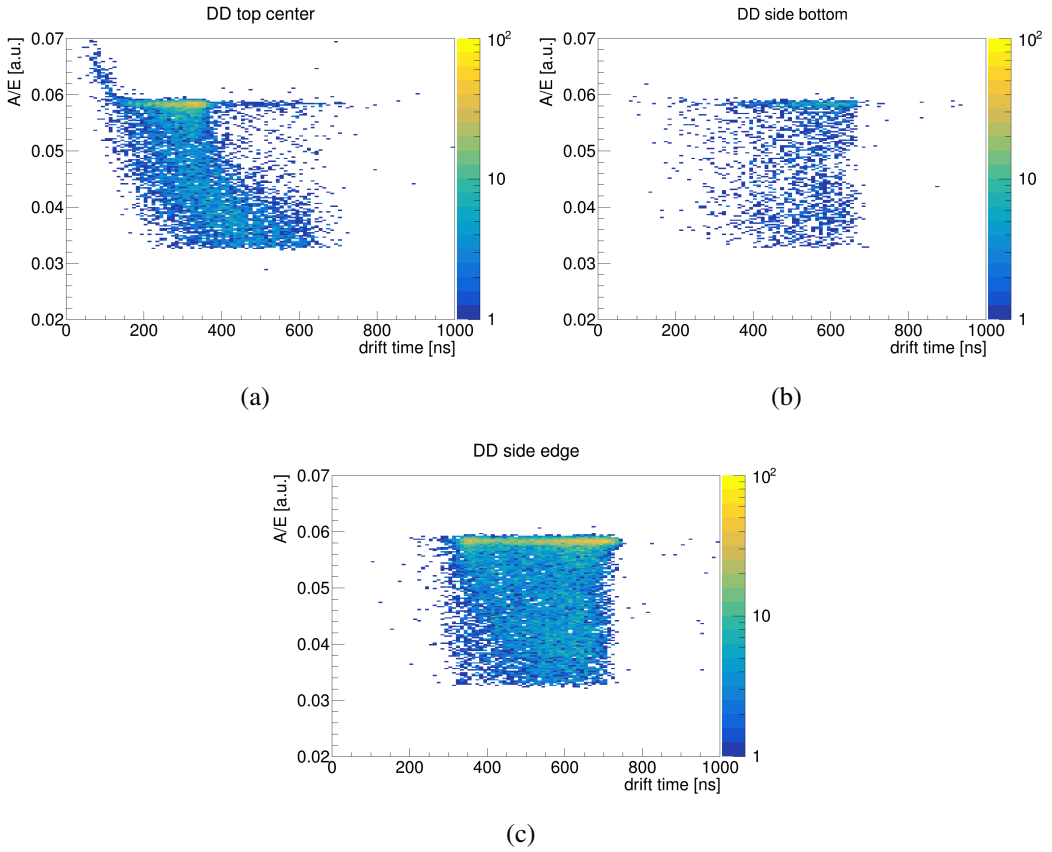

Fig. 5.23 DD: A/E vs drift time distribution for the three collimator positions. (a) at the top center, (b) at the side bottom and (c) at the side edge position.

The reduced PSD performance and the decrease of the A/E parameter towards the detector edges in PONaMa II is well reproduced by the `mjd_siggen` pulse shape simulation package by including a finite charge cloud size and its evolution with time. The good agreement between simulation and measurement shows that the physical processes in germanium point contact detectors are well understood and are modeled by the `mjd_siggen` simulation framework to a high precision.

Chapter 6

Conclusion and outlook

The use of germanium detectors with a point like geometry becomes more and more favorable in the astro-particle community since these detectors provide a superb energy resolution and background reduction techniques through pulse shape analysis. This work presented the characterization procedure and its results for the second batch of enriched germanium detectors used in the second phase of the GERDA experiment. Many of these detectors show a deviating pulse shape performance from the expectations gained through experience with prototype detectors made of depleted material. These deviations mostly relate to the spatial inhomogeneity of the A/E parameter used for the pulse shape discrimination between multi and single site events. Through comparison of simulated and measured pulses it was shown that the origin of this inhomogeneity most likely is caused by additional free charges located on the passivation layer inside the detector groove. These additional charges change the electric field and weighting potential in a way that the drift paths ending closer to the detector middle result in smaller A/E value. The oscillation of the A/E parameter along the crystal axis shows perfectly this effect. The faster drift in the <100> plane leads to closer impact point to the detector center and thus a smaller A/E value. This knowledge allows a reliable countermeasure namely the removing of the passivation layer on which the additional charges are trapped. The passivation layer is needed in detectors used in vacuum cryostats to reduce the leakage current and the linked electronic noise. In a liquid noble gas the leakage current can be reduced to a tolerable value without the use of a passivation layer [63][67]. Fortunately this is the case in GERDA since it uses liquid argon for cooling the detectors. The passivation layer was thus removed through etching in most BEGe detectors used in the GERDA experiment.

The second part of this work analyzed the influence of extremely low electric field caused by ultra pure germanium crystals. This was done with collimated surface scans and coincidence measurements of the first prototype detectors build by ORTEC for the Majorana experiment.

These measurements showed that an extreme low electric field leads to long charge drift times inside the crystal and an enormous expansion of the charge cloud followed by a decreased A/E value. This can worsen significantly the pulse shape performance of the detector. The results were compared with pulse shape simulations done with the `mjd_siggen` package. Charge cloud size evolution with time was previously implemented in the simulation package by David Radford. The parameters of the simulation were fine-tuned and evaluated in this work. The ability to reliably simulate the pulse shapes of germanium detectors enables the production of large volume detectors by selecting the needed impurity profile of the ingots and the right doping. PONaMa I is a good example that a large point contact detector can have a very low bias voltage and simultaneously a good pulse shape discrimination performance. To lower the background index by improving the pulse shape discrimination performance, it is important to fully understand the signal formation mechanism and measure the spatial dependence of the pulses. The common measurement methods like ^{241}Am scans only test the surface of the detectors and do not provide information on the bulk volume of the crystal. The coincident measurements presented in chapter 5 provide a statistical view on the bulk events through the drift time but not a direct spatial position.
A project was started in Tübingen to measure the direct interaction position of single site events and record the corresponding pulses. This was done in cooperation with the department of preclinical imaging and radiopharmacy since a small animal PET (Positron Emission Tomography) scanner was used to localize the interaction point inside the crystal. The full description of this project can be found in the thesis of Christopher Schmitt [68].
The full information on the spatial dependence of pulses would allow to further improve the the pulse shape simulations and also enable the creation of a pulse shape library. Such a library could be used to improve analysis methods based on machine learning algorithms and further increase the background suppression.

List of figures

1.1 Mass parabola and decay scheme of nuclei with A=76 2
1.2 Feynman diagram for $2\nu\beta\beta$ and $0\nu\beta\beta$ 2
1.3 Nuclear matrix elements for various $0\nu\beta\beta$ candidates 4
1.4 Effective Majorana neutrino mass versus lightest neutrino mass 5
1.5 Laboratory Nazionale del Gran Sasso (LNGS) 7
1.6 GERDA schematic drawing 7
1.7 Germanium detector strings inside the nylon shrouds 8
1.8 Liquid argon veto 9
1.9 Water Cherenkov muon veto 9
1.10 Liquid argon veto efficiency 10
1.11 PSD cut efficiency 11

2.1 Average path length of electrons 15
2.2 Minimal enclosing sphere for a electron track in germanium 15
2.3 Photon mass attenuation coefficient μ for germanium 17
2.4 Simulated spectrum for the 2.6 MeV line of ^{208}Tl 18
2.5 Signal formation in a detector 21
2.6 HPGe detectors geometries 23
2.7 Simulated electric and weighting potential for a BEGe detector 24
2.8 Example pulse shape for different event classes 25
2.9 A/E vs energy scatter plot for a BEGe 26
2.10 A/E classifier for DEP and SEP ROI 26

3.1 Example electric potential simulation for a BEGe detector 28
3.2 Germanium crystal structure 29
3.3 Charge carrier velocities along different crystal axis 30

4.1 Photograph of the ^{enr}Ge. 34
4.2 Photographs of a germanium crystal 34

4.3 Cylindrical and cone-shaped crystal slices 34
4.4 Layout of the HADES facility 35
4.5 Design of the automated scanning apparatus 36
4.6 Catequil linear scans 38
4.7 59.5 keV peak in the ^{241}Am spectrum 38
4.8 Catequil peak position 59.5 keV 42
4.9 Diana peak position 59.5 keV 43
4.10 Diana event rate in 59.5 keV ROI 44
4.11 Average FWHM at 59.5 keV for the second batch of enriched detectors . . . 45
4.12 Raw auxiliary waveform 45
4.13 Rise time distribution for Catequil 46
4.14 Catequil 1-90% rise time 47
4.15 Centaur 1-90% rise time 49
4.16 Catequil: A/E @ 59.5 keV ROI at r=30 mm and 0° 50
4.17 Caesar A/E top and lateral scan 51
4.18 A/E distribution for the DEP of Caesar and Ge9 a detector made made depleted Ge 52
4.19 Catequil A/E top and lateral scan 53
4.20 Catequil A/E distribution vs radius 54
4.21 Centaur A/E top and lateral scan 55
4.22 ^{208}Tl DEP A/E distribution for the DEP of Centaur and Bhima 56
4.23 Standard deviation of the centroid of the A/E distribution in the circular scans for the second batch of enriched detectors 56
4.24 Average FWHM of the A/E distribution in the circular scans for the second batch of enriched detectors 57
4.25 Briseis and Bellerophons A/E top scan 58
4.26 FWHM of the A/E distribution for the DEP events vs standard deviation of the centroid of the A/E for circular scans 59
4.27 FWHM of the A/E distribution for the DEP events vs maximum difference between the centroids of the A/E distribution for two points in the circular scans 60
4.28 Detector and collimator geometry used in MaGe 61
4.29 Simulated BEGe pulse with white noise 62
4.30 Catequil 1-90% rise time, simulated pulses 63
4.31 Catequil A/E, simulated pulses 64
4.32 Simulated drift paths for the Catequil detector 65

4.33 Measured and simulated A/E distribution of the DEP events of ^{208}Tl in the Catequil detector 66
4.34 Bes A/E top and lateral scan 67
4.35 A/E distribution for collimated ^{228}Th measurements on Bes 68

5.1 Simulated electric and weighting potential in PONaMa I 73
5.2 Simulated electric and weighting potential in PONaMa II 75
5.3 ^{241}Am scanning setup at LBNL 76
5.4 Example pulse of the PONoMa I detector illuminated with a collimated ^{241}Am source. 76
5.5 59.5 keV peak in the ^{241}Am spectrum of PONaMa I 77
5.6 PONaMA I/II: Counts in linear scans 77
5.7 PONaMA I/II: A/E distribution for r=0,15,30m̊m 78
5.8 PONaMA I/II A/E in linear scans 78
5.9 PONaMA II sample wave forms for r=0,15,30m̊m 79
5.10 PONaMA I/II: Rise time in linear scans 80
5.11 Drift time measurement setup at LBNL 81
5.12 Positions for the coincidence measurements 81
5.13 Drift time measurement sample waveform 83
5.14 Scatter plot of the detected energy in the PONaMa I and the NaI detector . . 83
5.15 PONaMA I/II: Drift time distribution 85
5.16 PONaMA I/II: 1-90% rise time vs drift time distribution 86
5.17 PONaMA I/II: 1-90% rise time distribution 87
5.18 PONaMA I/II: A/E distribution 89
5.19 PONaMA I/II: A/E vs drift time distribution 90
5.20 PONaMA II: A/E vs drift time simulated distribution 91
5.21 Simulated electric potential and field in B8684 92
5.22 [BEGe B8684: A/E vs drift time distribution 93
5.23 [BEGe DD: A/E vs drift time distribution 94

A.1 Summery 1-90% rise time top scans 114
A.2 Summery 1-90% rise time lateral scans 118
A.3 Summery AE top circular scans 122
A.4 Summery A/E lateral scans 126

List of tables

4.1 Top scan summary 39
4.2 Lateral scan summary 40
4.3 Summary of the simulated drift paths for the Catequil detector 65

5.1 Summary of the general specifications and performance parameters of PONaMa I and II 72

References

[1] The GERDA Collaboration. Background-free search for neutrinoless double-β decay of ^{76}Ge with GERDA. *Nature*, 2017/04/06/ print:544.

[2] David Radford. Radware Sofware. http://radware.phy.ornl.gov/MJ/mjd_siggen/. Accessed: 2017-06-24.

[3] A. S. Barabash. Precise half-life values for two neutrino double beta decay. *Phys. Rev.*, C81:035501, 2010.

[4] Ettore Majorana. Teoria simmetrica dell'elettrone e del positrone. *Il Nuovo Cimento (1924-1942)*, 14(4):171, 2008.

[5] Q. R. Ahmad et al. Measurement of the rate of $\nu_e + d \rightarrow p + p + e^-$ interactions produced by ^8B solar neutrinos at the Sudbury Neutrino Observatory. *Phys. Rev. Lett.*, 87:071301, 2001.

[6] S. Fukuda et al. The Super-Kamiokande detector. *Nuclear Instruments and Methods in Physics Research Section A: Accelerators, Spectrometers, Detectors and Associated Equipment*, 501(2–3):418 – 462, 2003.

[7] Y. Abe et al. Improved measurements of the neutrino mixing angle θ_{13} with the Double Chooz detector. *JHEP*, 10:086, 2014.

[8] Heinrich Päs and Werner Rodejohann. Neutrinoless Double Beta Decay. *New J. Phys.*, 17(11):115010, 2015.

[9] Bernhard Schwingenheuer. Status and prospects of searches for neutrinoless double beta decay. *Annalen Phys.*, 525:269–280, 2013.

[10] J. Menendez. PhD thesis.

[11] Frank T. Avignone, III, Steven R. Elliott, and Jonathan Engel. Double Beta Decay, Majorana Neutrinos, and Neutrino Mass. *Rev. Mod. Phys.*, 80:481–516, 2008.

[12] A. Gando et al. Search for Majorana Neutrinos near the Inverted Mass Hierarchy Region with KamLAND-Zen. *Phys. Rev. Lett.*, 117(8):082503, 2016.

[13] Jonathan Engel and Javier Menéndez. Status and Future of Nuclear Matrix Elements for Neutrinoless Double-Beta Decay: A Review. *Rept. Prog. Phys.*, 80(4):046301, 2017.

[14] Manfred Lindner, Alexander Merle, and Werner Rodejohann. Improved limit on θ_{13} and implications for neutrino masses in neutrino-less double beta decay and cosmology. *Phys. Rev.*, D73:053005, 2006.

[15] J. J. Gomez-Cadenas, J. Martin-Albo, M. Sorel, P. Ferrario, F. Monrabal, J. Munoz-Vidal, P. Novella, and A. Poves. Sense and sensitivity of double beta decay experiments. *JCAP*, 1106:007, 2011.

[16] GERDA homepage. https://www.mpi-hd.mpg.de/gerda/internal/index.html.

[17] M. Agostini et al. Production, characterization and operation of ^{76}Ge enriched BEGe detectors in GERDA. *Eur. Phys. J.*, C75(2):39, 2015.

[18] H.V Klapdor-Kleingrothaus, I.V Krivosheina, A Dietz, and O Chkvorets. Search for neutrinoless double beta decay with enriched ^{76}Ge in Gran Sasso 1990–2003. *Physics Letters B*, 586(3–4):198 – 212, 2004.

[19] C. E. Aalseth et al. The IGEX Ge-76 neutrinoless double beta decay experiment: Prospects for next generation experiments. *Phys. Rev.*, D65:092007, 2002.

[20] J. Janicskó Csáthy, T. Bode, J. Kratz, S. Schönert, and Ch. Wiesinger. Optical fiber read-out for liquid argon scintillation light. *arXiv:1606.04254*, 2016.

[21] K. Freund et al. The performance of the Muon Veto of the GERDA experiment. *The European Physical Journal C*, 76(5):298, 2016.

[22] Canberra Industries Inc., 107 Union Valley Rd, Oak Ridge, TN, USA. http://www.canberra.com/. Accessed: 2016-01-12.

[23] ORTEC/AMETEK Inc., 801 South Illinois Avenue,Oak Ridge, TN, USA. http://www.ortec-online.com//. Accessed: 2016-06-08.

[24] P. N. Luke, F. S. Goulding, N. W. Madden, and R. H. Pehl. Low capacitance large volume shaped-field germanium detector. *IEEE Transactions on Nuclear Science*, 36(1):926–930, Feb 1989.

[25] Glenn Frederick Knoll. *Radiation detection and measurement; 4. ed.* Wiley, Hoboken, NJ, 2010.

[26] William R. Leo. *Techniques for nuclear and particle physics experiments : a how-to approach; 2nd rev. ed*. Springer, Berlin ;New York, 1994.

[27] M. J. Berger et al. ESTAR : Stopping-Power and Range Tables for Electrons, Protons and Helium Ions. http://www.nist.gov/pml/data/star/index.cfm.

[28] M. Boswell et al. Mage-a geant4-based monte carlo application framework for low-background germanium experiments. *IEEE Transactions on Nuclear Science*, 58(3):1212–1220, June 2011.

[29] Fast computation of the smallest enclosing ball of a point set, in low or moderately high dimensions. https://github.com/hbf/miniball.

[30] M. J. Berger et al. XCOM : Photon Cross Sections Database. http://www.nist.gov/pml/data/xcom/index.cfm.

[31] Helmuth Spieler. *Semiconductor detector systems*, volume 12 of *Series on semiconductor science and technology*. Oxford University Press, Oxford, 2005.

[32] Christian J. Schmidt. Lecture on particle detectors and electronic readout, 1938.

[33] W. Shockley. Currents to Conductors Induced by a Moving Point Charge. *Journal of Applied Physics*, 9(10):635–636, 1938.

[34] S. Ramo. Currents induced by electron motion. *Proceedings of the IRE*, 27(9):584–585, Sept 1939.

[35] Zhong He. Review of the shockley–ramo theorem and its application in semiconductor gamma-ray detectors. *Nuclear Instruments and Methods in Physics Research Section A: Accelerators, Spectrometers, Detectors and Associated Equipment*, 463(1–2):250 – 267, 2001.

[36] Raphael Falkenstein. *BEGe characterization for the* GERDA *experiment*. PhD thesis, Eberhard–Karls–Universität Tübingen, Germany, to be published.

[37] S. Mertens et al. *MAJORANA* Collaboration's Experience with Germanium Detectors. *J. Phys. Conf. Ser.*, 606(1):012005, 2015.

[38] M. Agostini et al. Pulse shape discrimination for GERDA Phase I data. *Eur. Phys. J.*, C73(10):2583, 2013.

[39] Dusan Budjas, Marik Barnabe Heider, Oleg Chkvorets, Nikita Khanbekov, and Stefan Schonert. Pulse shape discrimination studies with a Broad-Energy Germanium detector for signal identification and background suppression in the GERDA double beta decay experiment. *JINST*, 4:P10007, 2009.

[40] Marco Salathe. *Study on modified point contact germanium detectors for low background applications*. PhD thesis, Ruprecht–Karls–Universität Heidelberg, Germany, 2015.

[41] Charles Kittel. *Introduction to Solid State Physics*. John Wiley & Sons, Inc., New York, 6th edition, 1986.

[42] N.W. Ashcroft and N.D. Mermin. *Solid State Physics*. Saunders College, Philadelphia, 1976.

[43] Motoichi Shibuya. Hot electron problem in semiconductors with spheroidal energy surfaces. *Phys. Rev.*, 99:1189–1191, Aug 1955.

[44] W. Sasaki and M. Shibuya. Experimental evidence of the anisotropy of hot electrons in n-type germanium. *Journal of the Physical Society of Japan*, 11(11):1202–1203, 1956.

[45] M.Ali Omar and Lino Reggiani. Drift velocity and diffusivity of hot carriers in germanium: Model calculations. *Solid-State Electronics*, 30(12):1351 – 1354, 1987.

[46] L Mihailescu, W Gast, R.M Lieder, H Brands, and H Jäger. The influence of anisotropic electron drift velocity on the signal shapes of closed-end HPGe detectors. *Nuclear Instruments and Methods in Physics Research Section A: Accelerators, Spectrometers, Detectors and Associated Equipment*, 447(3):350 – 360, 2000.

[47] I-Yang Lee. GRETINA technical note: Electron and hole drift velocity in Ge. unpublished report.

[48] D. Weisshaar et al. The performance of the γ-ray tracking array {GRETINA} for γ-ray spectroscopy with fast beams of rare isotopes. *Nuclear Instruments and Methods in Physics Research, A*, 847:187 – 198, 2017.

[49] Bart Bruyneel, Peter Reiter, and Gheorghe Pascovici. Characterization of large volume HPGe detectors. Part II: Experimental results. *Nuclear Instruments and Methods in Physics Research Section A: Accelerators, Spectrometers, Detectors and Associated Equipment*, 569(3):774 – 789, 2006.

[50] Characterization of large volume HPGe detectors. Part I: Electron and hole mobility parameterization.

[51] Emilio Gatti, Antonio Longoni, Pavel Rehak, and Marco Sampietro. Dynamics of electrons in drift detectors. *Nuclear Instruments and Methods in Physics Research Section A: Accelerators, Spectrometers, Detectors and Associated Equipment*, 253(3):393 – 399, 1987.

[52] C. Jacoboni, F. Nava, C. Canali, and G. Ottaviani. Electron drift velocity and diffusivity in germanium. *Phys. Rev. B*, 24:1014–1026, Jul 1981.

[53] Canberra Semiconductor N.V., Lammerdries 25, 2250 Olen, Belgium. http://www.canberra.com/. Accessed: 2016-01-12.

[54] Joint Stock Company "Production Association Electrochemical Plant", Pervaya Promyshlennaya 1, 663690 Zelenogorsk, Russia. http://www.ecp.ru/eng. Accessed: 2016-01-12.

[55] PPM Pure Metals GmbH. http://www.ppmpuremetals.de/. Accessed: 2016-04-08.

[56] HADES Underground Research Laboratary. http://science.sckcen.be/en/Facilities/HADES. Accessed: 2016-01-12.

[57] E. Andreotti et al. HEROICA: an Underground Facility for the Fast Screening of Germanium Detectors. *JINST*, 8:P06012, 2013.

[58] E. Andreotti et al. Status of underground radioactivity measurements in HADES, in Proceedings of the 3rd International Conference on Current Problems in Nuclear Physics and Atomic Energy, Kyev Ukrain, P601. 2011.

[59] Victoria Wagner. Investigation of Pulse Shape Performance of the First GERDA Phase II Detectors, 2012.

[60] Hans R. Bilger. Fano Factor in Germanium at 77°K. *Phys. Rev.*, 163:238–253, Nov 1967.

[61] N. Strokan, V. Ajdačić, and B. Lalović. Measurements of the fano factor in germanium. *Nuclear Instruments and Methods*, 94(1):147–149, 1971.

[62] Heng-Ye Liao. *Developments of pulse shape discrimination methods for the BEGe detectors*. PhD thesis, Ludwig–Maximilians–Universität München, Germany, 2016.

[63] Marik Barnabé Heider. *Performance and stability testsof bare high purity germanium detectors in liquid argon for the* GERDA *experiment*. PhD thesis, Ruprecht–Karls–Universität Heidelberg, Germany, 20209.

[64] S. Mertnes et al. Pulse Shapes in High Purity Germanium Point Contact Detectors with Low Net Impurity Concentration. *Nuclear Inst. and Methods in Physics Research, A*, to be published.

[65] Object-oriented Real-time Control Aquisition. http://orca.physics.unc.edu/Orca_Help/Home.html. Accessed: 2016-09-14.

[66] R. D. Martin et al. Determining the Drift Time of Charge Carriers in P-Type Point-Contact HPGe Detectors. *Nuclear Inst. and Methods in Physics Research, A*, A678:98–104, 2012.

[67] M. Barnabé Heider, D. Budjáš, K. Gusev, and S. Schönert. Operation and performance of a bare broad-energy germanium detector in liquid argon. *Journal of Instrumentation*, 5(10):P10007, 2010.

[68] Christopher Schmitt. *Measurement of the spatial location of double escape events in a germanium detector using a PET scanner*. PhD thesis, Eberhard–Karls–Universität Tübingen, Germany, to be published.

Appendix A

Appendix

Circular scans

top scans 1-90 % rise time

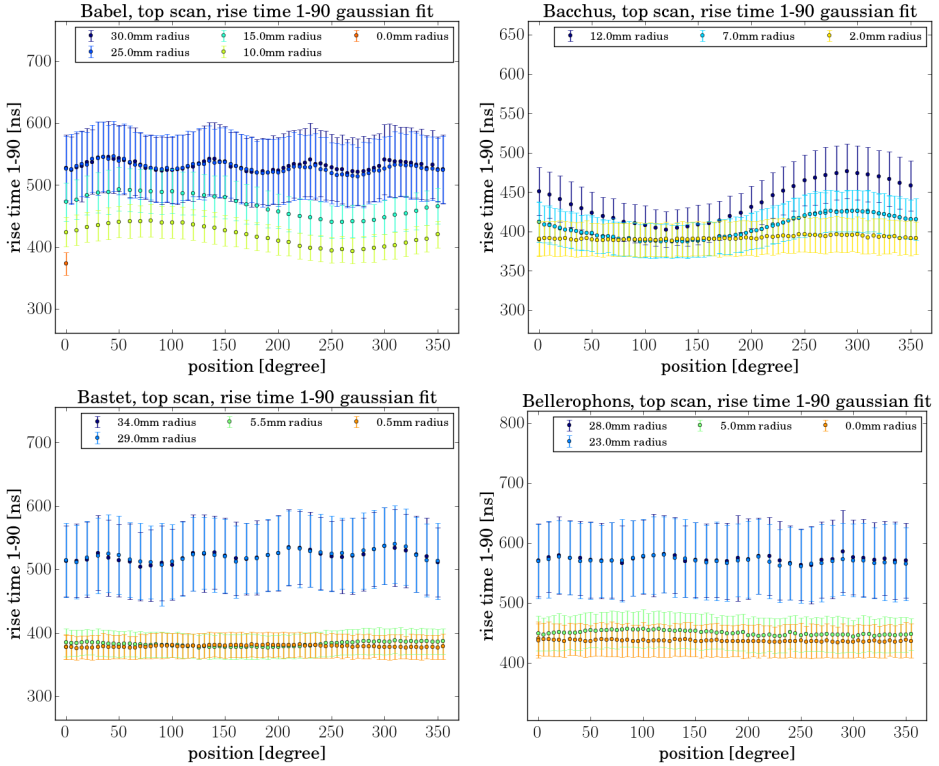

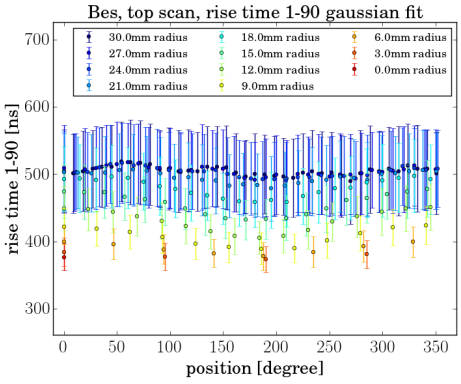
Bes, top scan, rise time 1-90 gaussian fit
30.0mm radius
27.0mm radius
24.0mm radius
21.0mm radius
18.0mm radius
15.0mm radius
12.0mm radius
9.0mm radius
6.0mm radius
3.0mm radius
0.0mm radius
rise time 1-90 [ns]
position [degree]

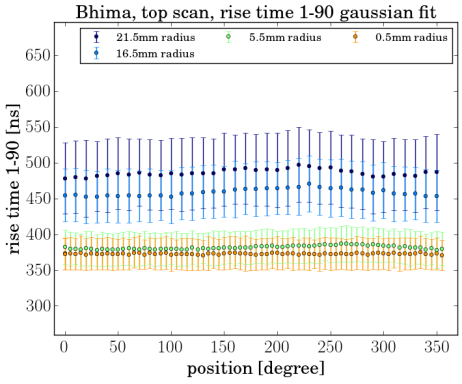
Bhima, top scan, rise time 1-90 gaussian fit
21.5mm radius
16.5mm radius
5.5mm radius
0.5mm radius
rise time 1-90 [ns]
position [degree]

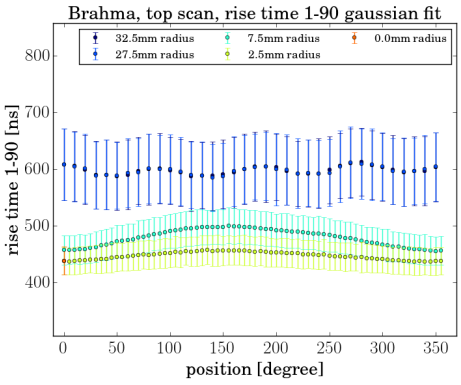
Brahma, top scan, rise time 1-90 gaussian fit
32.5mm radius
27.5mm radius
7.5mm radius
2.5mm radius
0.0mm radius
rise time 1-90 [ns]
position [degree]

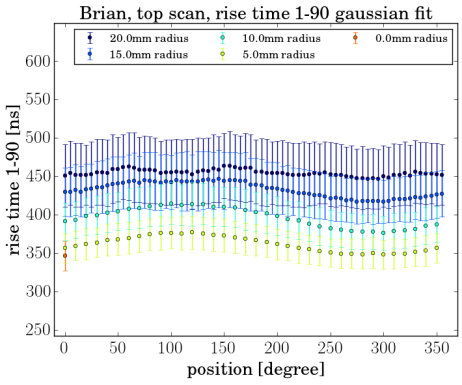
Brian, top scan, rise time 1-90 gaussian fit
20.0mm radius
15.0mm radius
10.0mm radius
5.0mm radius
0.0mm radius
rise time 1-90 [ns]
position [degree]

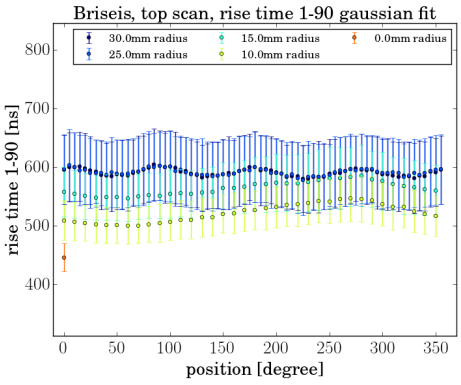
Briseis, top scan, rise time 1-90 gaussian fit
30.0mm radius
25.0mm radius
15.0mm radius
10.0mm radius
0.0mm radius
rise time 1-90 [ns]
position [degree]

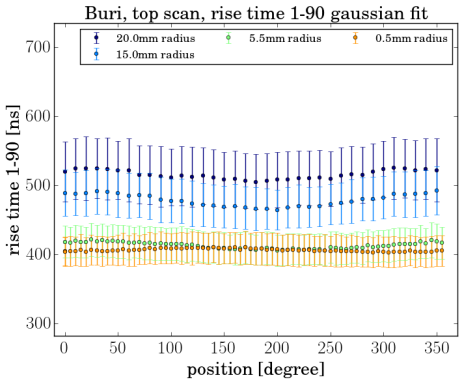
Buri, top scan, rise time 1-90 gaussian fit
20.0mm radius
15.0mm radius
5.5mm radius
0.5mm radius
rise time 1-90 [ns]
position [degree]

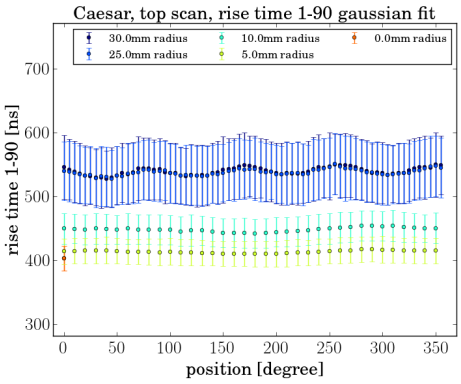
Caesar, top scan, rise time 1-90 gaussian fit
30.0mm radius
25.0mm radius
10.0mm radius
5.0mm radius
0.0mm radius
rise time 1-90 [ns]
position [degree]

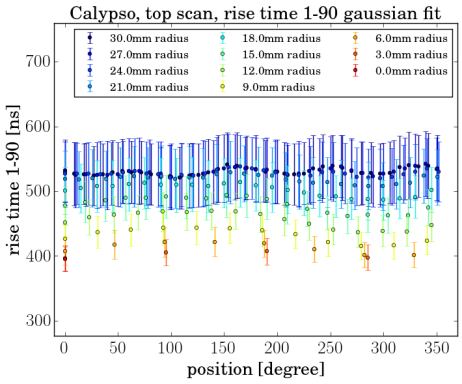
Calypso, top scan, rise time 1-90 gaussian fit
30.0mm radius
27.0mm radius
24.0mm radius
21.0mm radius
18.0mm radius
15.0mm radius
12.0mm radius
9.0mm radius
6.0mm radius
3.0mm radius
0.0mm radius
rise time 1-90 [ns]
position [degree]

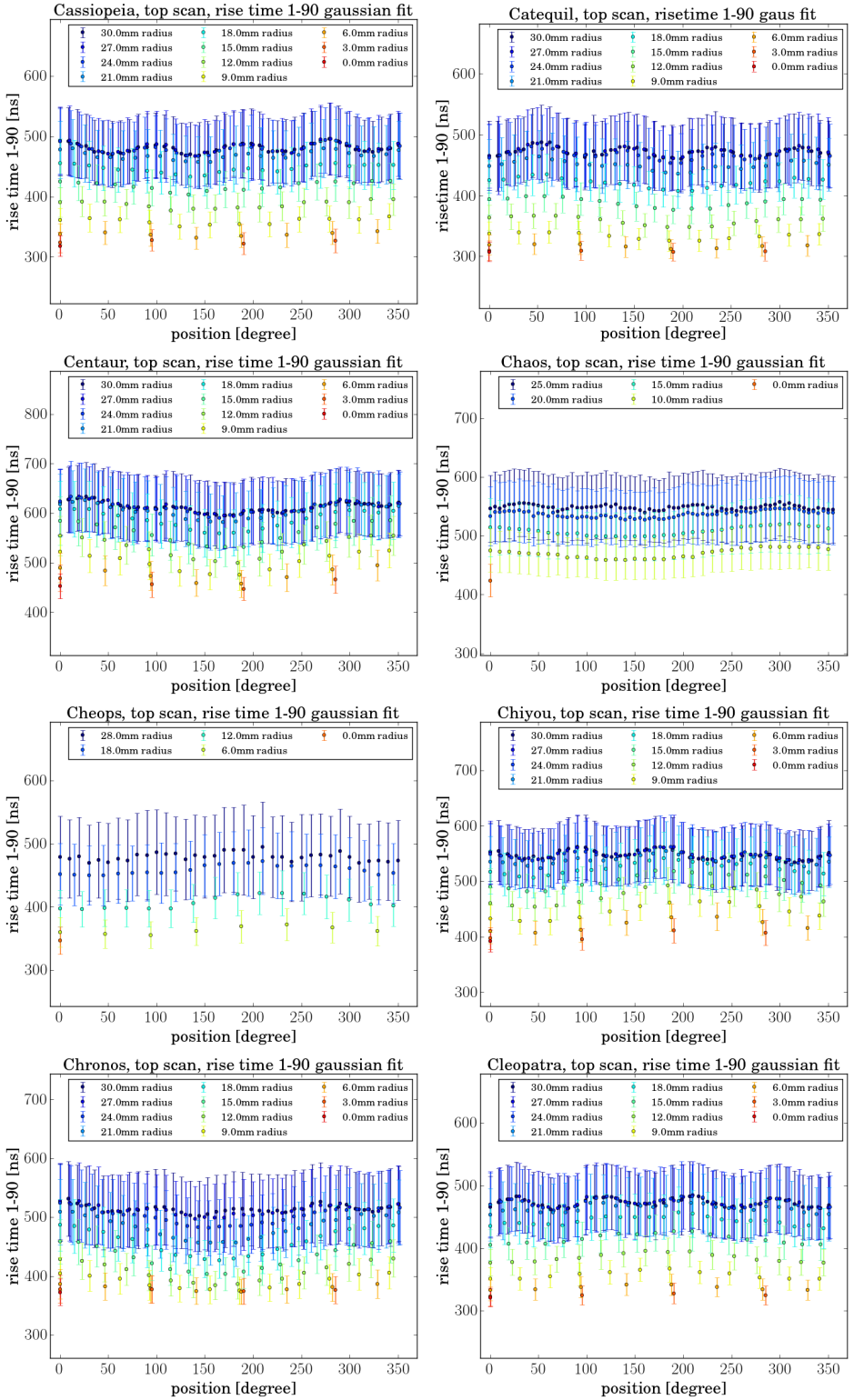
Cassiopeia, top scan, rise time 1-90 gaussian fit
30.0mm radius
27.0mm radius
24.0mm radius
21.0mm radius
18.0mm radius
15.0mm radius
12.0mm radius
9.0mm radius
6.0mm radius
3.0mm radius
0.0mm radius
rise time 1-90 [ns]
position [degree]
Catequil, top scan, risetime 1-90 gaus fit
risetime 1-90 [ns]
position [degree]
Centaur, top scan, rise time 1-90 gaussian fit
rise time 1-90 [ns]
position [degree]
Chaos, top scan, rise time 1-90 gaussian fit
25.0mm radius
20.0mm radius
15.0mm radius
10.0mm radius
0.0mm radius
rise time 1-90 [ns]
position [degree]
Cheops, top scan, rise time 1-90 gaussian fit
28.0mm radius
18.0mm radius
12.0mm radius
6.0mm radius
0.0mm radius
rise time 1-90 [ns]
position [degree]
Chiyou, top scan, rise time 1-90 gaussian fit
rise time 1-90 [ns]
position [degree]
Chronos, top scan, rise time 1-90 gaussian fit
rise time 1-90 [ns]
position [degree]
Cleopatra, top scan, rise time 1-90 gaussian fit
rise time 1-90 [ns]
position [degree]

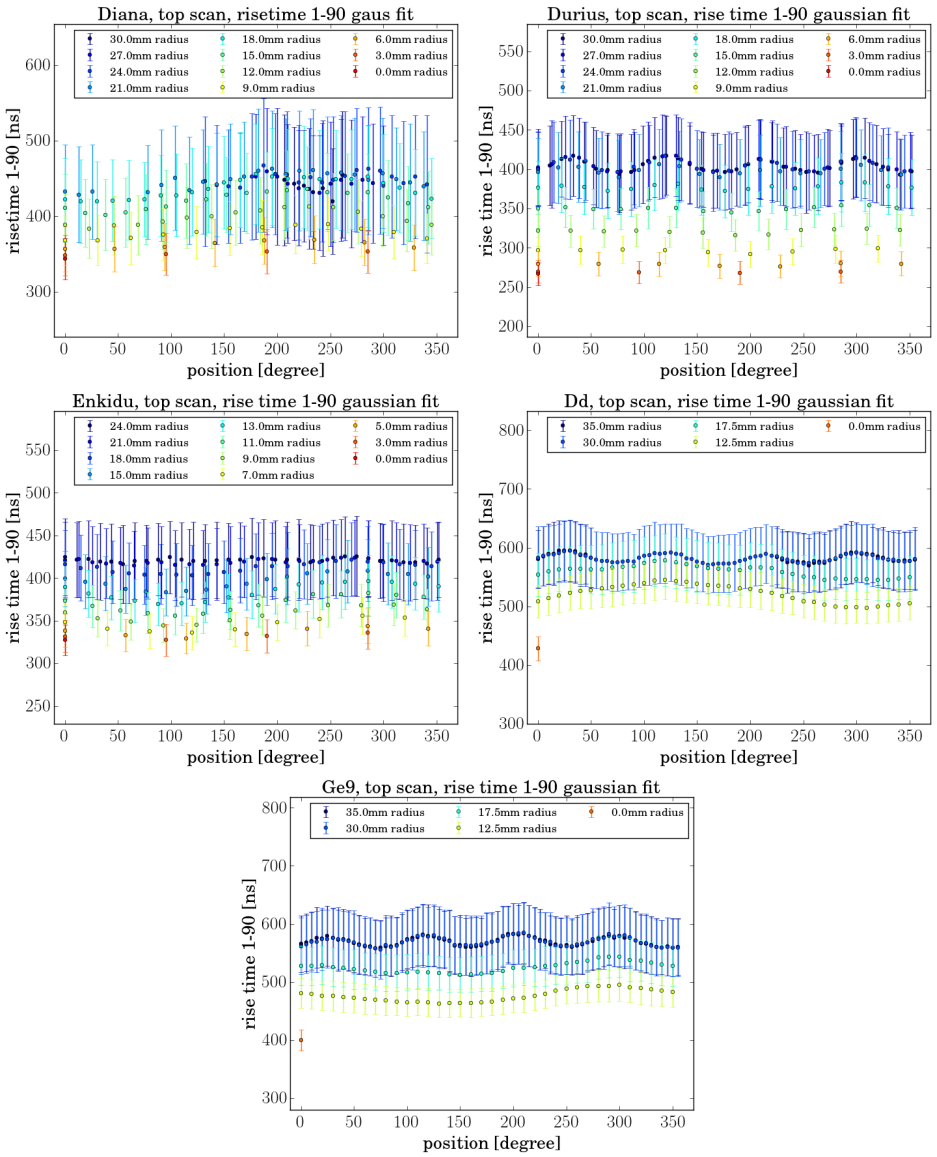

Fig. A.1 Summery 1-90% rise time for the top circular scans. Each point in the graphs represents the mean of the Gaussian fitted to the rise time distribution in the 59.5 keV ROI with the sigma as error bars. Different radii are plotted in different colors. The middle point is plotted as r=0 and ϕ =0^0.

lateral scans 1-90 % rise time

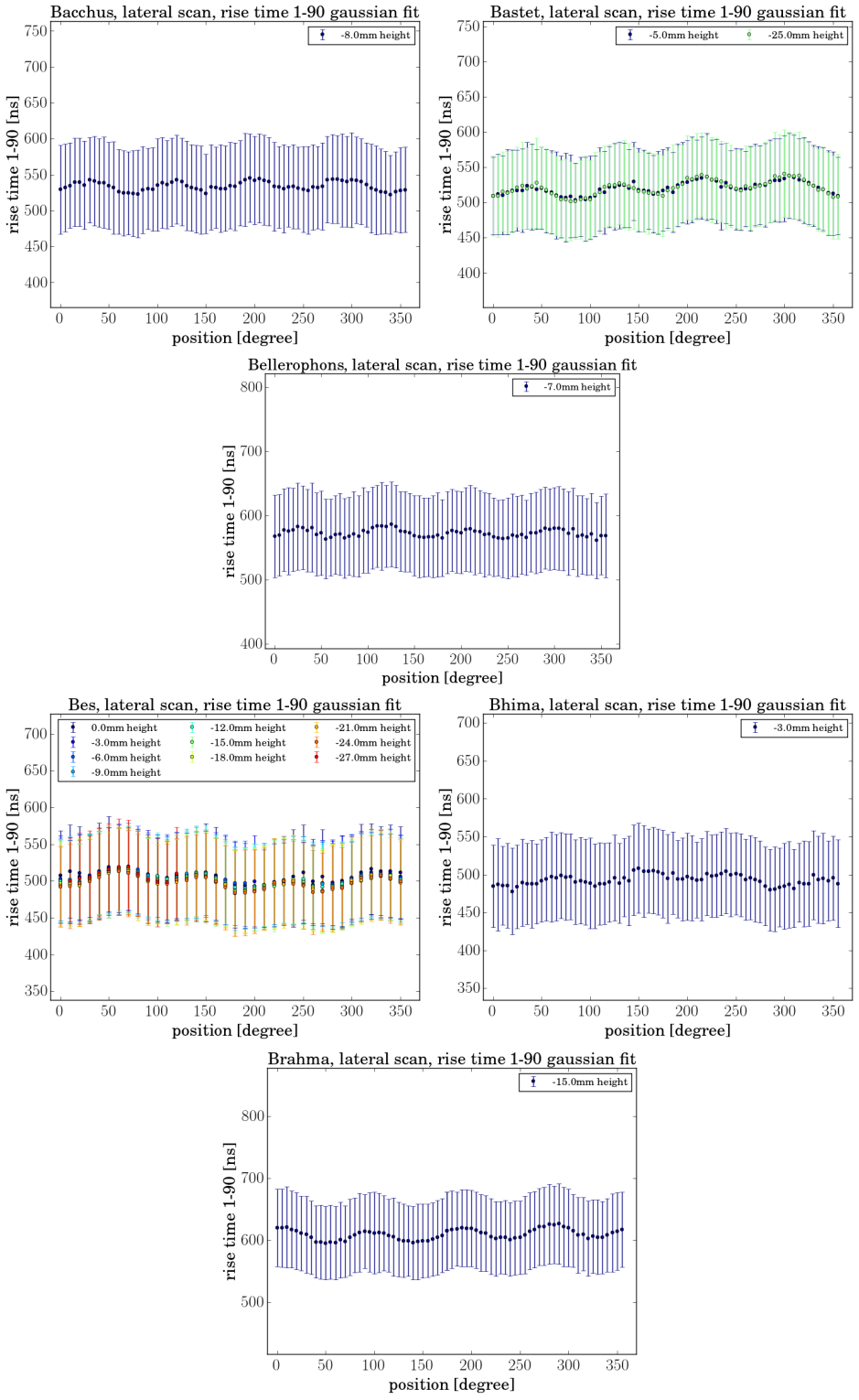

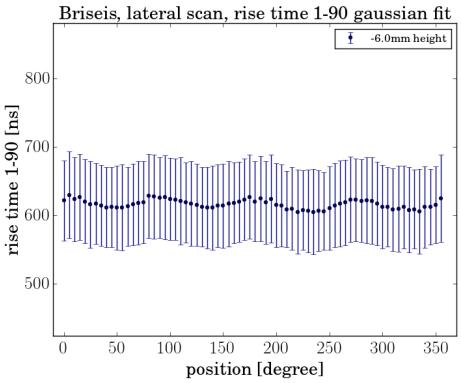
Briseis, lateral scan, rise time 1-90 gaussian fit
-6.0mm height
rise time 1-90 [ns]
position [degree]

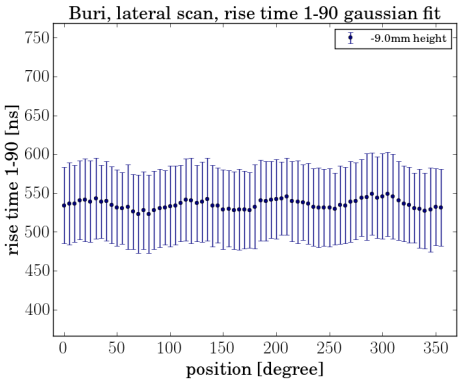
Buri, lateral scan, rise time 1-90 gaussian fit
-9.0mm height
rise time 1-90 [ns]
position [degree]

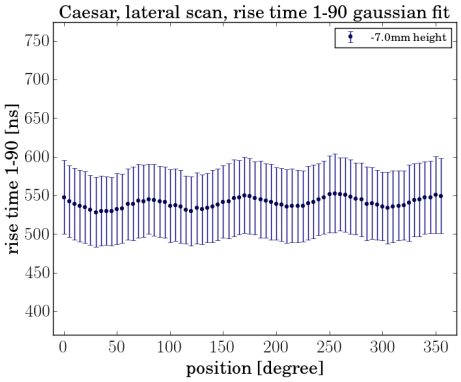
Caesar, lateral scan, rise time 1-90 gaussian fit
-7.0mm height
rise time 1-90 [ns]
position [degree]

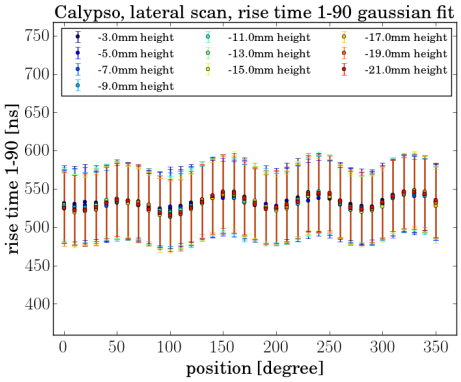
Calypso, lateral scan, rise time 1-90 gaussian fit
-3.0mm height
-5.0mm height
-7.0mm height
-9.0mm height
-11.0mm height
-13.0mm height
-15.0mm height
-17.0mm height
-19.0mm height
-21.0mm height
rise time 1-90 [ns]
position [degree]

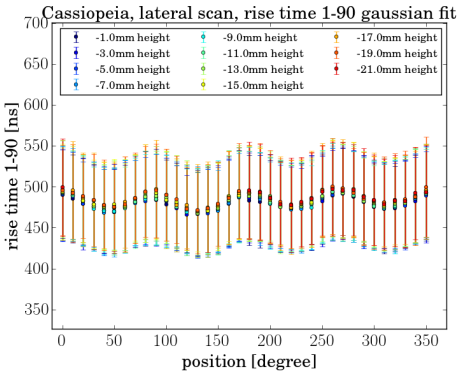
Cassiopeia, lateral scan, rise time 1-90 gaussian fit
-1.0mm height
-3.0mm height
-5.0mm height
-7.0mm height
-9.0mm height
-11.0mm height
-13.0mm height
-15.0mm height
-17.0mm height
-19.0mm height
-21.0mm height
rise time 1-90 [ns]
position [degree]

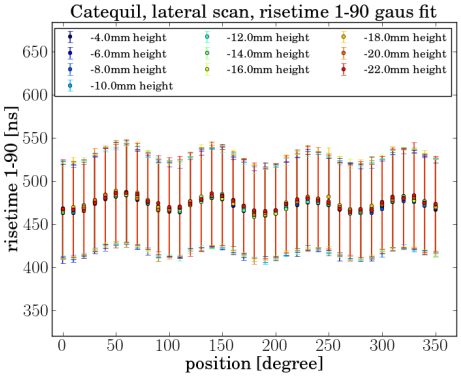
Catequil, lateral scan, risetime 1-90 gaus fit
-4.0mm height
-6.0mm height
-8.0mm height
-10.0mm height
-12.0mm height
-14.0mm height
-16.0mm height
-18.0mm height
-20.0mm height
-22.0mm height
risetime 1-90 [ns]
position [degree]

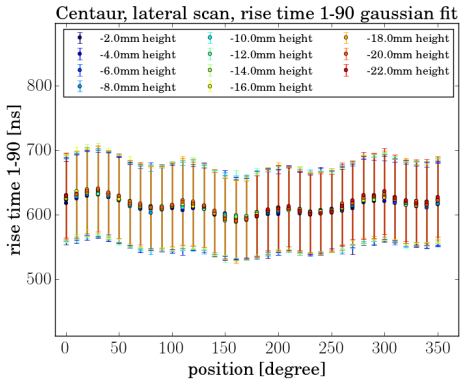
Centaur, lateral scan, rise time 1-90 gaussian fit
-2.0mm height
-4.0mm height
-6.0mm height
-8.0mm height
-10.0mm height
-12.0mm height
-14.0mm height
-16.0mm height
-18.0mm height
-20.0mm height
-22.0mm height
rise time 1-90 [ns]
position [degree]

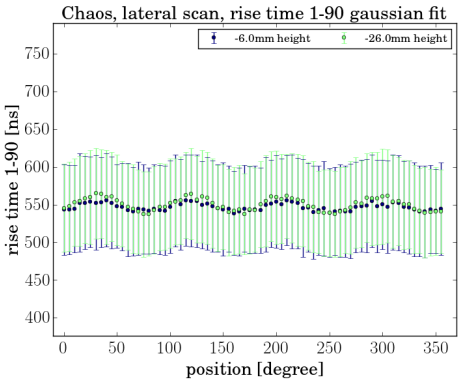
Chaos, lateral scan, rise time 1-90 gaussian fit
-6.0mm height
-26.0mm height
rise time 1-90 [ns]
position [degree]

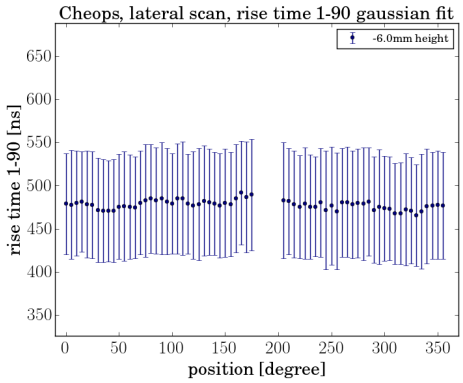
Cheops, lateral scan, rise time 1-90 gaussian fit
-6.0mm height
rise time 1-90 [ns]
position [degree]

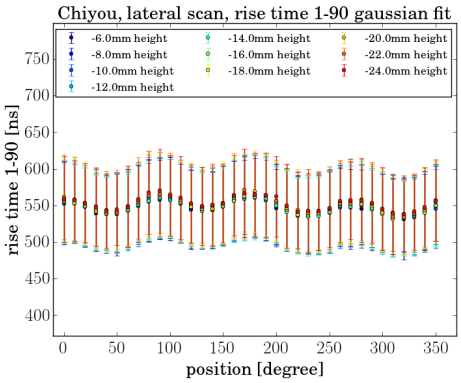
Chiyou, lateral scan, rise time 1-90 gaussian fit
-6.0mm height
-8.0mm height
-10.0mm height
-12.0mm height
-14.0mm height
-16.0mm height
-18.0mm height
-20.0mm height
-22.0mm height
-24.0mm height
rise time 1-90 [ns]
position [degree]

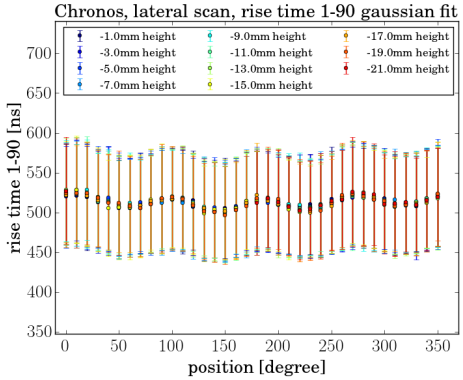
Chronos, lateral scan, rise time 1-90 gaussian fit
-1.0mm height
-3.0mm height
-5.0mm height
-7.0mm height
-9.0mm height
-11.0mm height
-13.0mm height
-15.0mm height
-17.0mm height
-19.0mm height
-21.0mm height
rise time 1-90 [ns]
position [degree]

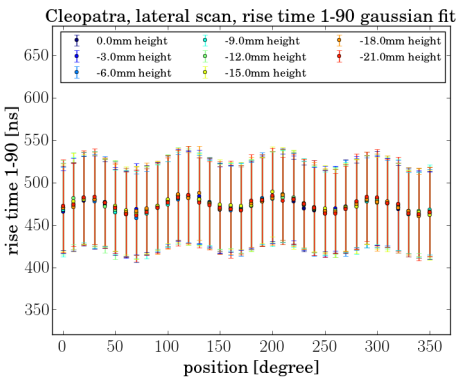
Cleopatra, lateral scan, rise time 1-90 gaussian fit
0.0mm height
-3.0mm height
-6.0mm height
-9.0mm height
-12.0mm height
-15.0mm height
-18.0mm height
-21.0mm height
rise time 1-90 [ns]
position [degree]

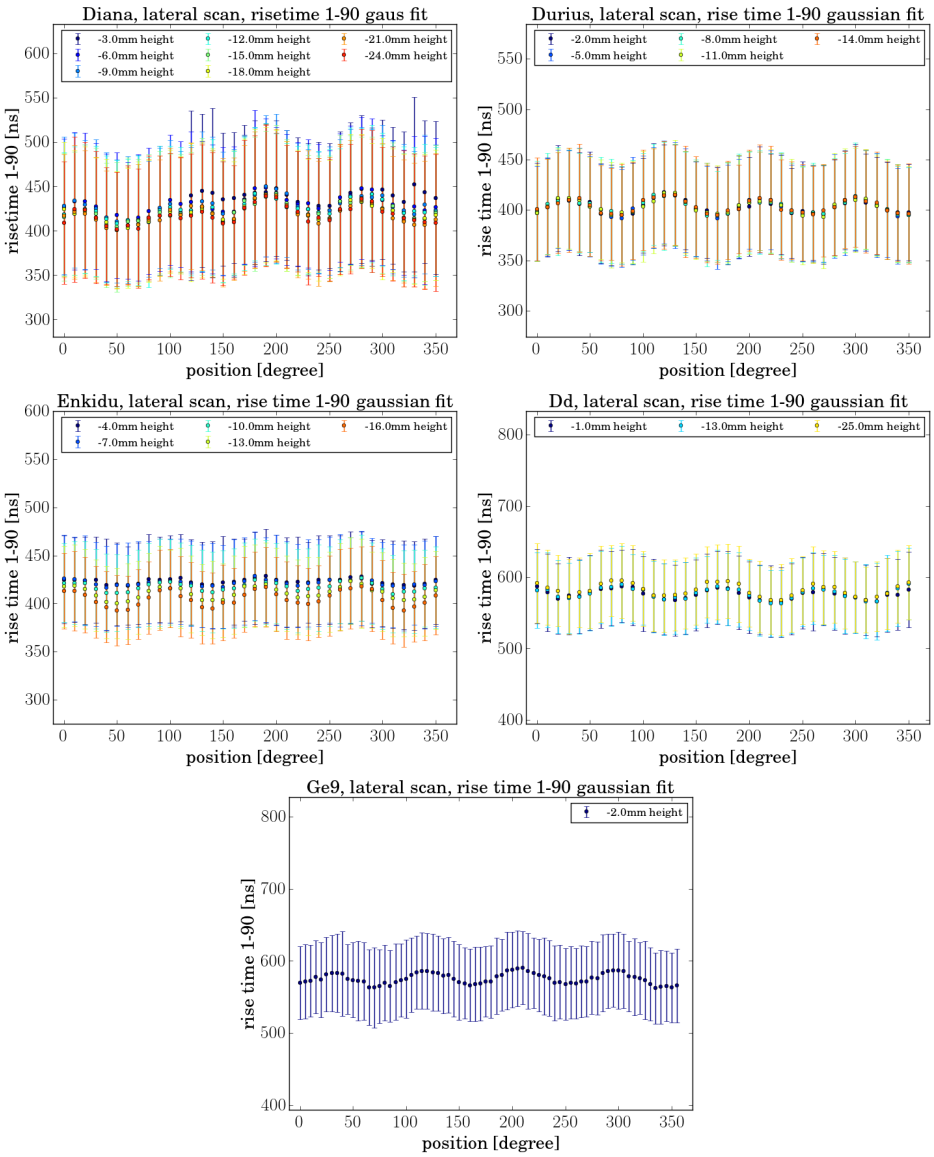

Fig. A.2 Summery 1-90% rise time for the lateral circular scans. Each point in the graphs represents the mean of the Gaussian fitted to the rise time distribution in the 59.5 keV ROI with the sigma as error bars. Each color represents a different z position in the scan with the top surface of the detector as the 0 point.

top scans A/E

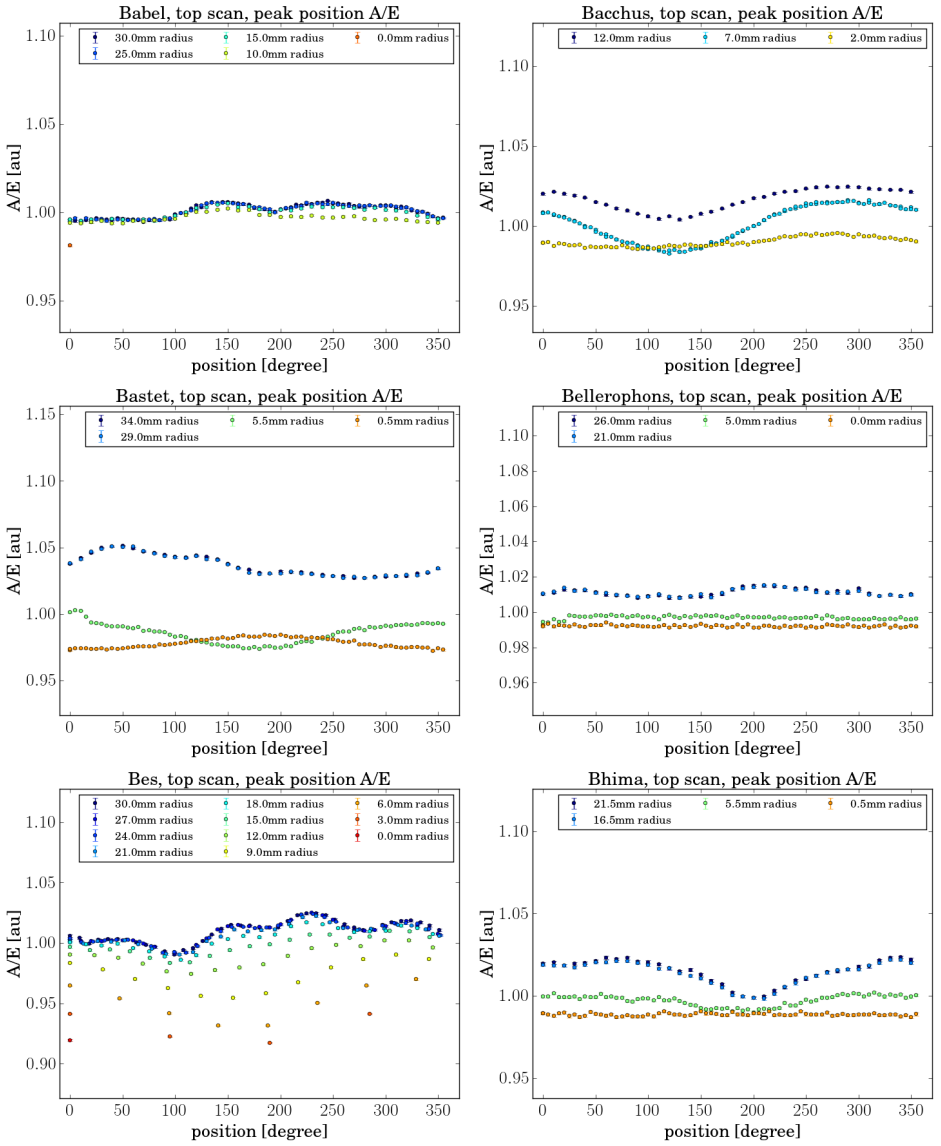
Babel, top scan, peak position A/E
30.0mm radius
25.0mm radius
15.0mm radius
10.0mm radius
0.0mm radius
A/E [au]
position [degree]
Bacchus, top scan, peak position A/E
12.0mm radius
7.0mm radius
2.0mm radius
A/E [au]
position [degree]
Bastet, top scan, peak position A/E
34.0mm radius
29.0mm radius
5.5mm radius
0.5mm radius
A/E [au]
position [degree]
Bellerophons, top scan, peak position A/E
26.0mm radius
21.0mm radius
5.0mm radius
0.0mm radius
A/E [au]
position [degree]
Bes, top scan, peak position A/E
30.0mm radius
27.0mm radius
24.0mm radius
21.0mm radius
18.0mm radius
15.0mm radius
12.0mm radius
9.0mm radius
6.0mm radius
3.0mm radius
0.0mm radius
A/E [au]
position [degree]
Bhima, top scan, peak position A/E
21.5mm radius
16.5mm radius
5.5mm radius
0.5mm radius
A/E [au]
position [degree]

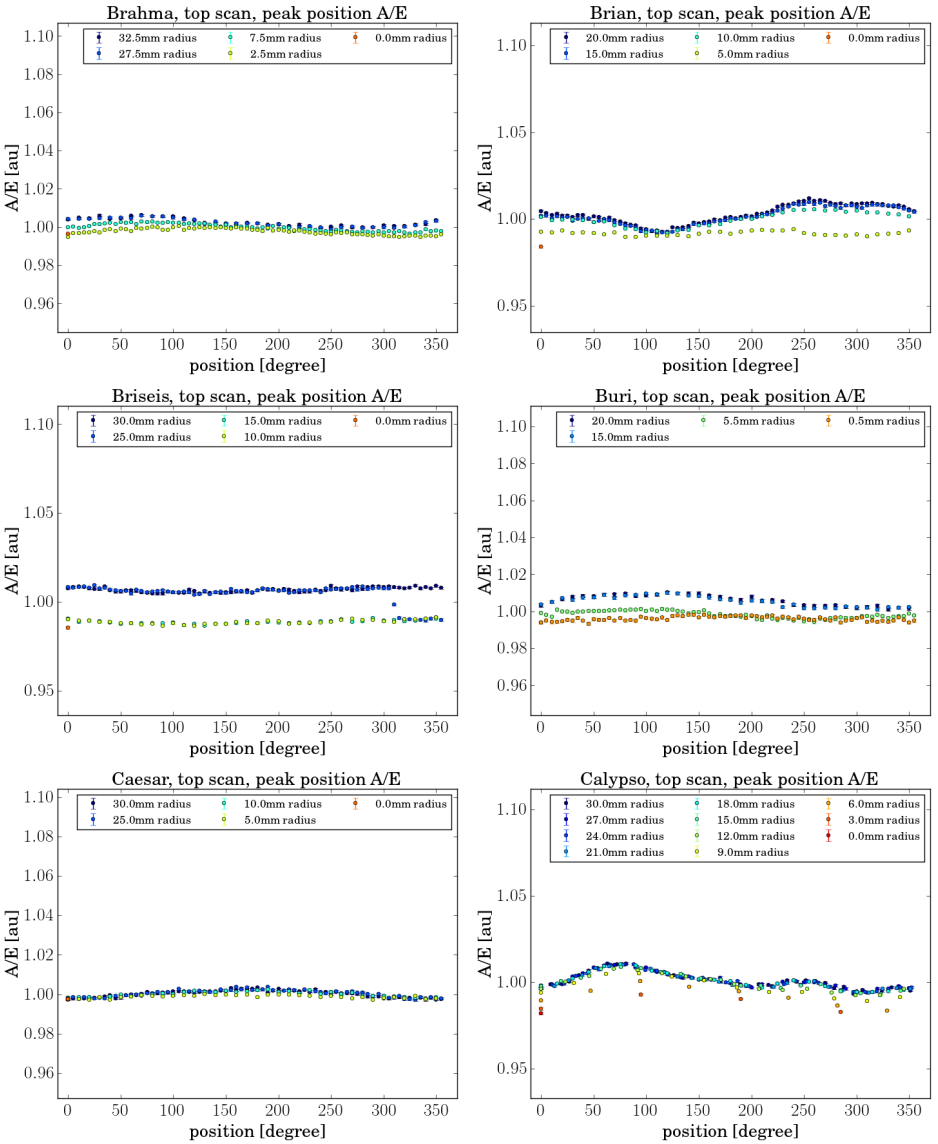
Brahma, top scan, peak position A/E
32.5mm radius
27.5mm radius
7.5mm radius
2.5mm radius
0.0mm radius
A/E [au]
position [degree]
Brian, top scan, peak position A/E
20.0mm radius
15.0mm radius
10.0mm radius
5.0mm radius
0.0mm radius
A/E [au]
position [degree]
Briseis, top scan, peak position A/E
30.0mm radius
25.0mm radius
15.0mm radius
10.0mm radius
0.0mm radius
A/E [au]
position [degree]
Buri, top scan, peak position A/E
20.0mm radius
15.0mm radius
5.5mm radius
0.5mm radius
A/E [au]
position [degree]
Caesar, top scan, peak position A/E
30.0mm radius
25.0mm radius
10.0mm radius
5.0mm radius
0.0mm radius
A/E [au]
position [degree]
Calypso, top scan, peak position A/E
30.0mm radius
27.0mm radius
24.0mm radius
21.0mm radius
18.0mm radius
15.0mm radius
12.0mm radius
9.0mm radius
6.0mm radius
3.0mm radius
0.0mm radius
A/E [au]
position [degree]

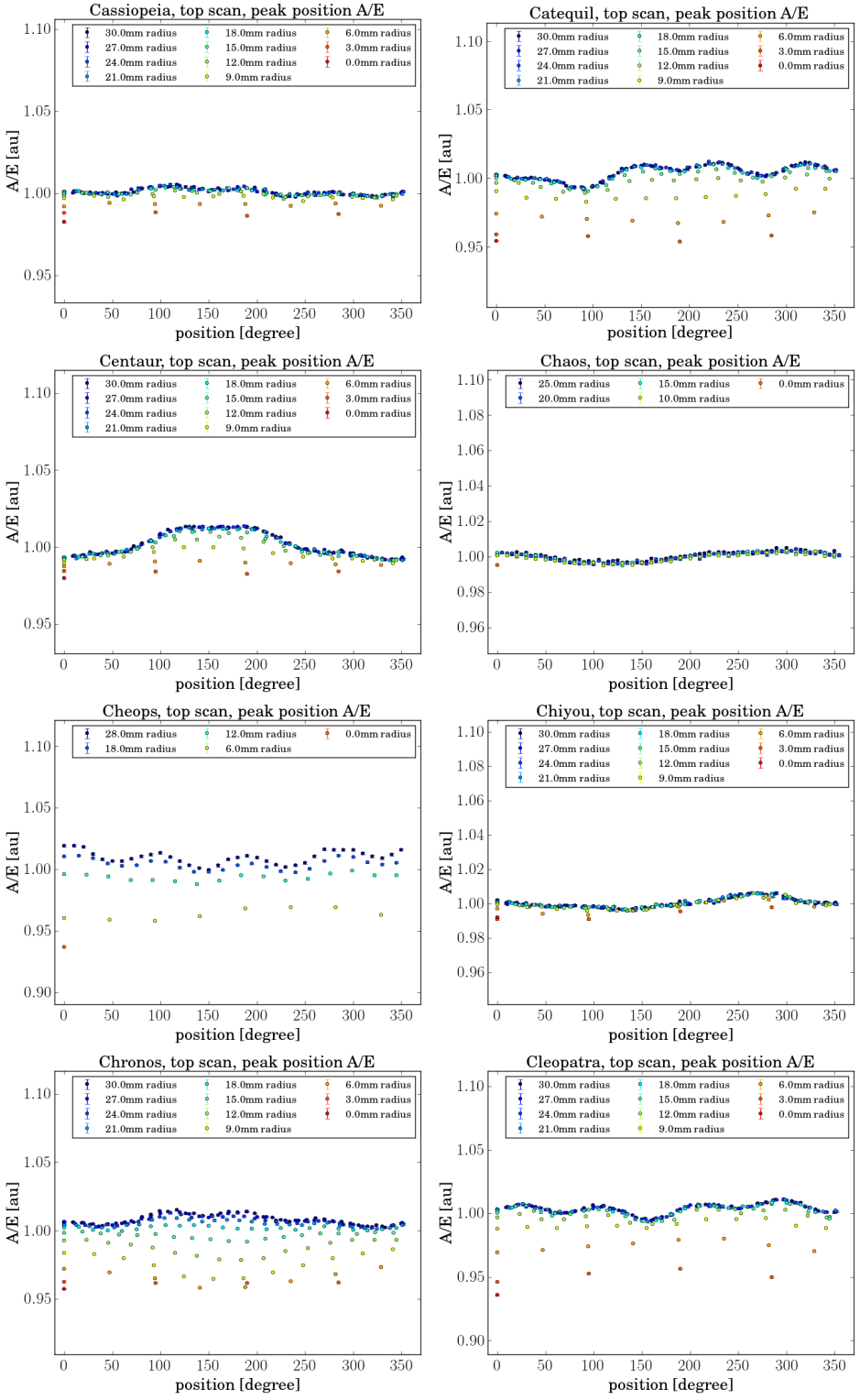
Cassiopeia, top scan, peak position A/E
Catequil, top scan, peak position A/E
Centaur, top scan, peak position A/E
Chaos, top scan, peak position A/E
Cheops, top scan, peak position A/E
Chiyou, top scan, peak position A/E
Chronos, top scan, peak position A/E
Cleopatra, top scan, peak position A/E
30.0mm radius
27.0mm radius
24.0mm radius
21.0mm radius
18.0mm radius
15.0mm radius
12.0mm radius
9.0mm radius
6.0mm radius
3.0mm radius
0.0mm radius
25.0mm radius
20.0mm radius
15.0mm radius
10.0mm radius
28.0mm radius
18.0mm radius
12.0mm radius
6.0mm radius
A/E [au]
position [degree]

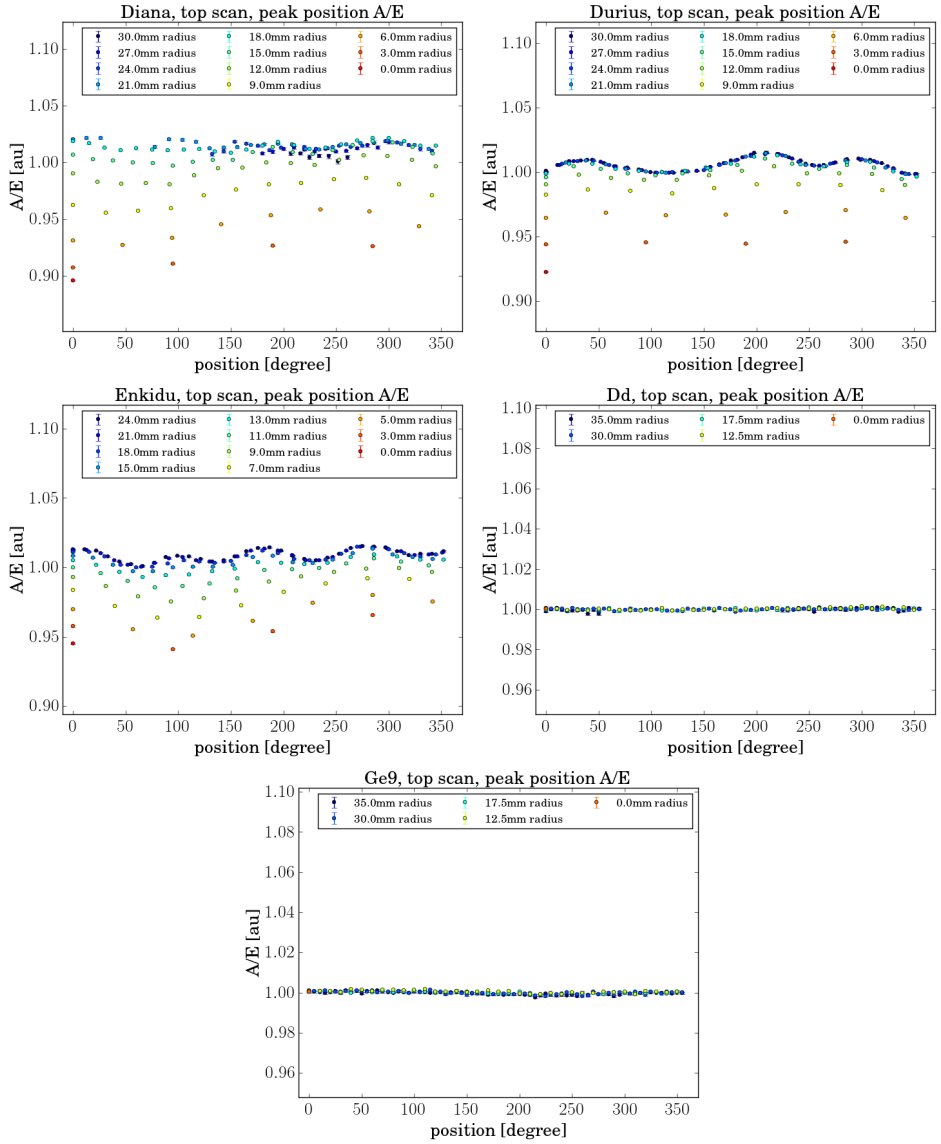

Fig. A.3 Summery A/E time for the top circular scans. Each point in the graphs represents the mean of the Gaussian fitted to the A/E distribution in the 59.5 keV ROI. Different radii are plotted in different colors. The middle point is plotted as r=0 and ϕ =0^0.

lateral scans A/E

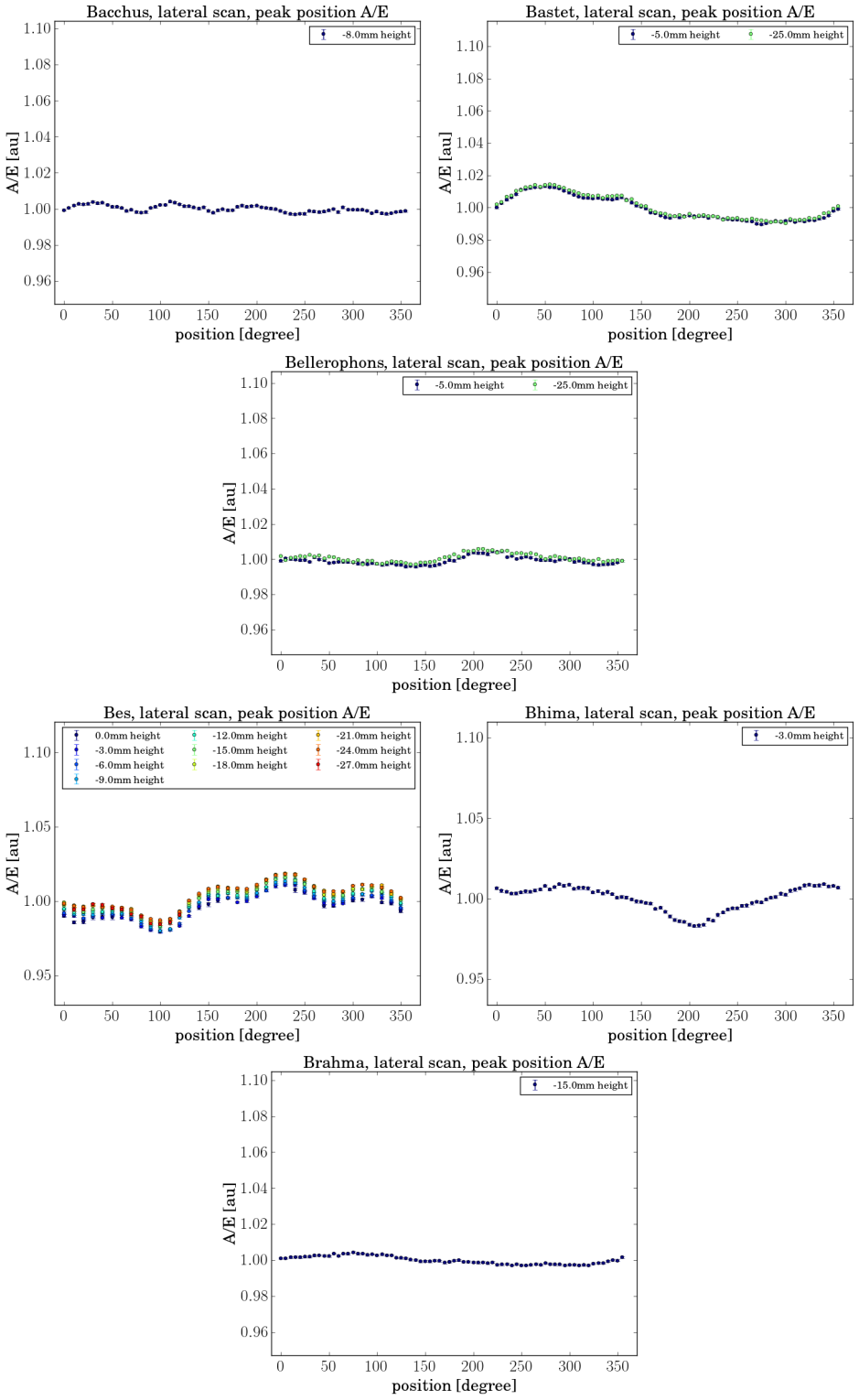

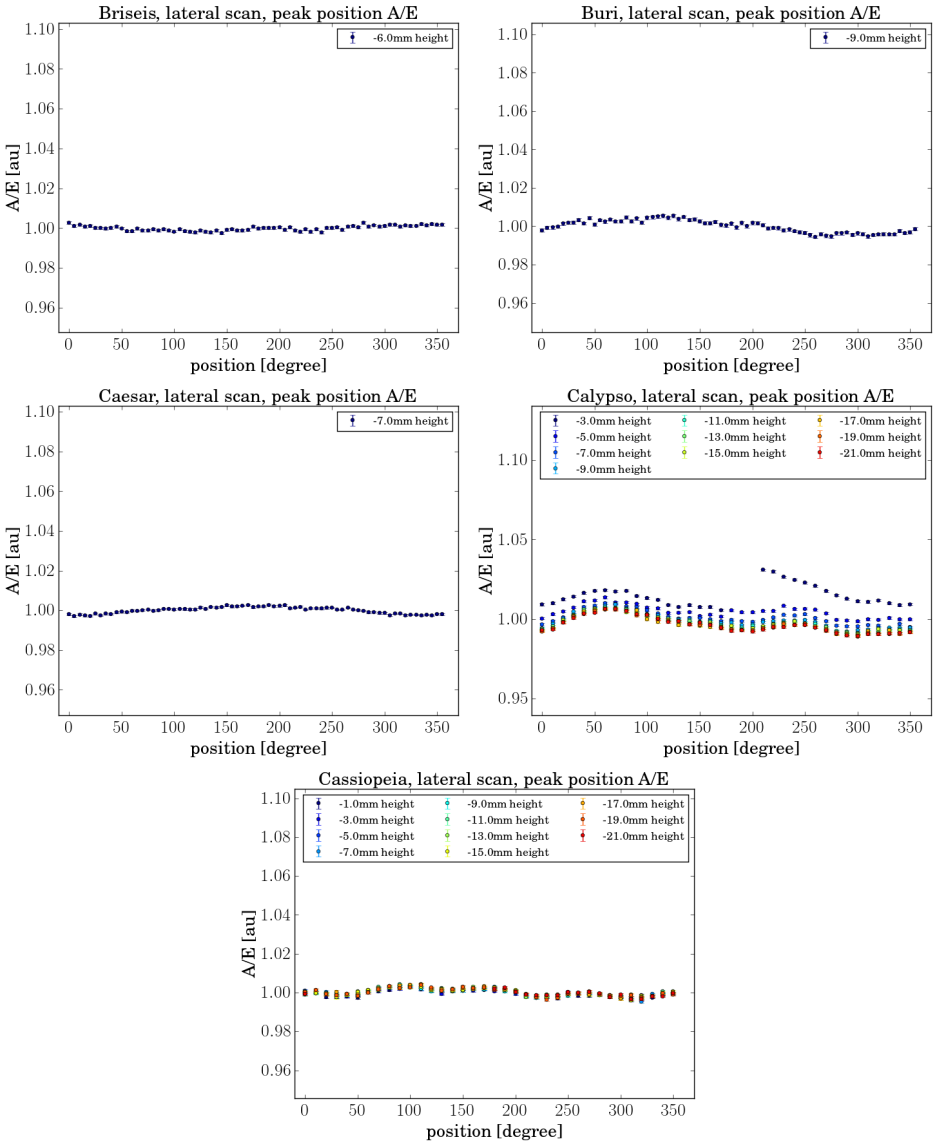
Briseis, lateral scan, peak position A/E
-6.0mm height
A/E [au]
position [degree]
Buri, lateral scan, peak position A/E
-9.0mm height
A/E [au]
position [degree]
Caesar, lateral scan, peak position A/E
-7.0mm height
A/E [au]
position [degree]
Calypso, lateral scan, peak position A/E
-3.0mm height
-5.0mm height
-7.0mm height
-9.0mm height
-11.0mm height
-13.0mm height
-15.0mm height
-17.0mm height
-19.0mm height
-21.0mm height
A/E [au]
position [degree]
Cassiopeia, lateral scan, peak position A/E
-1.0mm height
-3.0mm height
-5.0mm height
-7.0mm height
-9.0mm height
-11.0mm height
-13.0mm height
-15.0mm height
-17.0mm height
-19.0mm height
-21.0mm height
A/E [au]
position [degree]

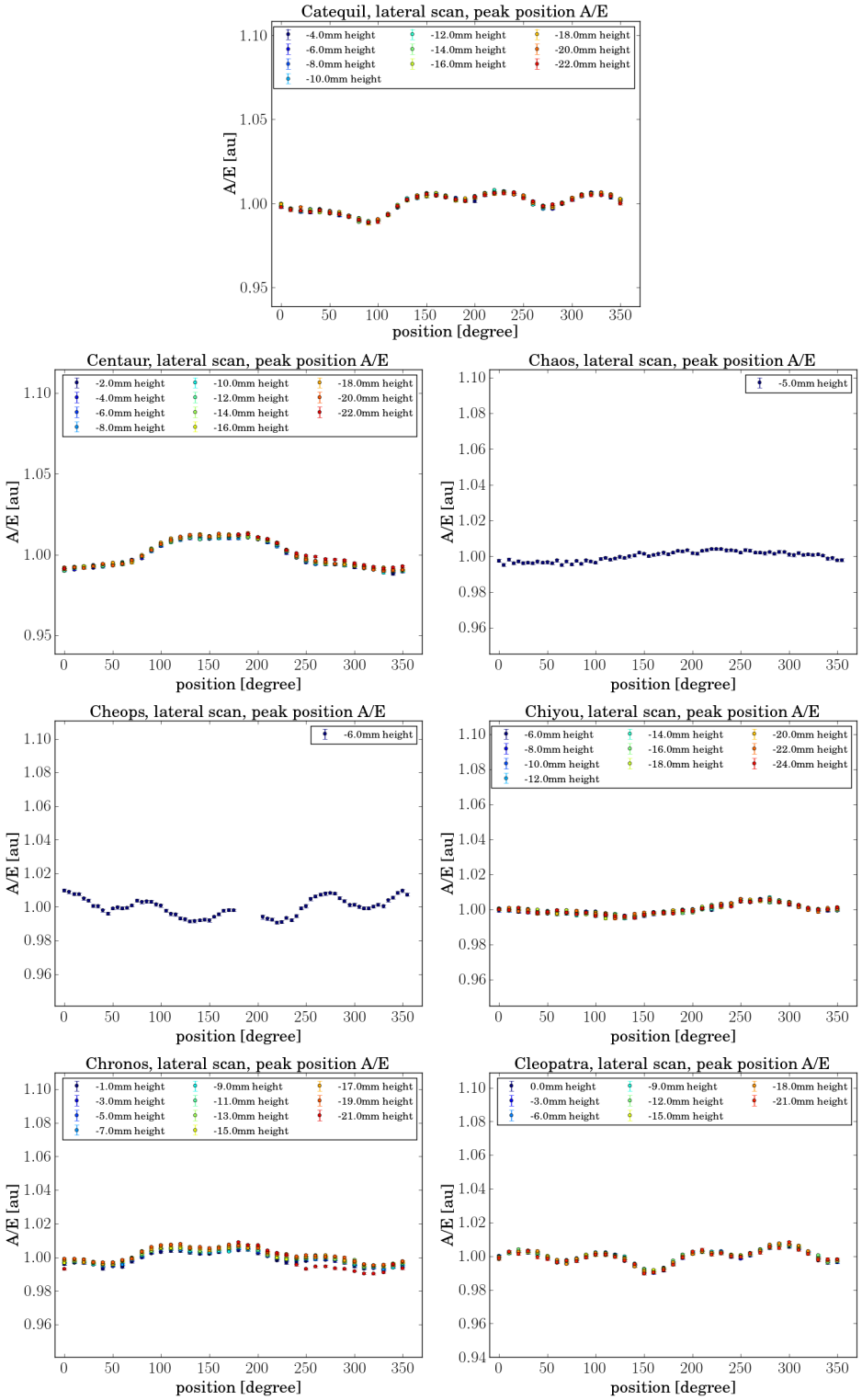
Catequil, lateral scan, peak position A/E
-4.0mm height
-6.0mm height
-8.0mm height
-10.0mm height
-12.0mm height
-14.0mm height
-16.0mm height
-18.0mm height
-20.0mm height
-22.0mm height
A/E [au]
position [degree]
Centaur, lateral scan, peak position A/E
-2.0mm height
-4.0mm height
-6.0mm height
-8.0mm height
-10.0mm height
-12.0mm height
-14.0mm height
-16.0mm height
-18.0mm height
-20.0mm height
-22.0mm height
A/E [au]
position [degree]
Chaos, lateral scan, peak position A/E
-5.0mm height
A/E [au]
position [degree]
Cheops, lateral scan, peak position A/E
-6.0mm height
A/E [au]
position [degree]
Chiyou, lateral scan, peak position A/E
-6.0mm height
-8.0mm height
-10.0mm height
-12.0mm height
-14.0mm height
-16.0mm height
-18.0mm height
-20.0mm height
-22.0mm height
-24.0mm height
A/E [au]
position [degree]
Chronos, lateral scan, peak position A/E
-1.0mm height
-3.0mm height
-5.0mm height
-7.0mm height
-9.0mm height
-11.0mm height
-13.0mm height
-15.0mm height
-17.0mm height
-19.0mm height
-21.0mm height
A/E [au]
position [degree]
Cleopatra, lateral scan, peak position A/E
0.0mm height
-3.0mm height
-6.0mm height
-9.0mm height
-12.0mm height
-15.0mm height
-18.0mm height
-21.0mm height
A/E [au]
position [degree]

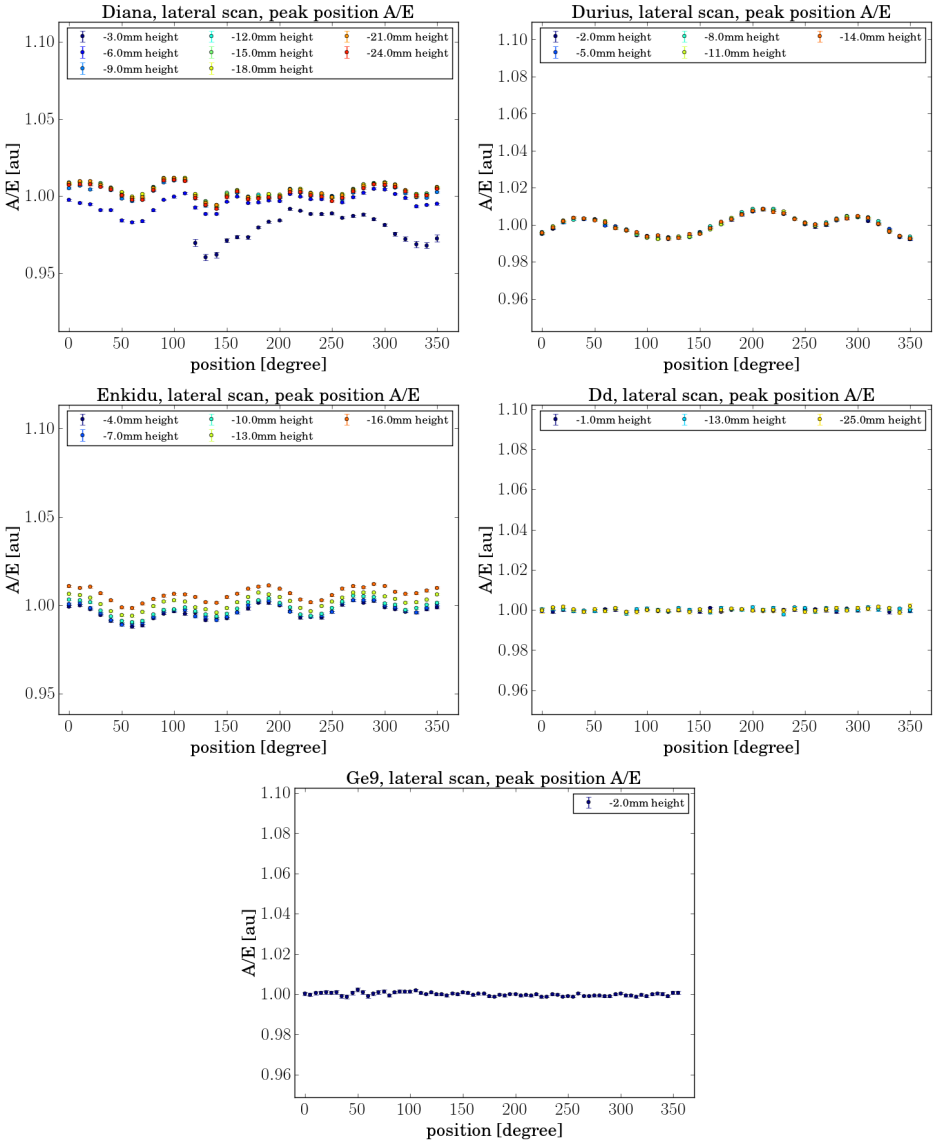

Fig. A.4 Summery A/E for the lateral circular scans. Each point in the graphs represents the mean of the Gaussian fitted to the A/E distribution in the 59.5 keV ROI. Each color represents a different z position in the scan with the top surface of the detector as the 0 point.

Acknowledgements

Ich möchte mich bei allen bedanken, die mich auf dem langen Weg der Fertigstellung dieser Arbeit begleitet haben und deren Unterstützung und Hilfe maßgebend dafür war, dass dieser nun endet.

Ein besonderer Dank gilt meinen Betreuern Prof. Dr Josef Jochum und Prof. Dr. Peter Grabmayr, die es mir zum einen ermöglicht haben diese Arbeit anzufertigen (vor allem fertigzustellen) und mich auch ermuntert haben diesen Weg zu gehen.

Ich danke Ihnen auch für die Unterstützung bei der Organisation meines Forschungsaufenthaltes am LBNL. Dieser war eine sehr prägende Erfahrung in meinem Leben. Mein Dank gilt auch dem DAAD, der diesen ermöglicht hat,sowie Alan Poon, der ein großartiger Gastgeber war.

Mein Dank geht auch an die gesamte GERDA-Kollaboration, die dieses aufregende und einzigartige Experiment vollbracht hat. Die gemeinsamen Meetings werden mir immer unvergesslich bleiben.

Ein besonderer Dank geht an Robert Radford und Dusan Budjáš, die immer eine Anlaufstelle waren, wenn ich fachlich nicht mehr weiter wusste. Sie hatten immer ein offenes Ohr für meine Probleme und konnten mir den Weg in die richtige Richtung weisen.

Ich möchte dem gesamten Hades Team für die tolle Zusammenarbeit und die Erlebnisse während der Messschichten und Trappistenbierverköstigungen in Belgien danken. Die ersten angereicherten Detektoren in den Händen zu halten und in Betrieb zu nehmen war ein besonderer Moment.

Ich danke Susanne Mertens für die wissenschaftlich wie persönlich unglaublich bereichernde Zusammenarbeit am LBL. Susanne, du hast mir gezeigt wie sehr ein Mensch sich für die Physik begeistern kann.

Ein großer Dank geht an alle PIT Mitglieder, die mich in dieser langen Zeit begleitet haben. Vielen Dank für eure Hilfe und die gemeinsamen Erlebnisse, ohne die ich diese lange Zeit nicht überstanden hätte.

An alle die Korrekturgelesen haben: Ihr seid meine persönlichen Helden!

Lee thanks for the fantastic time we had together!

Insbesondere möchte ich mich bei meinen Eltern dafür bedanken, dass Sie es mir ermöglicht haben zu studieren und mich auch bei der Promotion voll unterstütz haben. Dies war eine ganz besondere Zeit in meinem Leben und ein großes Privileg.
Deborah ich danke Dir, dass du während all dieser Zeit für mich da warst und mich unterstützt hast, egal wie egoistisch meine Entscheidungen auch mal waren. Ohne deinen Rückhalt währe diese Arbeit nie fertig geworden!
Feli und Lina ich danke euch einfach dafür, dass es euch gibt!